

**Cellular and subcellular analysis
of peripheral neuropathy
caused by peroxisomal dysfunction in mice**

Dissertation

for the award of the degree
"Doctor rerum naturalium" (Dr.rer.nat)
of the Georg-August University Göttingen

within the doctoral program Molecular Medicine
of the Georg-August University School of Science (GAUSS)

submitted by

Sandra Kleinecke

born in Blankenburg (Harz), Germany

Göttingen, 2016

Thesis committee:

Prof. Klaus-Armin Nave, Ph.D. (Reviewer)

Department of Neurogenetics

Max Planck Institute of Experimental Medicine, Göttingen

Prof. Dr. Jutta Gärtner (Reviewer)

Department of Neuropediatrics

University Medical Center, Göttingen

Prof. Dr. Mikael Simons (Reviewer)

Department of Cellular Neuroscience

Max Planck Institute of Experimental Medicine, Göttingen

Extended thesis committee:

Prof. Dr. Michael Meinecke

Department of Molecular Membrane Biology

University Medical Center, Göttingen

Nuno Raimundo, Ph.D.

Department of Cellular Biochemistry

University Medical Center, Göttingen

Prof. Dr. Dr. Hannelore Ehrenreich

Department of Clinical Neuroscience

Max Planck Institute of Experimental Medicine, Göttingen

Date of oral examination: 04.10. 2016

Declaration

I hereby declare that the Ph.D. thesis entitled, "Cellular and subcellular analysis of peripheral neuropathy caused by peroxisomal dysfunction in mice", was written independently and with no other sources and aids than quoted.

Göttingen,

Sandra Kleinecke

Curiosity is always the first step to resolving a problem.

Galileo Galilei

To my family.

Acknowledgements

First of all, I thank Dr. Celia Kassmann for giving me the opportunity to work independent on this interesting project. I thank her for the great supervision and all the inspiring discussions. Her confidence and extraordinary optimism motivated and encouraged me all the time.

I further thank Prof. Klaus-Armin Nave, PhD for giving me the opportunity to work in his department and for providing such an excellent working environment. It was a great experience to work and develop my scientific competences in such a heterogeneous team.

I thank my thesis committee, Prof. Dr. Mikael Simons and Prof. Dr. Jutta Gärtner for their ideas and advices that influenced this work. Furthermore, I thank my extended committee, Prof. Dr. Michael Meinecke, Prof. Dr. Dr. Hannelore Ehrenreich, and Nuno Raimundo, PhD for their interest in my project and taking their time to attend my defense.

Many Thanks also to...

...the whole PEX-lab group for the nice working atmosphere and all the scientific and non-scientific discussions. I especially thank Jenny Günther, the good soul of the group, for her comprehensive and patient help with technical issues.

...the EM facility, Torben Ruhwedel, Dr. Wiebke Möbius and Boguslaw Sadowski for teaching and helping me a lot with the electron microscopy.

...Dr. Judith Blanz and Meryem Senkara for their great help with lysosomal enzyme assays and providing antibodies. I'm especially grateful for welcoming and teaching me this technique.

...Dr. Britta Brügger for her collaboration and doing lipid mass spectrometry.

...Dr. Rhona McGonigal and Prof. Hugh Willison for providing antibodies and their great technical and theoretical support regarding gangliosides.

...Dr. Livia de Hoz for advices and analysis of electrophysiological data.

...Prof. Myriam Baes for her collaboration and providing mice.

...Dr. Susanne Quintes, Dr. Theresa Kungl, and Dr. Julia Patzig for their advices and help concerning PNS biology.

...Annette Fahrenholz, Ramona Jung, and Ulli Bode for technical help in many ways.

...the animal caretakers for looking after my mice and thereby providing the basis of this work.

...Michaela Schmalstieg and Gabriele Endo for organizational help.

...Lothar Demel, Hans-Joachim Horn, Rolf Merker, and Harry Scherer for technical help concerning IT issues.

...the whole Neurogenetics department for the great working atmosphere. I especially want to thank Sina, Jenny, Sarah, Dinah, Tim, and Jan for the great time in the lab and all the fun we had during the retreats.

Abschließend geht ein großer Dank an meine Familie, die mich immer unterstützt hat und ohne die dies alles nicht möglich gewesen wäre. Ein besonderer Dank geht an Andreas Schmidt, der mir immer zu Seite stand und auch in schwierigen Phasen immer die richtigen Worte gefunden hat um mich zu motivieren.

Content

List of figures	11
Abbreviations	12
Abstract	15
1. Introduction	16
1.1 The peripheral nervous system	16
1.1.1 Myelin formation and composition	16
1.1.2 Non-compact myelin and metabolic support of axons	18
1.1.3 Molecular domains of myelinated axons.....	20
1.1.4 Ganglioside metabolism and function.....	22
1.2 Lysosomes in the nervous system	23
1.2.1 The endosomal-autophagic-lysosomal system.....	23
1.2.2 Lysosomal storage disorders.....	25
1.3 Peroxisomes in the nervous systems.....	26
1.3.1 Peroxisome biogenesis	26
1.3.2 Peroxisomal lipid metabolism	28
1.3.3 Peroxisomal disorders and their impact on the nervous system.....	28
1.4 Aim of this study.....	31
2. Results	32
2.1 Ablation of PEX5 from Schwann cells	32
2.1.1 Disturbed import of peroxisomal proteins	32
2.1.2 Disturbed peroxisomal lipid metabolism	33
2.2 Impact of peroxisomal dysfunction on nerve function.....	36
2.2.1 Electrophysiological analysis indicates early sciatic nerve dysfunction	36
2.2.2 Tendency of more neuromuscular junctions in aged <i>Cnp-Cre::Pex5^{flox/flox}</i>	38
2.2.3 Analysis of sensory impairment.....	39
2.3 Impact of peroxisomal dysfunction on nerve integrity.....	40
2.3.1 No considerable demyelination or deficient myelin compaction	40
2.3.2 Axon degeneration is not a substantial feature of sciatic nerve pathology	42
2.3.3 Mild macrophage activation with occasional T-cells infiltration.....	44
2.4 Molecular composition of nodes of Ranvier	46
2.4.1 Normal formation of nodes and paranodal junctions	46
2.4.2 Ectopic localization of juxtapanodal K _v 1.1 channels along internodes.....	48
2.4.3 Impaired anchoring of K _v 1.1 channels	50
2.5 Perturbation of gangliosides.....	51

2.6 Secondary alterations of the endosomal-lysosomal system.....	54
2.6.1 Lysosomes are in close contact with peroxisomes	54
2.6.2 Accumulation of lysosomes at paranodes	55
2.6.3 Accumulation of lysosomes within enlarged Schmidt-Lanterman incisures	58
2.6.4 Alterations of lysosomal function	61
2.7 Comparative analysis of ABCD1-deficient mice, a model of human adrenomyeloneuropathy	62
2.7.1 Behavioral analysis of nerve impairment in ABCD1-deficient mice	62
2.7.2 Absence of myelin alterations and axonal loss in aged <i>Abcd1</i> ^{-/-} mice	65
2.7.3 Kv1.1 channel clustering is impaired in aged <i>Abcd1</i> ^{-/-} mice	68
2.7.4 Lysosomal alterations and abnormal Schmidt-Lanterman incisures.....	70
3. Discussion	73
3.1 PEX5-deficiency disrupts peroxisomal function in SC.....	73
3.2 Impaired nerve function despite normal myelin and axon distribution	74
3.3 Ectopic juxtaparanodal proteins and potential effects on nerve excitability	76
3.4 Peroxisomal dysfunction disturbs ganglioside homeostasis.....	79
3.5 Pex5-deficiency in SC mimics symptoms of lysosomal storage disorders	80
3.6 Increased number of SLI- a consequence of lysosomal storage?.....	82
3.7 ABCD1-deficiency results in similar, but less severe neuropathy.....	83
3.8 Model of Cnp-Pex5-deficiency	85
4. Material	86
4.1. Equipment.....	86
4.2 Molecular biology	88
4.3 Protein biochemistry.....	89
4.4 Lysosomal enzyme assay	90
4.5 Immunohistochemistry	91
4.6 Immuno-electron microscopy	94
4.7 Electron microscopy	94
4.8 Antibodies	95
4.9 Dyes and marker.....	96
4.10 Primer	96
4.11 Mouse lines.....	97
5. Methods.....	98
5.1 Animals	98
5.1.1 Tail digest and genotyping PCR	98
5.2 Molecular biology	100
5.2.1 RNA isolation from sciatic nerves	100

5.2.2 Complementary single stranded DNA (cDNA) synthesis.....	101
5.2.3 Quantitative real-time PCR (qRT-PCR)	101
5.2.4 Enzyme activity assay	102
5.2.5 Mass spectrometry	102
5.3 Protein biochemistry.....	103
5.3.1 Sample preparation	103
5.3.2 Lowry protein assay.....	103
5.3.3 Protein separation using SDS-PAGE	103
5.3.4 Western blotting.....	104
5.4 Fluorescence microscopy	105
5.4.1 Teased fiber preparation	105
5.4.2 Immunofluorescence of teased fibers.....	105
5.4.3 <i>Ex vivo</i> fluorescent staining of gangliosides	105
5.4.4 Immunofluorescence of cryo sections	106
5.5 Histology	107
5.5.1 Perfusion and paraffin embedding.....	107
5.5.2 DAB staining of paraffin sections.....	107
5.6 Immuno-electron microscopy	108
5.6.1 Perfusion and tissue preparation.....	108
5.6.2 Preparation of ultrathin cryo sections	109
5.6.3 Immunolabeling of ultrathin cryo sections.....	109
5.7 Electron microscopy.....	109
5.7.1 Perfusion and epon embedding.....	109
5.7.2 Preparation of semi- and ultra-thin sections	110
5.7.3 Staining of semi-thin sections and quantification of axon number	110
5.7.4 Contrasting of ultra-thin sections	111
5.7.5 Electron microscopy and g-ratio analysis	111
5.8 Electrophysiology	111
5.9 Behavior	112
5.9.1 Grid test.....	112
5.9.2 Grip strength.....	112
5.9.3 Elevated beam.....	112
5.9.4 Dynamic plantar aesthesiometer	113
5.9.5 Plantar Hargreaves Test.....	113
References	114
Curriculum vitae	132

List of figures

<i>Fig. 1: Schwann cell differentiation during development.....</i>	<i>17</i>
<i>Fig. 2: Scheme of a peripheral myelinated axon highlighting regions of non-compact myelin.....</i>	<i>19</i>
<i>Fig. 3: Molecular organization of myelinated peripheral nerve fibers</i>	<i>21</i>
<i>Fig. 4: Synthesis of brain gangliosides and their function in axo-glial interaction at nodes</i>	<i>23</i>
<i>Fig. 5: The endosomal-autophagic-lysosomal system.....</i>	<i>25</i>
<i>Fig. 6: Peroxisomal protein import</i>	<i>27</i>
<i>Fig. 7: PEX5 ablation from Schwann cells disrupts import of peroxisomal proteins.....</i>	<i>33</i>
<i>Fig. 8: PEX5 ablation from Schwann cells disturbs peroxisomal lipid metabolism</i>	<i>35</i>
<i>Fig. 9: Functional impairment in 2 months old Cnp-Cre::Pex5^{flox/flox} sciatic nerves.....</i>	<i>37</i>
<i>Fig. 10: Number of NMJs is slightly enhanced in gastrocnemius muscles of Cnp-Cre::Pex5^{flox/flox}</i>	<i>38</i>
<i>Fig. 11: Impaired pressure, but not heat sensation in 9 months old Cnp-Cre::Pex5^{flox/flox}</i>	<i>39</i>
<i>Fig. 12: Normal myelin thickness in Cnp-Cre::Pex5^{flox/flox} sciatic nerves.....</i>	<i>41</i>
<i>Fig. 13: Normal myelin compaction and protein composition in Cnp-Cre::Pex5^{flox/flox} sciatic nerves</i>	<i>42</i>
<i>Fig. 14: Normal distribution and number of myelinated axons in Cnp-Cre::Pex5^{flox/flox} sciatic nerves.....</i>	<i>43</i>
<i>Fig. 15: Moderate neuroinflammation in Cnp-Cre::Pex5^{flox/flox} sciatic nerves.....</i>	<i>45</i>
<i>Fig. 16: Paranodal junctions are intact</i>	<i>47</i>
<i>Fig. 17: Juxtaparanodal Kv1.1 proteins are progressively shifted towards internodes.....</i>	<i>49</i>
<i>Fig. 18: The entire juxtaparanodal complex drifts into internodes</i>	<i>50</i>
<i>Fig. 19: Ganglioside metabolism and their distribution at nodes of Ranvier is disturbed</i>	<i>53</i>
<i>Fig. 20: Peroxisomes and lysosomes are closely associated in the paranodal Schwann cell compartment.....</i>	<i>54</i>
<i>Fig. 21: Accumulation of enlarged lysosome-associated vesicles at paranodes</i>	<i>56</i>
<i>Fig. 22: Endosomal and autophagic vesicles are not accumulating at nodes of Cnp-Cre::Pex5^{flox/flox} nerves.....</i>	<i>57</i>
<i>Fig. 23: Schmidt-Lanterman incisures are increased in number and contain LAMP1-positive vesicles.....</i>	<i>59</i>
<i>Fig. 24: Relative protein abundance and mRNA expression of LAMP1 and LIMP2</i>	<i>60</i>
<i>Fig. 25: Lysosomal enzyme activity is progressively enhanced in Cnp-Cre::Pex5^{flox/flox} nerves</i>	<i>61</i>
<i>Fig. 26: Behavioral assessment of motor performance.....</i>	<i>64</i>
<i>Fig. 27: Normal pressure and heat sensation in aged Abcd1^{-/-} mice.....</i>	<i>65</i>
<i>Fig. 28: Normal myelin thickness and age-related myelin inclusions.....</i>	<i>66</i>
<i>Fig. 29: No axonal loss in Abcd1^{-/-} sciatic nerves</i>	<i>67</i>
<i>Fig. 30: Ectopic localization of juxtaparanodal Kv1.1 proteins despite intact paranodal junctions</i>	<i>69</i>
<i>Fig. 31: Accumulation of lysosome-associated vesicles in regions of non-compact myelin</i>	<i>71</i>
<i>Fig. 32: Lysosomal enzyme activity in Abcd1^{-/-} nerves</i>	<i>72</i>
<i>Fig. 33: Hypothetical model of Cnp-Pex5-mediated pathomechanism in myelinated fibers</i>	<i>85</i>

Abbreviations

ABCD1	ATP-binding cassette, sub-family D (ALD), member 1 protein
<i>Abcd1</i>	ATP-binding cassette, sub-family D (ALD), member 1 gene
ACSF	Artificial cerebrospinal fluid
AMN	Adrenomyeloneuropathy
AnkG	Ankyrin G
APS	Ammonium persulfate
ATG5	Autophagy-related protein 5
ATG8	Autophagy-related protein 8
ATP	Adenosine triphosphate
bp	Base pairs
BSA	Bovine serum albumin
°C	Degrees Celsius (centigrades)
CAP	Compound action potential
cALD	Cerebral ALD
CAM	Cell adhesion molecules
CASPR	Contactin-associated protein
CASPR2	Contactin-associated protein 2
CMAP	Compound muscle action potential
CNP	2'3'-cyclic nucleotide 3'phosphodiesterase
CNS	Central nervous system
cKO	Conditional knockout
CoA	Coenzyme A
CO ₂	Carbon dioxide
CST	Cerebroside sulfotransferase
CTB	Cholera toxin subunit B
CTR	Control
DAB	3,3'-Diaminobenzidine
DAPI	4'-6-Diamidino-2-phenylindole
ddH ₂ O	Double distilled water
DNA	Deoxyribonucleic acid
dNTPs	Desoxyribonukleosidtriphosphate
EE	Early endosome
EEA1	Early-endosome associated protein 1
EDTA	Ethylene acid
e.g.	Exempli gratia
EM	Electron microscopy
ER	Endoplasmic reticulum
EtOH	Ethanol
FA	Fatty acid

Fig.	Figure
g	Gram
<i>g</i>	Standard gravity
h	Hour
HCl	Hydrogen chloride
HRP	Horseradish peroxidase
HS	Horse serum
IN	Internode
IEM	Immuno-electron microscopy
IHC	Immunohistochemistry
JXP	Juxtaparanode
K ⁺	Potassium ion
KCl	Potassium chloride
kDa	Kilodalton
K _v 1.1	Potassium voltage-gated Channel Subfamily A Member 1
LE	Late endosomes
LAMP1	Lysosomal-associated membrane protein 1
LIMP2	Lysosomal integral membrane protein 2
LSD	Lysosomal storage disorder
M	Molar
mA	Milliampere
MAG	Myelin-associated glycoprotein
MBP	Myelin basic protein
min	Minutes
mo	Months
μA	Microampere
μl	Microliter
μM	Micromolar
μm	Micrometer
mm	Millimeter
mM	Millimolar
MPI	Max Planck Institute
mRNA	Messenger ribonucleic acid
mTOR	Mechanistic target of rapamycin
n	Number
Na ⁺	Sodium ion
Na _v 1.6	Voltage-gated sodium channel 1.6
NCV	Nerve conduction velocity
NF155	Neurofascin 155
NF186	Neurofascin 186
Nm	Nanometer

NMJ	Neuromuscular junction
n.s.	Not significant
o/n	Overnight
p	P-value
P	Postnatal day
PBS	Phosphate buffered saline
PCR	Polymerase chain reaction
PFA	Paraformaldehyde
PLP	Proteolipid protein
PMP22	Peripheral myelin protein 22
PMP70	Peroxisomal membrane protein 70
PN	Paranode
PNL	Paranodal loop
PNS	Peripheral nervous system
PTS1	Peroxisomal targeting sequence 1
RAB7	Ras-related protein7
RNA	Ribonucleic acid
ROS	Reactive oxygen species
rpm	Rounds per minute
RT	Room temperature
SC	Schwann cell
sec	Second
s.e.m	Standard error of the mean
SDS	Sodium dodecyl sulfate
SLI	Schmidt-Lanterman incisures
TAG-1	Transient axonal glycoprotein-1
TGN	Trans-Golgi network
TUJ1	Neuron-specific class III beta-tubulin
U	Units
V	Volt
VLCFA	Very long-chain fatty acids
X-ALD	X-linked adrenoleukodystrophy

Abstract

Fast signal propagation and long-term integrity of myelinated axons rely on precise axo-glial interactions. A role for myelin-associated peroxisomes in facilitating axonal support by glial cells was demonstrated in a mouse model with peroxisome dysfunction specifically in myelinating glia (*Cnp-Cre::Pex5^{flox/flox}*). This Cnp-Pex5 mouse model was used in the current thesis to analyze the role of peroxisomes in myelin maintenance and Schwann cell (SC)-axon interaction. Here, a critical function of SC lipid metabolism in axonal conduction was proven by *ex vivo* electrophysiology, showing reduced conduction velocity and decreased amplitudes before behavioral deficits occurred. Unexpectedly, analysis of myelin sheath thickness, compaction, and protein composition excluded dysmyelination as the underlying reason of nerve impairment. Furthermore, the overall number and distribution of myelinated axons was normal. Vesicular accumulations within mutant paranodes could have perturbed paranodal junctions, potentially causing nerve dysfunction. However, axo-glial contact sides at this region were intact. Immunofluorescent staining revealed early-onset redistribution of juxtaparanodal Kv1.1 channels. Nevertheless, the majority of Kv1-clusters was normal in the postnatal phase, and their progressive mislocalization suggested a problem in the maintenance rather than formation. In addition, the Kv1-anchoring protein TAG-1 showed a similar pattern and colocalized with ectopic Kv1.1 ion channels. Within membranes, TAG-1 is associated with gangliosides, a class of glycosphingolipids that were massively perturbed in PEX5 mutant nerves as revealed by lipid mass spectrometry and by (immune-) fluorescent staining. Thus, gangliosides were abundantly present in enlarged vesicles, several of which were identified as lysosomes. Finally, lysosomal marker proteins and enzymatic activities were dramatically increased in mutant nerves, which are typical characteristics of lysosomal storage disorders. Most interestingly, similar pathological features were observed in aged *Abcd1*^{-/-} mice, a disease model of human adrenomyeloneuropathy, suggesting a common pathomechanism in disorders of peroxisomal β -oxidation. In summary, this work revealed secondary defects of lysosomes as a consequence of peroxisomal dysfunction *in vivo* and the importance of SC lipid metabolism for normal nerve function, independent of myelin. Since abnormal lipid metabolism is related to several other peripheral neuropathies, this knowledge may provide new therapeutic strategies for other diseases.

1. Introduction

1.1 The peripheral nervous system

The peripheral nervous system (PNS), comprising the somatosensory and autonomous nervous system, represents the interface between the central nervous system (CNS) and the inner and outer environment. Accordingly, it transmits nerve impulses from sensory receptors to the CNS (afferent nerve fibers) and signals back to muscles and glands (efferent nerve fibers). Interconnections between different compartments are made by electrical and chemical synapses. One of the best-studied chemical synapse is the neuromuscular junction that connects motor neurons with muscle fibers (Hirsch, 2007). The sciatic nerve is the largest peripheral nerve. Due to its easy accessibility and simplicity, it is an appropriate model to study interactions between axons and their myelinating Schwann cells and is well suited to investigate neurodegeneration in disease situations.

1.1.1 Myelin formation and composition

Myelination of axons facilitated the evolution of complex nervous systems by reducing energy consumption and accelerating signal propagation (Waxman, 1980; Tasaki 1939). Axons in the peripheral nervous system are myelinated by Schwann cells (SCs). SC precursors originate from neural crest cells and develop into immature SC, which approach axons (Jessen and Mirsky, 1992). Axonal signals further trigger SC proliferation and differentiation (Salzer and Bunge, 1980; Pereira et al., 2012). In contrast to oligodendrocytes in the CNS, Schwann cells myelinate only one single axonal segment. This one-to-one relation is established through radial sorting during late embryonic development and shortly after birth (Fig. 1; Jessen and Mirsky, 1999). Thereby, small caliber axons ($\leq 1 \mu\text{m}$) remain engulfed, but not myelinated, forming Remak bundles (Jessen and Mirsky, 2005; Pereira et al., 2012). These are unique to peripheral nerves and harbor unmyelinated C-fibers, which have a slow conduction velocity (0.5-2.0 m/s) and convey sensory stimuli (e.g. pain and heat; Griffin and Thompson, 2008). In contrast, large caliber axons ($> \sim 1 \mu\text{m}$) are associated with promyelinating SC.

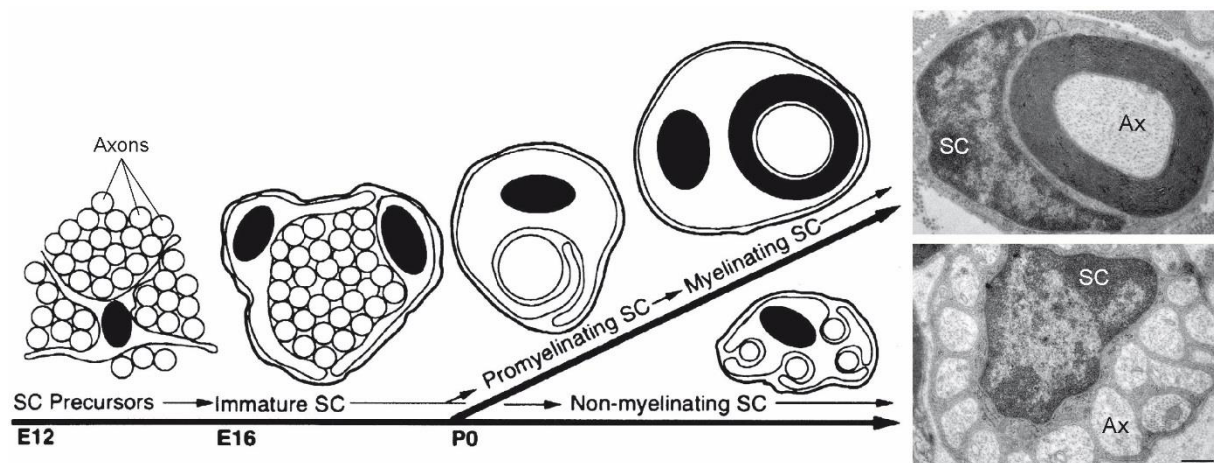


Fig. 1: Schwann cell differentiation during development

This scheme illustrates the Schwann cell (SC) lineage (left). SC progenitors develop into immature SC around embryonic day 15 (E15) and E17 in mice. These further differentiate into pro-myelinating or non-myelinating SC around birth (postnatal day 0, P0). Pro-myelinating SC further mature postnatally into myelinating SC. EM pictures (right) demonstrate a myelinating SC in close contact to an axon (Ax, top) or a non-myelinating SC engulfing several axons (bottom; scale bar, 500 nm; modified from (Scherer, 1997)

Myelination occurs postnatally and is finished at around postnatal day 30 (P30; (Garbay et al., 2000). It is controlled by complex axo-glial interactions (Pereira et al., 2012). Thus, myelin sheath thickness and internodal lengths are proportional to the axonal diameter, ensuring optimal nerve conduction (Waxman, 1980). Later studies showed that the neuronal growth factor neuregulin 1 (NRG1) type III binds to the glial receptor ErbB thereby regulating SC differentiation and myelin thickness in the PNS (Garratt et al., 2000; Michailov et al., 2004; Brinkmann et al., 2008). Myelin sheath thickness can be calculated by the ratio of the axonal diameter divided by the complete fiber diameter, which is termed the “g-ratio”.

Myelin sheaths are specialized plasma membranes of Schwann cells. They are highly abundant in lipids (70-80% of dry mass), mainly composed of cholesterol (20-30%), galactosphingolipids (e.g. cerebroside; sulfatides and gangliosides), phospholipids (e.g. plasmalogens), and saturated very long-chain fatty acids (Garbay et al., 2000). Furthermore, myelin sheaths can be differentiated into compact and non-compact compartments with characteristic and non-overlapping protein profiles. Compact myelin comprises the major part and is highly abundant in glycoproteins (e.g. *protein zero*, P0 and *peripheral myelin protein 22*, PMP22, Quarles, 2002). P0 is the major

myelin protein (50-70%) in the PNS and is essential for myelin compaction (Greenfield et al., 1973; Wiggins et al., 1975; Giese et al., 1992). Beside glycoproteins, basic proteins (e.g. *myelin basic protein*, MBP and *protein 2*, P2) are the second most abundant class of peripheral myelin proteins (Garbay et al., 2000). Other proteins, such as *2', 3'-cyclic nucleotide 3'-phosphodiesterase* (CNP) and *proteolipid proteins* (PLP/DM20), both abundant in CNS, only represent 0.5% of total PNS myelin (Uyemura et al., 1972; Pham-Dinh et al., 1991; Patzig et al., 2011).

1.1.2 Non-compact myelin and metabolic support of axons

Axonal access to extracellular metabolites is limited by insulating myelin sheaths. Additionally, peripheral nerves become quite long (e.g. sciatic nerve) and axons are thereby isolated from their neuronal cell bodies. Thus, they particularly rely on metabolic support by Schwann cells. There is strong evidence that glial cells ensure axonal long-term survival and integrity independent of myelin (Wilkins et al., 2003; Nave, 2010b; Ghosh et al., 2011; Fünfschilling et al., 2012; Viader et al., 2013). This is further emphasized by several myelin deficiencies resulting in axonal degeneration (Ferguson et al., 1997; Garbern et al., 2002; Lappe-Siefke et al., 2003; Nave et al., 2007; Griffiths, 2011). Metabolic exchange between axons and Schwann cells is facilitated by cytoplasmic channels at regions of non-compact myelin, such as paranodal loops, Schmidt-Lanterman incisures (SLI), and the outer and inner mesaxon (Arroyo and Scherer, 2000). These regions form a transport network that provides short pathways through the myelin sheath (Fig. 2). Moreover, autotypic adherens, tight, and gap junctions connect adjacent Schwann cell membranes and thereby enable rapid intracellular signaling and transport (Spiegel and Peles, 2002).

Paranodal loops connect the adaxonal myelin to the axolemma at each end of a myelin segment (Arroyo and Scherer, 2000). Heterotypic septate-like junctions between axons and paranodal loops enable fast exchange between axonal and SC cytoplasm (Fannon et al., 1995; Einheber et al., 1997). Another route for short diffusion through the myelin sheath are Schmidt-Lanterman incisures, funnel-shaped interruptions in the compact myelin of primarily peripheral fibers (Hall and Williams, 1970; Ghabriel and Allt, 1981). They are highly dynamic, thus supposed to protect peripheral nerves from mechanical stress by providing flexibility (Singer and Bryant, 1969). Also, the number

of incisures depends on the fiber diameter (Ghabriel and Allt, 1981). SLI are highly enriched in *myelin-associated glycoprotein* (MAG) that is essential for CNS myelination and glial integrity, and ensures the viability of myelinated axons in the PNS (Trapp et al., 1989; Trapp, 1990; Pan et al., 2005). Interestingly, SLI are increased in several myelin abnormalities and axonal changes, suggesting a compensatory mechanism to ensure axo-glial communication (Gould et al., 1995; Hoshi et al., 2007).

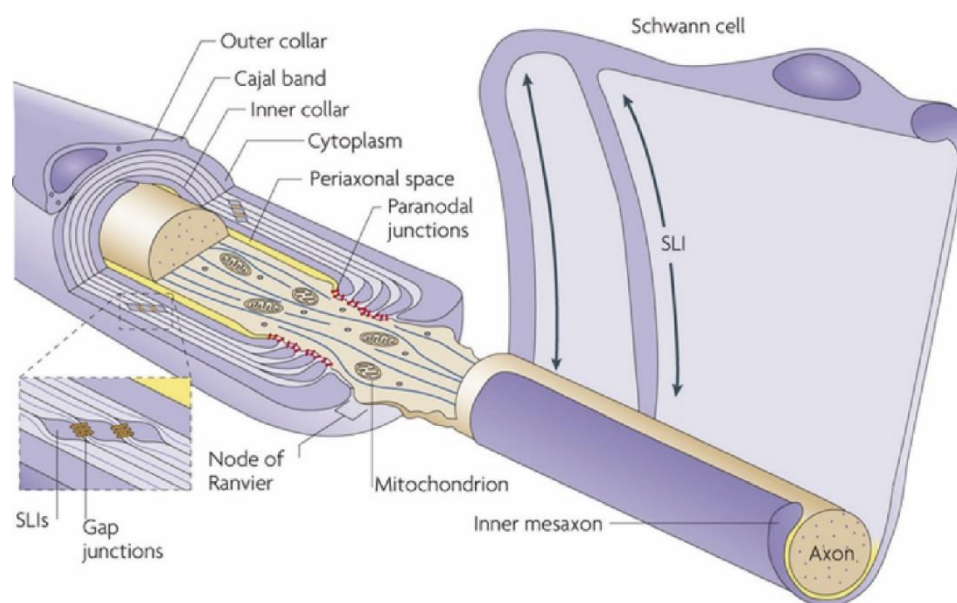


Fig. 2: Scheme of a peripheral myelinated axon highlighting regions of non-compact myelin

Regions of non-compact myelin (dark purple) provide a short transport route through compact myelin (light purple) and towards the periaxonal space (yellow). Axo-glial interactions are especially pronounced at paranodal junctions (red stripes) and Schmidt-Lanterman incisures (SLI). Unrolled Schwann cell sheaths indicate SLI that spiral around axons and are interconnected by gap junctions (inset, adapted from Nave 2010).

Besides metabolic support of axons, SC are capable of taking up axonal material at paranodes via an axon-Schwann cell network (ASN, (Gatzinsky et al., 1997). Like SLI these ASNs are highly associated with lysosomes and are therefore supposed to serve as disposal sites for non-degradable axonal material (Gatzinsky and Berthold, 1990; Gatzinsky et al., 1997). This seems to be particularly important during aging and peripheral neuropathies.

1.1.3 Molecular domains of myelinated axons

Myelinated axons are composed of distinct molecular domains that result from complex axonal interactions with polarized myelinating Schwann cells (Pereira et al., 2012). Hence, the inner (adaxonal) Schwann cell membrane and the underlying axolemma are organized into node, paranode, juxtaparanode, and internode. Each of these regions comprises specific ion channels, cell adhesion molecules and cytoskeletal adaptor proteins (Arroyo and Scherer, 2000; Salzer et al., 2008; Faivre-Sarrailh and Devaux, 2013). This molecular and functional differentiation provides the basis for fast signal propagation and reduced energy consumption through saltatory conduction (Tasaki 1939). Disruption of axo-glial interaction leads to severe alterations in the molecular and structural organization of axons, including shifted ion channel distribution (Dupree et al., 1999; Bhat et al., 2001; Ishibashi et al., 2002; Rios et al., 2003).

Nodes of Ranvier are short (~1 μm) interruptions in the myelin sheath, where action potentials are generated (Huxley and Stämpeli, 1949; Waxman and Ritchie, 1985). Therefore, they are highly enriched in voltage-gated sodium ($\text{Nav}1.6$; Salzer et al., 2008) and potassium ($\text{Kv}7.2$; Devaux et al., 2004) channels. The assembly and the maintenance of nodal ion channels is controlled by axonal cell-adhesion molecules (CAMs) *NrCAM* and *neurofascin 186* (NF186; Davis et al., 1996). NF186 further interacts with gliomedin, which is secreted by Schwann cell microvilli to promote node formation (Eshed et al., 2005; Labasque et al., 2011). The whole complex is stabilized and linked to the axonal cytoskeleton via scaffolding proteins *ankyrin G* (ANKG; Jenkins and Bennett, 2002) and *β IV spectrin* (Fig. 3A; Komada and Soriano, 2002; Yang et al., 2004). Nodes are flanked by paranodal loops that form axo-glial septate-like junctions (transverse bands), attaching the myelin sheath to the axon (Rosenbluth, 2009). Paranodal junctions are formed by a complex of axonal *contactin/contactin-associated protein* (CASPR) and glial *neurofascin 155* (NF155; Einheber et al., 1997; Boyle et al., 2001; Bhat et al., 2001; Rios et al., 2003). This complex is further anchored to the axonal cytoskeleton via 4.1B protein (Fig. 3B; Cifuentes-Diaz et al., 2011). Paranodal junctions provide a partial diffusion barrier between the node and the juxtaparanode. Thereby, the electrical activity is separated from the internodal region, and lateral diffusion of axonal membrane proteins is prevented (Rios et al., 2003; Rosenbluth, 2009). Accordingly, disruption of paranodal junctions provokes a

displacement of juxtapanodal proteins into the paranode (Boyle et al., 2001; Bhat et al., 2001; Ishibashi et al., 2002).

The juxtapanode is located underneath the compact myelin sheath, adjacent to the paranodal region (Arroyo and Scherer, 2000). It is enriched in delayed rectifier Shaker-type K^+ channels, mainly composed of $K_v1.1/K_v1.2$ heteromultimers and their cytoplasmic $K_v\beta 2$ subunit (Wang and Tempel, 1993; Rasband et al., 1998). These voltage-gated K^+ channels are supposed to be important for stabilizing conduction and maintaining the internodal resting potential, thereby ensuring nerve excitability (Sherratt et al., 1980; Smart et al., 1998; Vabnick et al., 1999; Chi and Nicol, 2007). During myelination, K^+ channels are clustered at around P14 dependent on the axonal adhesion molecule CASPR2 (Poliak et al., 1999; Hivert et al., 2016). Juxtapanodal anchoring and maintenance are further mediated by interaction of CASPR2 with the GPI-anchored *transient axonal glycoprotein-1* (TAG-1 or Contactin-2) that is expressed by both Schwann cells and axons (Fig. 3C; Traka et al., 2002; Poliak and Peles, 2003; Savvaki et al., 2010). It has been shown that juxtapanodal localization of CASPR2 and TAG-1 is interdependent and deficiency in either protein causes a localization of K^+ channels evenly distributed along internodes (Poliak and Peles, 2003).

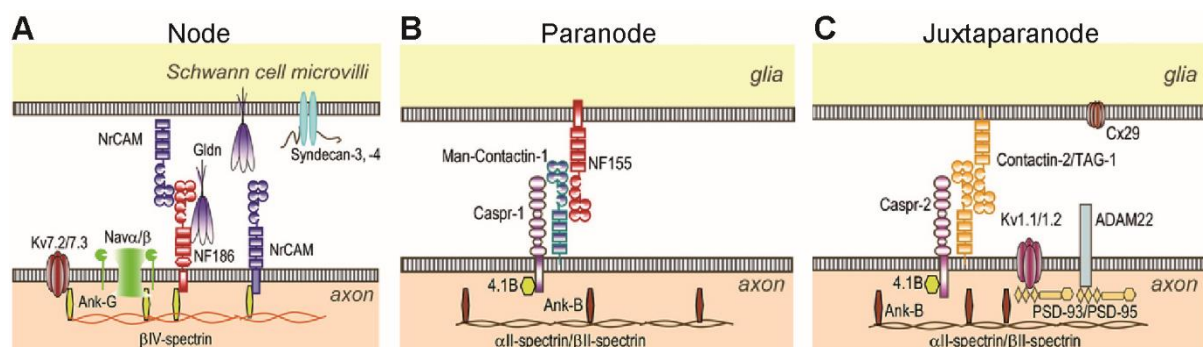


Fig. 3: Molecular organization of myelinated peripheral nerve fibers

A node of Ranvier (A), the paranode (B), and the juxtapanode (C) contain distinct ion channels, cell adhesion molecules and cytoskeletal adaptor proteins. (modified from Faivre-Sarrailh et al., 2013)

1.1.4 Ganglioside metabolism and function

Gangliosides are acidic glycosphingolipids that contain sialic acids and are most abundant in the nervous system (Sonnino et al., 2006; Schnaar et al., 2014). They are synthesized from ceramide in the Golgi apparatus and are further transported through vesicles towards plasma membranes (Maccioni, 2007). Gangliosides are primarily located in the outer leaflet of plasma membranes, where they form and stabilize lipid rafts through lateral segregation (Prioni et al., 2004; Schnaar et al., 2014). During brain development, complex gangliosides are synthesized by sequential addition of sialic acids to the simple GM3 ganglioside via glycosyl- and sialyltransferases. Dependent on the number of sialic acid residues they are further divided into 0-, a-, b- and c-series gangliosides (Garratt et al., 2000; Yu et al., 2011). However, the adult nervous system is highly abundant in a-series (GM1 and GD1a) and b-series (GD1b and GT1b) gangliosides (Fig. 4A; Tettamanti et al., 1973).

Gangliosides substantially regulate membrane organization, intercellular adhesion, and signaling (de Chaves and Sipione, 2010; Schnaar et al., 2014). Moreover, they are critical for axo-glial interactions. Accordingly, ablation of complex gangliosides results in central and peripheral demyelination and axonal degeneration (Sheikh et al., 1999; Ma et al., 2003; Pan et al., 2005). Furthermore, GM1 and GD1a are particularly essential for molecular organization and maintenance of myelinated axons (Fig. 4B). Thus, GM1 is highly abundant at paranodes, facilitating paranodal junction formation through glial NF155 and axonal CASPR (Howell et al., 2006; Susuki et al., 2007). Strong evidence implies that GM1 influences juxtaparanodal clustering of Kv1.1 by interacting with TAG-1 (Kasahara et al., 2000; Loberto et al., 2003; Labasque and Faivre-Sarrailh, 2010). In addition, myelin stability and axonal integrity is influenced by the interaction of axonal gangliosides (GD1b and GT1b) with MAG (Fig. 4B; Pan et al., 2005). A major role of gangliosides for nervous system integrity is further illustrated by Guillain-Barré syndromes (GBS). This group of autoimmune disorders is caused by immune responses against axonal or Schwann cell gangliosides, leading to severe peripheral neuropathies (Hughes and Cornblath, 2005; Kaida et al., 2009; van Doorn et al., 2008). Furthermore, deficiencies of ganglioside catabolism manifest as lysosomal storage disorders (Jeyakumar et al., 2005; Ballabio et al., 2009; Platt et al., 2012).

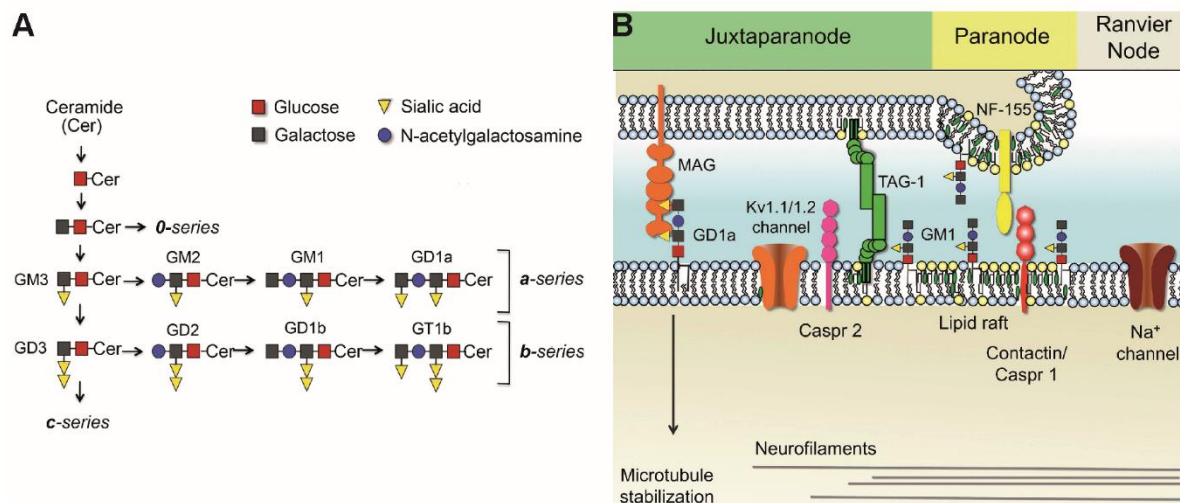


Fig. 4: Synthesis of brain gangliosides and their function in axo-glia interaction at nodes

A) Biosynthesis of complex brain gangliosides (a- and b-series) from ceramide.

B) Gangliosides regulate axo-glia interaction and membrane organization at nodes of Ranvier.

(adapted from Chaves et al., 2010)

1.2 Lysosomes in the nervous system

Lysosomes are electron dense, acidic organelles that are indispensable for the degradation of extracellular and intracellular material that is taken up by endocytosis or autophagy. Thus, lysosomes are highly involved in lipid metabolism and membrane dynamics (Singh et al., 2009; Settembre et al., 2014). Their consequential importance for myelin maintenance is emphasized by lysosomal disorders that frequently display a neurodegenerative phenotype accompanied with demyelination (Jeyakumar et al., 2005; Faust et al., 2010).

1.2.1 The endosomal-autophagic-lysosomal system

Protein degradation and recycling is essential for membrane dynamics and cellular integrity. Thus, the endosomal-autophagic-lysosomal system maintains cellular homeostasis and contributes to various cellular processes (Grant and Donaldson, 2009; Hu et al., 2015). Deficiencies in this system are associated with neurodegenerative diseases such as Alzheimer's and Parkinson's disease or lysosomal storage disorders (Vellodi, 2005; Rubinsztein, 2006; Neefjes and van der Kant, 2014).

The endosomal-lysosomal system forms a highly dynamic and interconnected network of distinct specialized membrane-enclosed compartments (Fig. 5; Hu et al., 2015). Extracellular material, membrane proteins, lipids, and ligands are internalized by endocytosis or phagocytosis and are transported to early endosomes via endocytic vesicles (Mousavi et al., 2004; Hu et al., 2015). Early endosomes (EE) are primarily located in the cellular periphery and are mainly involved in cargo sorting and recycling (Grant and Donaldson 2009). This is regulated by Rab GTPases (Huotari and Helenius, 2011). Thus, Rab5 mediates EE maturation and conversion to late endosomes (LE) by recruiting Rab7 (Meresse et al., 1995; Rink et al., 2005). Furthermore, endosome maturation includes a spectrum of morphological and molecular changes, such as acidification through vacuolar ATP-ase (Beyenbach and Wieczorek, 2006; Marshansky and Futai, 2008). Accordingly, mild pH in EE (6.8-5.9) enables conformational changes in proteins, whereas low pH in LE (6-4.9) and lysosomes (~4.5) facilitates hydrolysis and inactivation of pathogens (Maxfield and Yamashiro, 1987). During maturation, LE become round, acquire intraluminal vesicles, and move to perinuclear regions, where they undergo transient fusion to form multivesicular bodies (Huotari and Helenius, 2011). Finally, LE fuse with lysosomes to form endolysosomes, which are capable of degrading cargo through hydrolysis (Tjelle et al., 1996; Mullock et al., 1998). Lysosomal components (e.g. hydrolases and membrane proteins) are transported from the *trans*-Golgi network (TGN) to lysosomes by LE, primarily through mannose-6-phosphate receptor binding (Griffiths and Simons, 1986; Ghosh et al., 2003).

Lysosomes degrade intracellular material through autophagy (Fig. 5). This self-digestive pathway is activated by starvation, oxidative stress or protein aggregation to assure cellular integrity (Mizushima et al., 2003; Singh et al., 2009; Huang et al., 2011). Accordingly, dispensable or damaged organelles, misfolded proteins, and foreign microorganisms are degraded through autophagy, which can be inhibited by mTOR signaling (Noda and Ohsumi, 1998; Levine and Kroemer, 2008; Jung et al., 2010). The pathway is initiated by the formation of an isolation membrane (phagophore) that further engulfs cytoplasmic material. By this procedure a double-membranous autophagosome is generated, which fuses with lysosomes to form an autolysosome that is capable of degrading sequestered material (Levine and Kroemer, 2008).

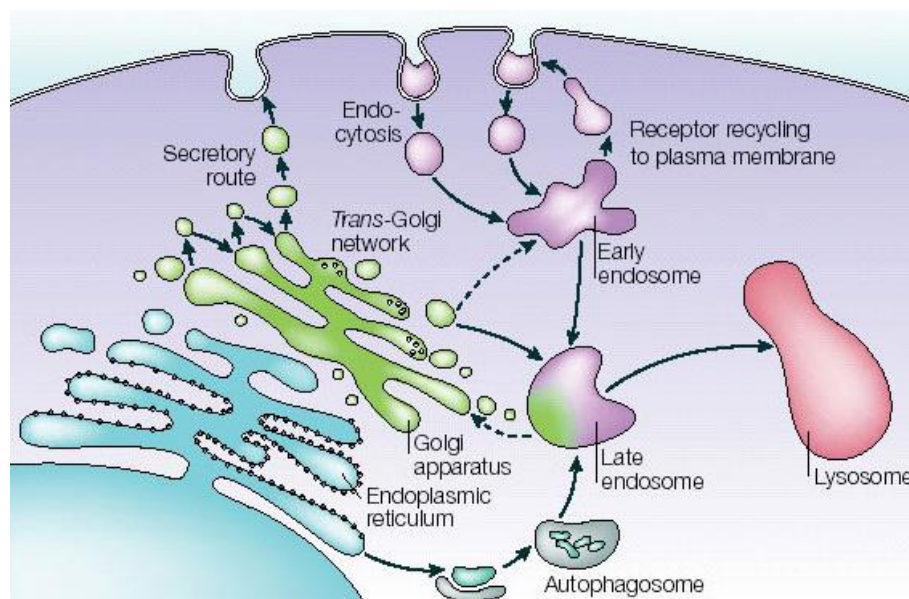


Fig. 5: The endosomal-autophagic-lysosomal system

Extracellular material is endocytosed and transported by the endocytic pathway either to lysosomes for degradation, or to early endosomes for recycling. Intracellular material is degraded by lysosomes through the autophagy pathway (taken from Jeyakumar et al., 2005)

1.2.2 Lysosomal storage disorders

Lysosomal storage disorders (LSDs) are single gene defects that are predominantly caused by deficiencies in lysosomal hydrolases. Consequently, their target substrates start to accumulate first within lysosomes and later also in other cellular compartments (Vellodi, 2005; Platt et al., 2012). It is suggested that lysosomes enlarge and increase in number to compensate this accumulation (Levine and Kroemer, 2008; Jeyakumar et al., 2005). Autophagy is severely reduced upon lysosomal storage (Settembre et al., 2008). As a result, cellular homeostasis is altered and other organelles, such as mitochondria and peroxisomes, are impaired (Schedin et al., 1997; Haq et al., 2006; Jennings et al., 2006; Ballabio et al., 2009). This subsequently causes CNS neurodegeneration and inflammation already in early childhood (Wraith, 2002; Vitner et al., 2010). Accordingly, lysosomal storage disorders account for about 45% of cases with infantile neurodegeneration (Verity et al., 2009).

One of the best-studied group of lysosomal storage disorders are glycosphingolipidoses, such as Gaucher disease, GM1 gangliosidosis, Tay-Sachs disease or metachromatic leukodystrophy (Levine and Kroemer, 2008; Jeyakumar et al., 2005). Studies on these disorders showed that sphingolipid trafficking and recycling

is highly impaired (Chen et al., 1999). Furthermore, distribution of lipid raft-associated proteins is potentially altered, resulting in signaling defects (Levine and Kroemer, 2008; Jeyakumar et al., 2005, Ballabio et al., 2009). Moreover, glycosphingolipid storage changes calcium homeostasis and could elicit an unfolded protein response and inflammatory responses (Korkotian et al., 1999; Jeyakumar et al., 2003; Tessitore et al., 2004). Together, these alterations affect neuronal integrity and results in neurodegeneration.

1.3 Peroxisomes in the nervous systems

Peroxisomes are ubiquitous, single membrane-enclosed organelles that are highly abundant in all nervous system cell types. Due to their small size in the brain, they are also termed “microperoxisomes” (De Duve and Baudhuin, 1966; Kassmann, 2014). Interestingly, they show a broad heterogeneity suggesting distinct functions within different cell types of the nervous system (Ahlemeyer et al., 2007). Nevertheless, peroxisomes are rather associated with myelin than axons in peripheral nerves (Kassmann et al., 2011). Peroxisomal disorders frequently show considerable alterations of the nervous system, indicating the crucial function of peroxisomes for myelin maintenance and axonal integrity (Steinberg et al., 2006; Wanders and Waterham, 2006; Barry et al., 2013). This is most probably due to their particular role in lipid metabolism and scavenging of reactive oxygen species (Wanders and Waterham, 2006).

1.3.1 Peroxisome biogenesis

Modes of peroxisome biogenesis were highly debated during the last decades. Whereas the model of autonomous division through growth and fission is well accepted (Schrader et al., 2012), data supporting *de novo* generation of peroxisomes from the endoplasmic reticulum (ER) is still contradictory (Ma et al., 2011; Nuttall et al., 2011). Due to a lack of own DNA, all peroxisomal proteins are nuclear-encoded and have to be shuttled into peroxisomes (Alberts et al., 2002). The majority of peroxisomal

membrane proteins (PMPs, class I) are directly imported into peroxisomes dependent on PEX19, PEX3 and PEX16 (Fig. 6A; Ghaedi et al., 2000; Fang et al., 2004; Matsuzaki and Fujiki, 2008). Only a minor portion of PMPs (class II) is independent on PEX19 and is supposed to require ER contribution (Hoepfner et al., 2005; Kim et al., 2006; van der Zand et al., 2010). Peroxisomal matrix proteins are synthesized on cytosolic ribosomes and are imported post-translationally into peroxisomes (Goldman and Blobel, 1978). This peroxisomal protein import depends on specific peroxisomal targeting signals (PTS1, C-terminal or PTS2, N-terminal; Gould et al., 1987; Swinkels et al., 1991). The majority of matrix proteins (> 90%) contains a PTS1, which is recognized by the cytosolic PEX5 protein (Gould and Valle, 2000; Stanley et al., 2006). After receptor-cargo binding, PEX5 associates with the docking complex (mainly PEX14 and PEX13) in the peroxisomal membrane (Fig. 6B; Platta and Erdmann, 2007; Meinecke et al., 2010). In contrast to other organelles, peroxisomes are capable of importing folded and oligomeric proteins (McNew and Goodman, 1994). After protein translocation, PEX5 is released and recycled or degraded (Platta et al., 2007).

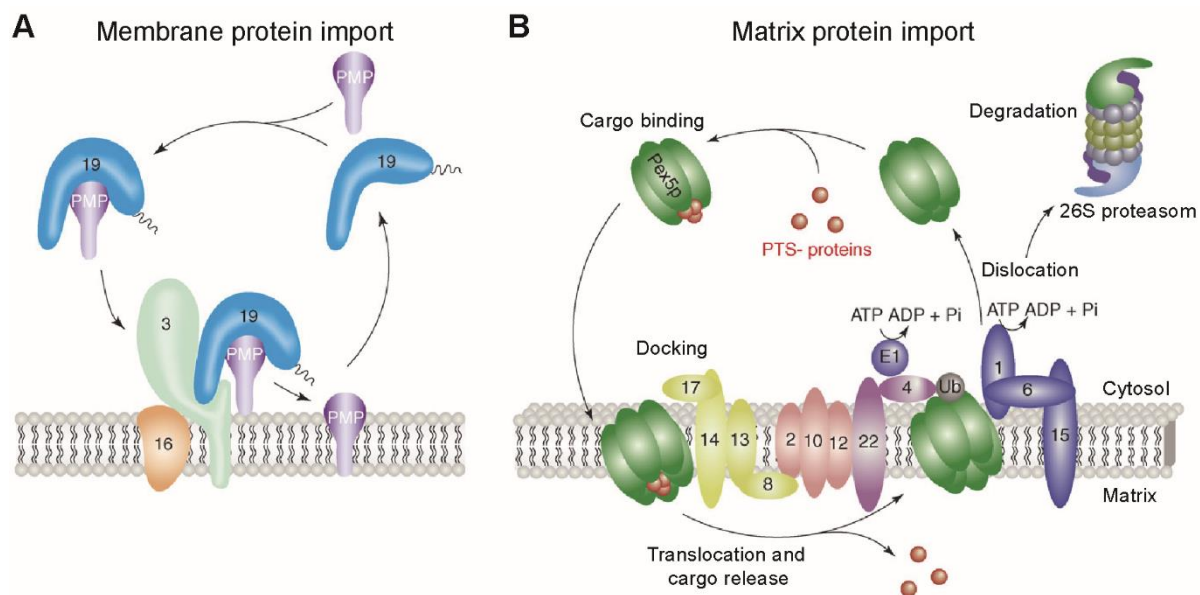


Fig. 6: Peroxisomal protein import

A) The import of most peroxisomal membrane proteins depends on PEX19, PEX3 and PEX16.

B) The majority of peroxisomal matrix proteins are imported via PEX5 through PTS1 recognition.

(adapted from Platta and Erdmann 2007)

1.3.2 Peroxisomal lipid metabolism

The importance of peroxisome function for human physiology is emphasized by fatal consequences of peroxisomal defects (Wanders, 2004a; Steinberg et al., 2006). Accordingly, patients with peroxisomal β -oxidation defects frequently phenocopy symptoms of patients with biogenesis defects (Baes and van Veldhoven, 2012). Like mitochondria, peroxisomes are capable of degrading fatty acids (FA) through β -oxidation (Reddy and Mannaerts, 1994; Wanders and Waterham, 2006). These fatty acids either derive from exogenous diet or endogenous lipid breakdown, for example in lysosomes. Notably, peroxisomes and mitochondria have certain substrate specificities. Thus, pristanic acids, long-chain dicarboxylic acids, di- and trihydroxycholestanic acids (DHCA and THCA), and very-long-chain fatty acids (VLCFA, $\geq C22$) are solely degraded by peroxisomal β -oxidation (Wanders, 2004a). Briefly, it starts with dehydrogenation of CoA-esters by two acyl-CoA oxidases (ACOX1/2), followed by hydration and another dehydrogenation performed by an enoyl-CoA hydratase (D-bifunctional protein, DBP or multifunctional protein, MFP2). Finally, fatty acids are cleaved by thiolases (ACAA1, SCPx). Unlike mitochondria, peroxisomes can only chain-shorten fatty acids and their products have to be further degraded by mitochondria (Bremer and Norum, 1982). Furthermore, hydrogen peroxide (H_2O_2) and other reactive oxygen species (ROS) are produced as by-products of beta-oxidation. Hence, peroxisomes contain several reducing enzymes, such as catalase, superoxide dismutase (SOD1), and glutathione peroxidase to prevent oxidative stress (Singh et al., 1994; Schrader and Fahimi, 2004). Besides fatty acid beta-oxidation, peroxisomes are involved in the synthesis of for example bile acids, docosahexaenoic acids, and plasmalogens (Brites et al., 2004). The latter are ether phospholipids, highly abundant in myelin (Braverman et al., 2012).

1.3.3 Peroxisomal disorders and their impact on the nervous system

Peroxisomal disorders are basically divided into single enzyme or protein deficiencies and biogenesis defects (Gould and Valle, 2000; Steinberg et al., 2006; Wanders and Waterham, 2006). The latter most notably comprises the Zellweger spectrum disorders, of which the Zellweger syndrome is the most severe (Bowen et al., 1964). It is caused by mutations in various *PEX* genes, especially *PEX1* (Reuber et al., 1997).

Since peroxisomes are ubiquitous organelles, Zellweger patients display multiple congenital defects in almost every organ system. Neurological alterations include neuronal migration defects, eye abnormalities, and absence of deep tendon reflex (Steinberg et al., 2006). Patients are mainly diagnosed through elevated VLCFA plasma levels and deficient erythrocyte plasmalogens (Wanders, 2004b). Due to their severe symptoms, affected children usually die within the first year after birth.

X-linked adrenoleukodystrophy (X-ALD) is the most frequent single peroxisomal protein disorder in children (Bezman and Moser, 1998; Berger and Gärtner, 2006). It is caused by loss-of-function mutations in the X-chromosomal *ABCD1* gene, which encodes a peroxisomal ATP-binding cassette transporter protein (ABCD1; Mosser et al., 1993). ABCD1 imports CoA-activated VLCFA into peroxisomes (van Roermund et al., 2008; Wiesinger et al., 2013). Consequently, X-ALD patients show elevated levels of especially C26:0 fatty acids due to impaired peroxisomal β -oxidation (Kemp and Wanders, 2010; Wiesinger et al., 2013). Although, VLCFA accumulation is supposed to trigger various cytotoxic effects (Singh and Pujol, 2010; Berger et al., 2014), the underlying molecular mechanism that eventually causes myelin abnormalities, axon degeneration and neuroinflammation are still under investigation. Furthermore, there is no general genotype-phenotype correlation and the disease shows a high phenotypic variance (Moser et al., 2007; Ferrer et al., 2010). Thus, patients may display one of two major clinical phenotypes: The cerebral childhood form (CCALD) is characterized by early-onset and fast progressive inflammatory cerebral demyelination, while adrenomyeloneuropathy (AMN) is a late-onset, slowly progressive disease mainly affecting spinal cord and peripheral nerves (Engelen et al., 2012). To better understand the molecular mechanisms that induce neurodegeneration, ABCD1-deficient mice have been generated by three independent groups (Forss-Petter et al., 1997; Kobayashi et al., 1997; Lu et al., 1997). These mice develop late-onset AMN-like symptoms, but fail to show cerebral demyelination or neuroinflammation (Forss-Petter et al., 1997; Lu et al., 1997; Pujol et al., 2002).

To study the role of peroxisomes, especially in the nervous system, cell type-specific mouse models have been generated (Baes and van Veldhoven, 2012). Depletion of peroxisomes from all neural progenitor cells, using the *Nes-Cre::Pex5^{flox/flox}* mice, results in severe neuropathological symptoms including de- and dysmyelination, axon loss and neuroinflammation (Hulshagen et al., 2008). Astonishingly, those

characteristics are absent in mice with peroxisome-deficient neurons (*Nes-Cre::Pex5^{flox/flox}* mice) or astrocytes (*Gfap-Cre::Pex5^{flox/flox}* mice; (Bottelbergs et al., 2010). These results suggest rather a minor role for peroxisomes especially in neurons, which might potentially be explained by the fact that myelinating glia provide trophic support for axons (Nave, 2010b; Fünfschilling et al., 2012). In line with this hypothesis, ablation of functional peroxisomes from oligodendrocytes (*Cnp-Cre::Pex5^{flox/flox}* mice) results in neuropathological symptoms comparable to *Nes-Cre::Pex5^{flox/flox}* mice. In detail, *Cnp-Cre::Pex5^{flox/flox}* mice show axonal loss, cerebral demyelination and neuroinflammation (Kassmann et al., 2007). Later studies of *Cnp-Cre::Pex5^{flox/flox}* mice further revealed a peripheral neuropathy, characterized by secondary axonal loss, reduced nerve conduction velocity, and muscle dystrophy. Moreover, these mice develop pathologically enlarged paranodes and axonal swellings, containing vesicular accumulations (Kassmann et al., 2011). Thus, the comparison of the different conditional PEX5 knockout mouse models highlights the essential function of peroxisomes in myelinating glial cells and demonstrates the importance of glial lipid metabolism for axonal integrity.

1.4 Aim of this study

Axonal integrity relies on metabolic support by myelinating glial cells. A role for myelin-associated peroxisomes to facilitate this particular function became evident from the specific ablation of peroxisomal function from oligodendrocytes and Schwann cells in mice (*Cnp-Cre::Pex5^{flox/flox}*). Considering peroxisomal abundance within Schwann cells, especially at non-compacted regions, we hypothesized a role for peroxisomal lipid metabolism in SC-mediated axonal support. Accordingly, we checked for disturbed axo-glial interactions and axonal alterations as possible results of peroxisomal dysfunction. Studies of *Cnp-Cre::Pex5^{flox/flox}* mice revealed a crucial role of peroxisomes in myelin maintenance and axonal integrity for the CNS. Therefore, the first aim of this thesis was to examine, whether peroxisomal dysfunction in SC provokes comparable demyelination and neurodegeneration in the PNS. To this end, structural and molecular analysis of myelin, as well as investigation of axonal distribution, was performed on sciatic nerves. Also, functional sensory and motor nerve impairment was assessed by electrophysiology and behavioral tests. Finding no considerable demyelination or axonal loss, but early-onset electrophysiological alterations, the second and major part of this project was to examine potential defects of axo-glial interaction and their impact on the molecular organization of nodes of Ranvier. The detection of ectopic ion channels and their corresponding anchor proteins drew attention to the metabolism and the distribution of gangliosides, lipids important for the normal juxtaparanodal localization of these proteins. Given the fact that the fraction of VLCFA-bound gangliosides was abnormally enriched and gangliosides were accumulated in cellular vesicles reminiscent of lysosomal storage disorders, we suspected secondary alterations of the endosomal-lysosomal compartment due to deficient peroxisomal β -oxidation. Hence, fluorescent teased fiber staining, enzyme activity tests, and electron microscopy were performed to analyze the origin of vesicles of paranodal swellings. Although the *Cnp-Cre::Pex5^{flox/flox}* mouse model is eligible to investigate the role of peroxisomes in SC, it is not directly related to human peroxisomal defects. To finally transfer our findings to a more disease-related model, ABCD1-deficient mice were comparatively analyzed with respect to the neuropathological phenotype.

2. Results

2.1 Ablation of PEX5 from Schwann cells

2.1.1 Disturbed import of peroxisomal proteins

Cnp-Cre mediated ablation of peroxin 5 (PEX5) from myelinating cells was used to study the function of peroxisomes for myelination and axon integrity. As PEX5 is the major import receptor of peroxisomal proteins, PEX5-deficient cells lack the majority of enzymes within peroxisomes, resulting in a complete disruption of peroxisome function (Gould and Valle, 2000). Peroxisomes are highly abundant in the myelin compartment and PEX5-deficiency in oligodendrocytes causes severe myelin and axon alterations (Kassmann et al., 2007). To prove excision of PEX5 also from Schwann cells (SC), polymerase chain reaction (PCR) on tail DNA was performed. Effective Cre-mediated recombination was evidenced by a 340 bp amplicon, which was absent in control animals (Fig. 7A). *Pex5* mRNA expression was reduced by 50% in sciatic nerve lysates as indicated by quantitative real-time PCR (Fig. 7B). Remaining mRNA expression likely resulted from non-Schwann cell nuclei in the PNS. To verify the functional lack of PEX5 from Schwann cells, teased sciatic nerve fibers were fluorescently stained for *peroxisomal membrane protein 70* (PMP70), and the intra-peroxisomal enzyme, catalase. The two proteins showed a punctate pattern and high degree of colocalization especially around SC nuclei in control nerves. In contrast, PEX5-deficient nerves showed less PMP70-positive puncta and revealed cytoplasmic localization of catalase (Fig. 7C). This observation indicates defective import of peroxisomal proteins, resulting in 'peroxisomal ghosts' due to PEX5 disruption (Fig. 7D).

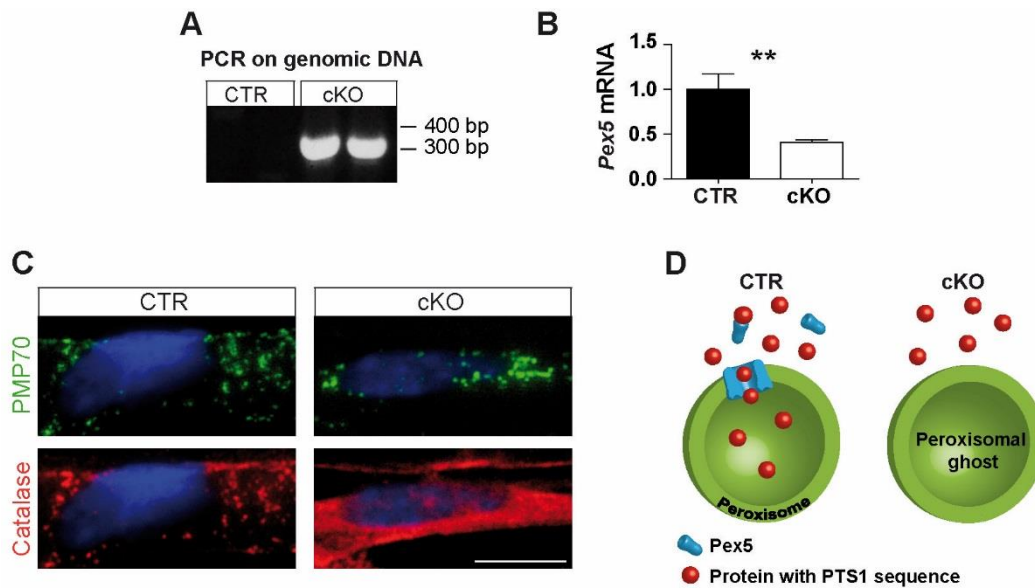


Fig. 7: PEX5 ablation from Schwann cells disrupts import of peroxisomal proteins

A) Polymerase chain reaction (PCR) on genomic DNA, isolated from mouse tails. Conditional mutants (cKO) show a band at 340 bp after Cre-mediated excision of *Pex5* floxed exons 11-14, which is absent in controls (CTR).

B) qRT-PCR on cDNA from total sciatic nerve lysates. mRNA expression of *Pex5* is reduced by 50% in conditional mutants (n=6 per genotype, error bars: mean + s.e.m, **p < 0.01, Student's T-test).

C) Immunofluorescent teased sciatic nerve fiber staining from 9 months old animals. *Peroxisomal membrane protein 70* (PMP70, green) and peroxisomal enzyme catalase (red) show punctate staining around Schwann cell nuclei (DAPI, blue) in controls. Conditional mutants show less PMP70-positive puncta and cytoplasmic catalase. Scale bar, 10 μ m.

D) Schematic model of normal (left) and disturbed (right) protein recognition and peroxisomal import by PEX5 via the peroxisomal targeting signal 1 (PTS1).

2.1.2 Disturbed peroxisomal lipid metabolism

Peroxisomes play an essential role in lipid metabolism (Wanders, 2004a). They exclusively degrade very long-chain fatty acids (VLCFA; Wanders and Waterham, 2006) and are involved in the synthesis of for example ether phospholipids (e.g. plasmalogens; Brites et al., 2004). Defects in either peroxisome biogenesis or single enzymes disturb peroxisomal function (Wanders, 2004b; Steinberg et al., 2006). Accordingly, patients with peroxisomal disorders frequently display reduced plasmalogen levels and/or accumulation of β -oxidation substrates, especially of VLCFA (Kemp and Wanders, 2010; Singh and Pujol, 2010).

To evaluate peroxisomal function in SC, lipid mass spectrometry was performed on sciatic nerve lysates of 9 months old animals. Plasmalogens were highly abundant in control nerves (Fig. 8A top, green arrows), whereas the same plasmalogens were hardly detectable in mutant nerves (Fig. 8A bottom, red arrows). Quantification of plasmalogen (PE_P) and its precursor alkylated phosphatidylethanolamines (PE_O) revealed a reduction of almost 70%. Accordingly and as reported from patients, phosphatidylethanolamines were increased 4-fold in mutant nerves (Fig. 8B). Besides reduced plasmalogen levels, accumulation of especially VLCFA (C26:0 and C24:0 respectively) is a key feature of peroxisomal disorders (Poulos et al., 1988; Engelen et al., 2012). Lipid mass spectrometry showed a significant increase of cholesterol in membrane fractions (Fig. 8C) as well as elevated C26/C22 and C26/24 ratios in nerve lysates (Fig. 8D). Taken together, these data confirm peroxisomal dysfunction due to PEX5-deficiency in myelinating SC.

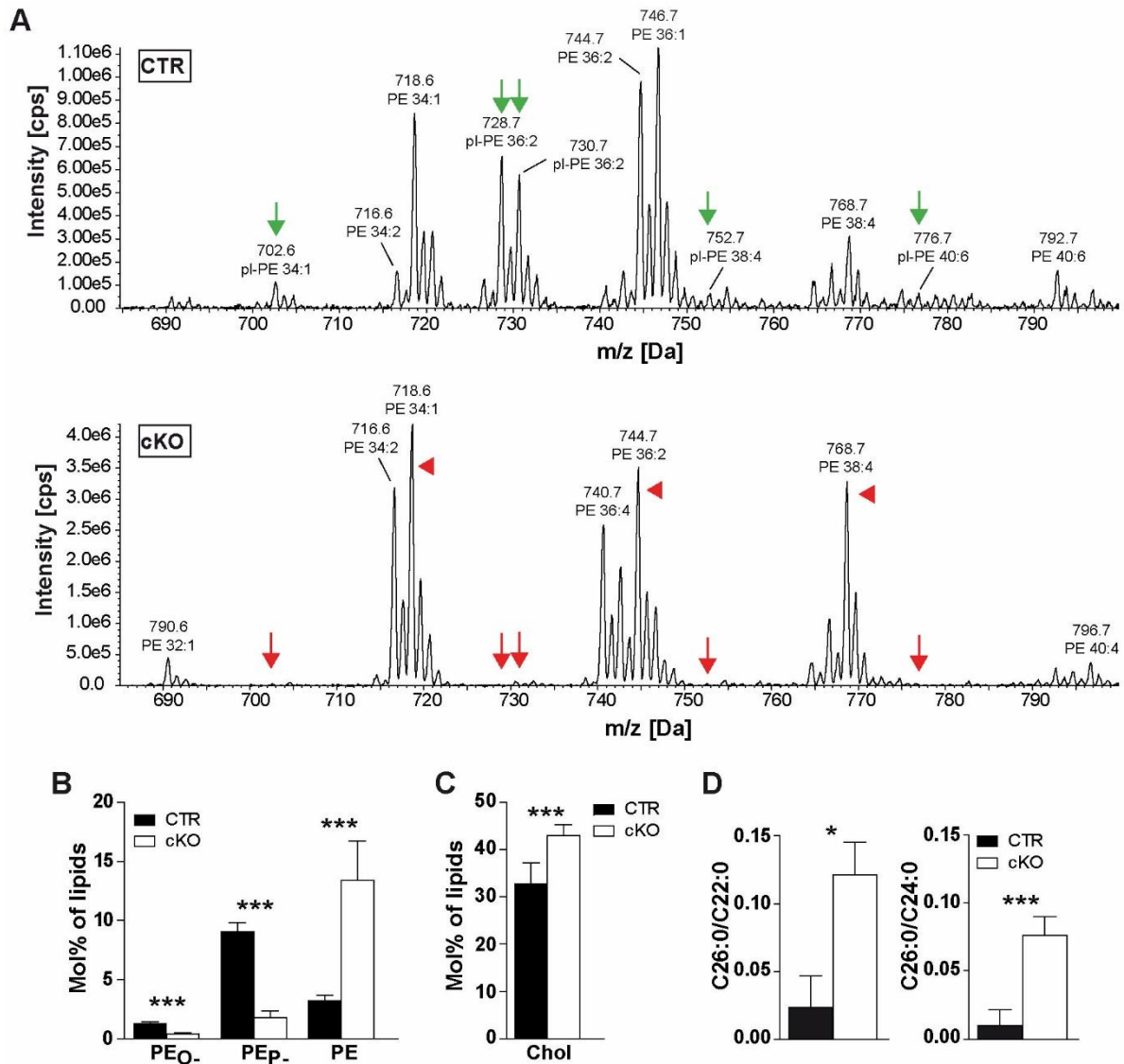


Fig. 8: PEX5 ablation from Schwann cells disturbs peroxisomal lipid metabolism

A) Quantitative lipid mass spectrometry of sciatic nerve lysates from 9 months old mice. Plasmalogens (pl-PE) are abundant in control nerves (top, green arrows), whereas mutant nerves lack those plasmalogens (bottom, red arrows) and have increased peaks of phosphatidylethanolamines (PE, red arrow heads).

B) Quantification of lipid mass spectrometry. Plasmalogen (PE_P) and its precursor alkylated phosphatidylethanolamines (PE_O) are significantly reduced, whereas phosphatidylethanolamines (PE) are increased 4-fold in mutant nerves. (n=6 per genotype, error bars: mean + s.e.m, ***p < 0.005, Student's T-test).

C) Lipid mass spectrometry reveals significantly elevated cholesterol levels in membrane fractions of 9 months old *Cnp-Cre::Pex5^{flx/flx}* sciatic nerves. (n=6 per genotype, error bars: mean + s.e.m, ***p < 0.001, Student's T-test).

D) Mass spectrometry of very long-chain fatty acids (VLCFA, C26:0) in nerve lysates from 9 months old animals. Mutant nerves show significantly increased ratios of C26:0/C22:0 (left graph) and C26:0/C24:0 (right graph). (n=6 per genotype, error bars: mean + s.e.m, *p < 0.05, ***p < 0.001, Student's T-test).

2.2 Impact of peroxisomal dysfunction on nerve function

2.2.1 Electrophysiological analysis indicates early sciatic nerve dysfunction

PEX5 conditional mutants start to develop neurological impairment (e.g. ataxia) already at 3 months of age (Kassmann et al., 2007). *In vivo* sciatic nerve recordings revealed reduced nerve conduction velocities and decreased amplitudes that are likely related to the observed motor problems (Kassmann et al., 2011). To exclude a possible influence of a pathology of neuromuscular junctions as underlying cause of altered electrophysiology, we performed *ex vivo* electrophysiological recordings using nerves from 2 months old animals. Therefore, sciatic nerves were dissected and both ends engulfed by suction electrodes (Fig. 9A). Nerves were stimulated with different current intensities (0.13-0.3 mA). Compound action potentials (CAP) as well as nerve conduction velocity (NCV) were significantly decreased in mutant nerves. In detail, amplitudes were reduced by up to 30% at stimulation intensities above 0.15 mA and nerve conduction speed was diminished from approximately 38 m/s in controls to 28 m/s in mutants (Fig. 9B). Mutants also required higher stimulation intensities (155 μ A) compared to controls (135 μ A) to elicit a signal, indicating an elevated threshold (Fig. 9C). Moreover, responses of mutant nerves did not show a clear slope at stimulus intensities above 220 μ A and only reached a peak amplitude that was 50% less than that of controls (Fig. 9D).

In conclusion, PEX5-deficiency in SC causes massive nerve dysfunction already at 2 months of age, which is characterized by decreased amplitudes, increased latencies, and fast response saturation. Thus, *ex vivo* electrophysiology revealed functional nerve impairment already at an early stage of disease progression, before the onset of clinical features (Kassmann et al., 2007). In contrast, *in vivo* measurements resulted in less pronounced differences, which showed a reduction of amplitudes not earlier than at 6 months of age (Kassmann et al., 2011). Accordingly, the *ex vivo* approach is a more sensitive method to analyze nerve alterations in animal models than *in vivo* recordings.

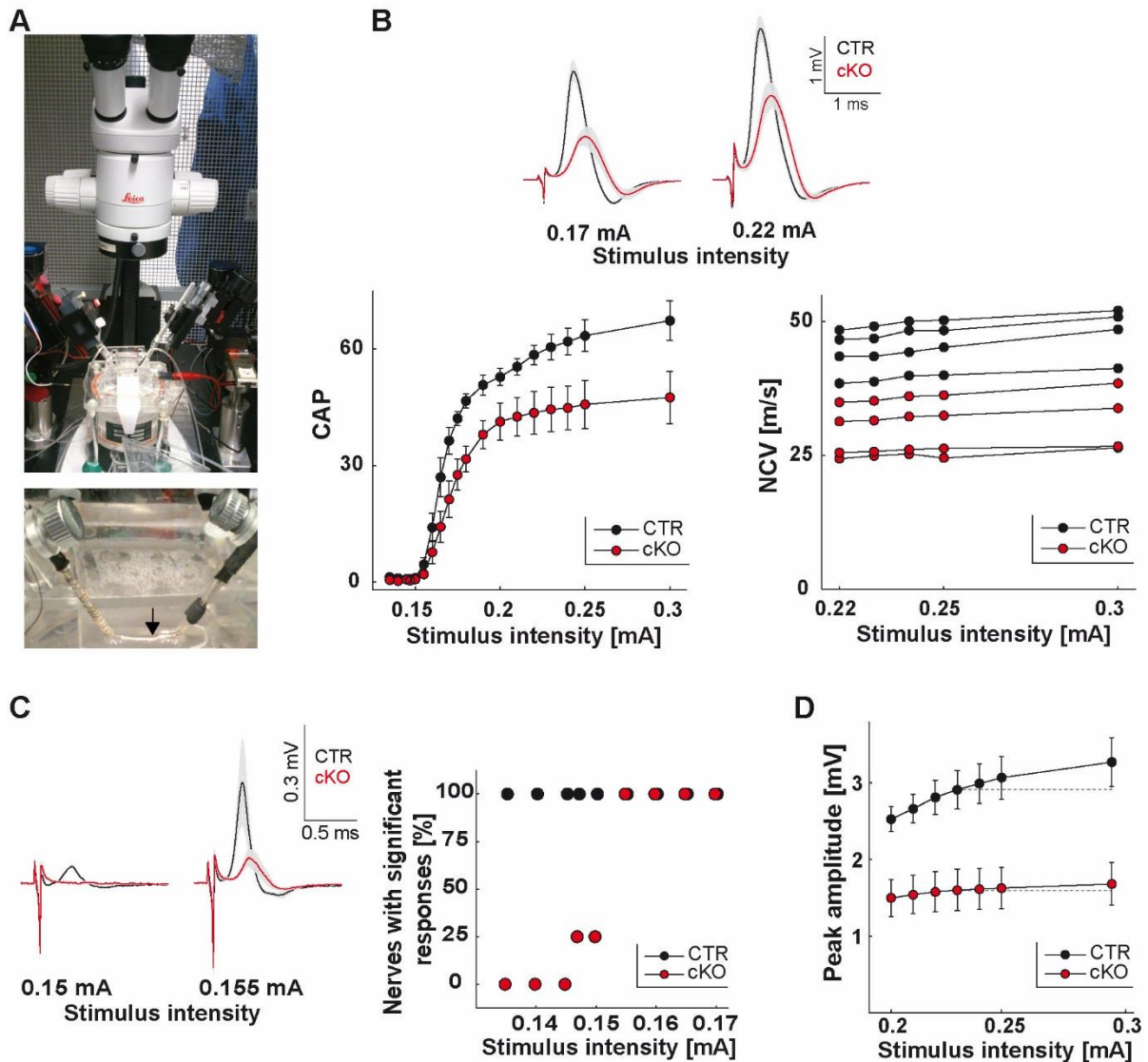


Fig. 9: Functional impairment in 2 months old *Cnp-Cre::Pex5^{flox/flox}* sciatic nerves

A) Image of *ex vivo* electrophysiology setup with two suction electrodes engulfing the dissected sciatic nerve (inset, arrow).

B) Representative nerve responses at stimulation intensities of 0.17 mA and 0.22 mA. Responses of conditional mutants (red) are slower and weaker, compared to control nerves (black). Quantification of compound action potentials (CAP) demonstrates a reduction of about 30% in mutant nerves and significantly reduced nerve conduction velocities (NCV, each curve represents mean nerve responses of one animal across intensities, n=4, error bars: means \pm s.e.m).

C) Mean sciatic nerve responses elicited with 0.15 mA and 0.155 mA stimulation intensities reveal highly reduced excitability in mutants. Percentage of nerves that show a significant response at low intensities (\leq 0.155 mA) is severely reduced in mutant nerves.

D) Peak amplitudes plotted against increasing stimulus intensity indicates earlier response saturation of mutant nerves. (n=4, error bars: means \pm s.e.m, two-way ANOVA).

2.2.2 Tendency of more neuromuscular junctions in aged *Cnp-Cre::Pex5^{flox/flox}*

Neuromuscular junctions (NMJs) transmit signals from peripheral nerves towards their innervating muscles. Moreover, they are highly dynamic and have a high capacity to compensate disease- or age-related alterations in muscle innervation (Naguib et al., 2002). Interestingly, *ex vivo* electrophysiology revealed functional impairment already early during disease progression (Fig. 9). Hence, less pronounced results from *in vivo* measurements may result from potential compensatory effects of NMJs. To investigate the number of NMJs, cryo sections of gastrocnemius muscles from 9 months old animals were stained for α -bungarotoxin, which irreversibly binds to nicotinic acetylcholine receptors (Fig. 10A; (Oswald and Freeman, 1981)). *Cnp-Cre::Pex5^{flox/flox}* muscles revealed a slight, however non-significant, increase of NMJs per mm² (Fig. 10B).

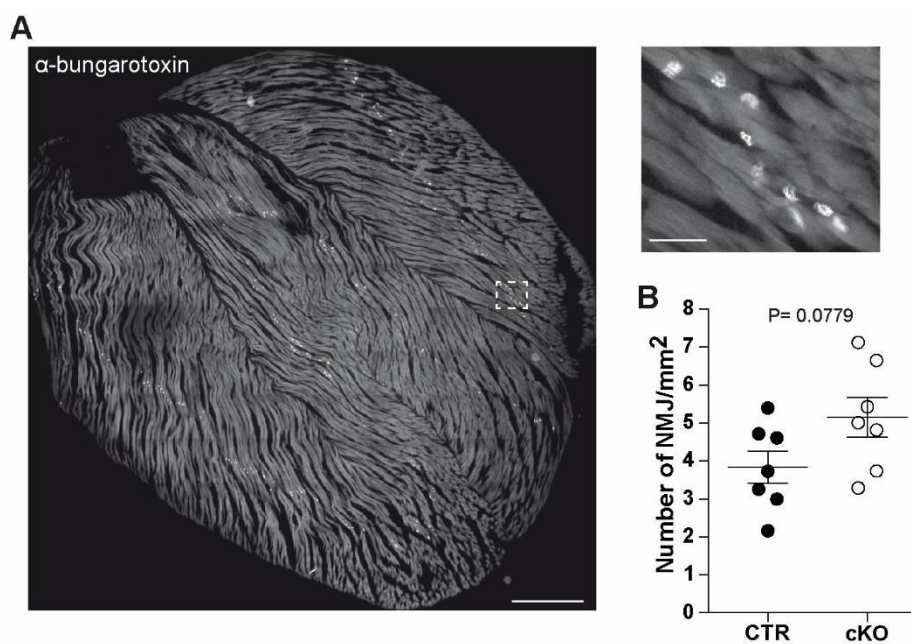


Fig. 10: Number of NMJs is slightly enhanced in gastrocnemius muscles of *Cnp-Cre::Pex5^{flox/flox}*

A) Representative image of immunofluorescent staining of neuromuscular junctions (NMJs) in cryo sections of gastrocnemius muscle, using α -bungarotoxin. NMJs are arranged in rows (inset). Scale bar, 1mm; 100 μ m (inset).

B) Quantification of the number of NMJs per mm² demonstrates a trend towards more NMJs in muscles of 9 months old *Cnp-Cre::Pex5^{flox/flox}* mice. (n=7, error bars: mean \pm s.e.m, p=0.078, Student's T-test).

2.2.3 Analysis of sensory impairment

Behavioral analysis of *Cnp-Cre::Pex5^{flox/flox}* mice revealed progressive motor impairment (Kassmann et al., 2007). Since sciatic nerves are composed of a mixture of sensory and motor fibers, the question arose whether sensory nerve fibers are affected as well. To this end, mechanical and thermal sensation was assessed in aged (> 9 mo) *Cnp-Cre::Pex5^{flox/flox}* and control mice (Fig. 11A-B). Conditional mutants showed a hypersensitivity in response to mechanical stimuli, indicated by their paw withdrawal already at lower force applications (Fig. 11A). In contrast, thermal stimulation with an infrared laser did not show comparable results. Here, mutant mice exhibited slightly delayed responses, which were highly variable and not significant (Fig. 11B). In summary, only the mechanical, but not the thermal test depicted sensory differences in conditional mutant mice. Together, both tests suggest discrete alterations of different sensory receptors.

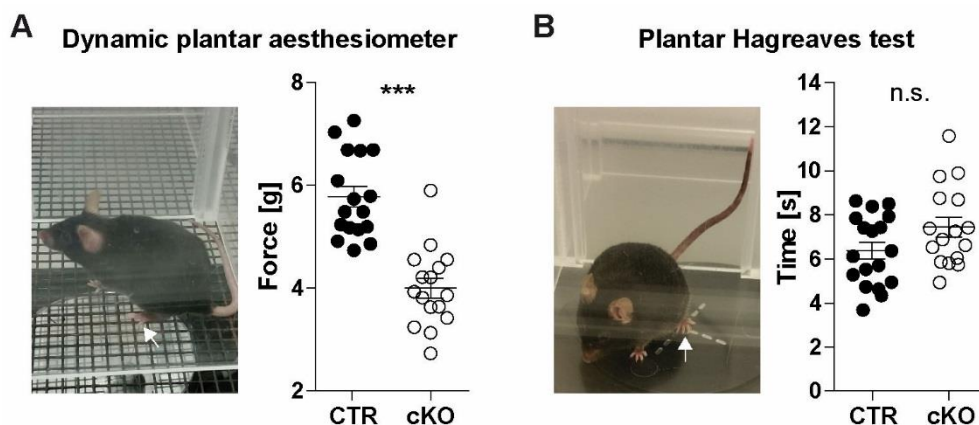


Fig. 11: Impaired pressure, but not heat sensation in 9 months old *Cnp-Cre::Pex5^{flox/flox}*

A) Behavioral assessment of pressure sensation using the dynamic plantar aesthesiometer. The mechanical sensitivity threshold of hind paws is determined by the use of electronic von Frey filaments (white arrow). Quantification of mechanical force that is needed to induce hind paw lifting reveals that conditional mutants respond at lower forces (4.006x g, white) than controls (5.779x g, black). (CTR n=17, cKO n=16; error bars: mean ± s.e.m, ***p < 0.001, Student's T-test).

B) Behavioral assessment of heat sensation using the plantar Hargreaves test. The sensitivity threshold is determined by stimulating the hind paw with an electronic punctual infrared heat (white arrow). Quantification of time that is needed to lift the hind paw shows comparable values for controls (6.37 s, black) and conditional mutants (7.44 s, white). (CTR n=18, cKO n=16, error bars: mean ± s.e.m, n.s. not significant, Student's T-test).

2.3 Impact of peroxisomal dysfunction on nerve integrity

2.3.1 No considerable demyelination or deficient myelin compaction

Peroxisomal defects are prone to cause myelin alterations (Steinberg et al., 2006; Faust et al., 2010; Hanson et al., 2014). This is in line with the fact that peroxisomes are highly associated with myelin sheaths and that their abundance and activity is enhanced during the peak of myelination (Adamo et al., 1986; Kassmann, 2014). Due to high lipid contents (>70% of dry mass) of myelin sheaths and the pivotal role of peroxisomes in lipid metabolism, peroxisomes are presumably important for myelin formation and maintenance (Adamo et al., 1986; Kassmann, 2014).

Cnp-Cre::Pex5^{flox/flox} mice develop progressive CNS demyelination, starting at around 4 months of age in the corpus callosum (Kassmann et al., 2007). Interestingly, we observed electrophysiological alterations of sciatic nerves already at 2 months of age (Fig. 9). To investigate, whether reduced nerve conduction velocities resulted from demyelination, ultrastructural and molecular analysis of sciatic nerves was performed. Semithin cross sections were stained for methylene blue/ azure II blue, to label the lipid-rich myelin sheaths. Examination of these complete nerve cross sections did not reveal apparent demyelination, neither in 2 months nor in severely affected 9 months old conditional mutants. However, axons with thinner myelin were occasionally observed in nerves from aged animals (Fig. 12A). To further evaluate myelin thickness, g-ratio analysis (axonal diameter divided by the complete fiber diameter) was performed on electron-microscopic images (Fig. 12B). Quantification of g-ratio demonstrated similar values for controls and conditional mutants at either age (2 and >9 months; Fig. 12C). Next, sciatic nerve cross sections were stained for P0, the most abundant myelin protein in the PNS (Greenfield et al., 1973), showing no obvious difference between controls and conditional mutants (Fig. 12D). Furthermore, electron microscopy of ultrathin cross sections demonstrated normal myelin compaction in 9 months old conditional mutant nerves (Fig. 13A). To investigate possible molecular differences, sciatic nerve lysates of 2 months old animals were analyzed by western blotting (Fig. 13B). This confirmed normal protein abundance of P0 in mutant nerves. Also, other important peripheral myelin proteins (P2 and PMP22) were normal. Only PLP comprising about 0.2% of all proteins in PNS myelin (Patzig et al., 2011), was significantly reduced by 42% (Fig. 13C).

These data suggest that electrophysiological changes are not provoked by deficient myelin compaction or myelin loss, particularly not during early disease progression. Moreover, in contrast to the CNS, where demyelination is an early consequence of peroxisome deficiency, peripheral nerves do not show considerable myelin alterations.

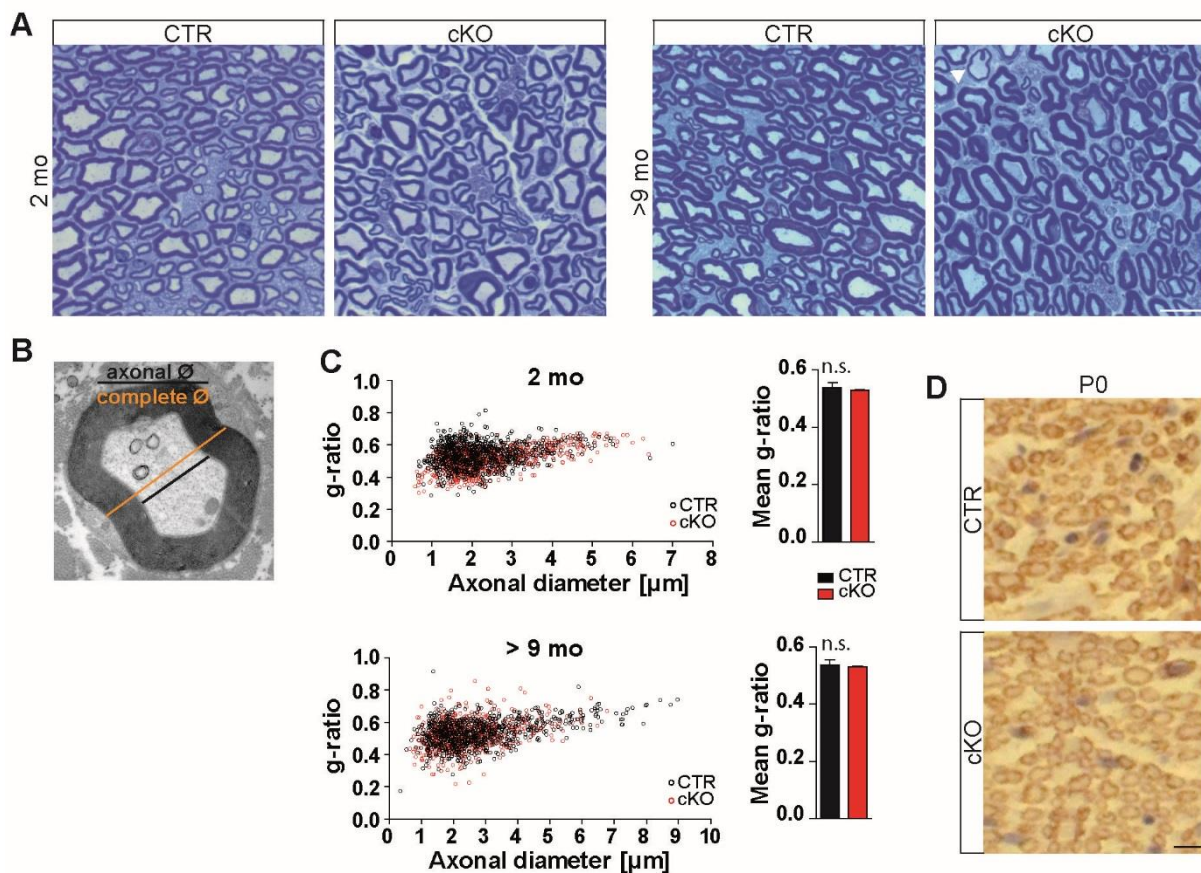


Fig. 12: Normal myelin thickness in *Cnp-Cre::Pex5^{lox/lox}* sciatic nerves

A) Methylene blue/ azur II blue stained semithin cross sections of sciatic nerves from 2 and > 9 months old mice occasionally depicts thinner myelin in aged conditional mutants (arrow head). Scale bar: 10 μm .

B) Principle of g-ratio analysis (axonal diameter divided by complete fiber diameter), a method to measure myelin sheath thickness.

C) g-ratio values are comparable between controls (black) and mutants (red) for all axonal diameters in young (2 mo) and aged (> 9 mo) nerves. Quantification of mean g-ratio depicts similar values for controls (2 mo, 0.533; >9 mo, 0.54) and mutants (2 mo, 0.51; >9 mo, 0.53). (n=3-4, ≥ 100 randomly chosen axons per animal, error bars: mean + s.e.m, n.s. not significant, Student's T-test).

D) Chromogenic immune-staining for myelin protein zero (P0) on paraffin-embedded sciatic nerve cross sections. Scale bar, 10 μm .

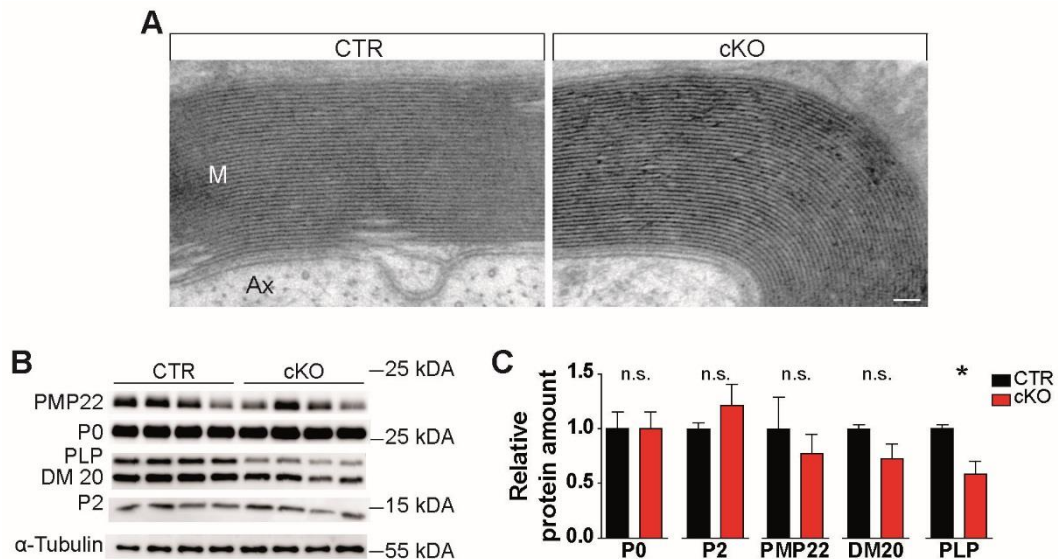


Fig. 13: Normal myelin compaction and protein composition in *Cnp-Cre::Pex5^{flox/flox}* sciatic nerves

A) Electron micrographs of sciatic nerve cross sections from 9 months old mice show normal myelin compaction in conditional mutant nerves. M, myelin; Ax, axon. Scale bar, 10 nm.

B) Western blot analysis of myelin protein abundance in sciatic nerve lysates from 2 months old mice. Alpha-tubulin was used as loading control.

C) Quantification of major peripheral myelin protein abundance (P0, P2, PMP22, and DM20, PLP) reveals only a significant reduction for PLP in mutant nerves. (n=4 per genotype, error bars: mean + s.e.m, n.s. not significant, *p < 0.05, Student's T-test).

2.3.2 Axon degeneration is not a substantial feature of sciatic nerve pathology

Myelinated axons depend on metabolic support by glial cells (Nave, 2010a; Fünfschilling et al., 2012). It has been shown that peroxisome-deficient oligodendrocytes fail to maintain axon integrity, resulting in axon degeneration independent of demyelination (Kassmann et al., 2007). Furthermore, electrophysiological recordings revealed reduced amplitudes already at 2 months of age, suggesting axonal loss (Fig. 9B). To investigate whether axons start to degenerate also in the PNS in the absence of demyelination, complete sciatic nerve cross sections were analyzed. Quantification of axon distribution revealed no significant differences between controls and *Cnp-Cre::Pex5^{flox/flox}* nerves at 2 months of age (Fig. 14A). Astonishingly, even severely impaired 9 months old mutants displayed normal distribution of axons (Fig. 14A). There was also no specific loss of small caliber ($\varnothing < 3 \mu\text{m}$) or big caliber ($\varnothing \geq 5 \mu\text{m}$) fibers (Fig. 14B). Although, aged

conditional mutants showed less large-caliber axons ($\varnothing \geq 5 \mu\text{m}$) than controls, this was highly variable between animals and not significant (Fig. 14C). Moreover, the overall number of axons was similar to that of controls in young and old mutant nerves (Fig. 14D). Taken together, these data suggest other nerve alterations, besides axonal degeneration, resulting in electrophysiological differences already at 2 months of age.

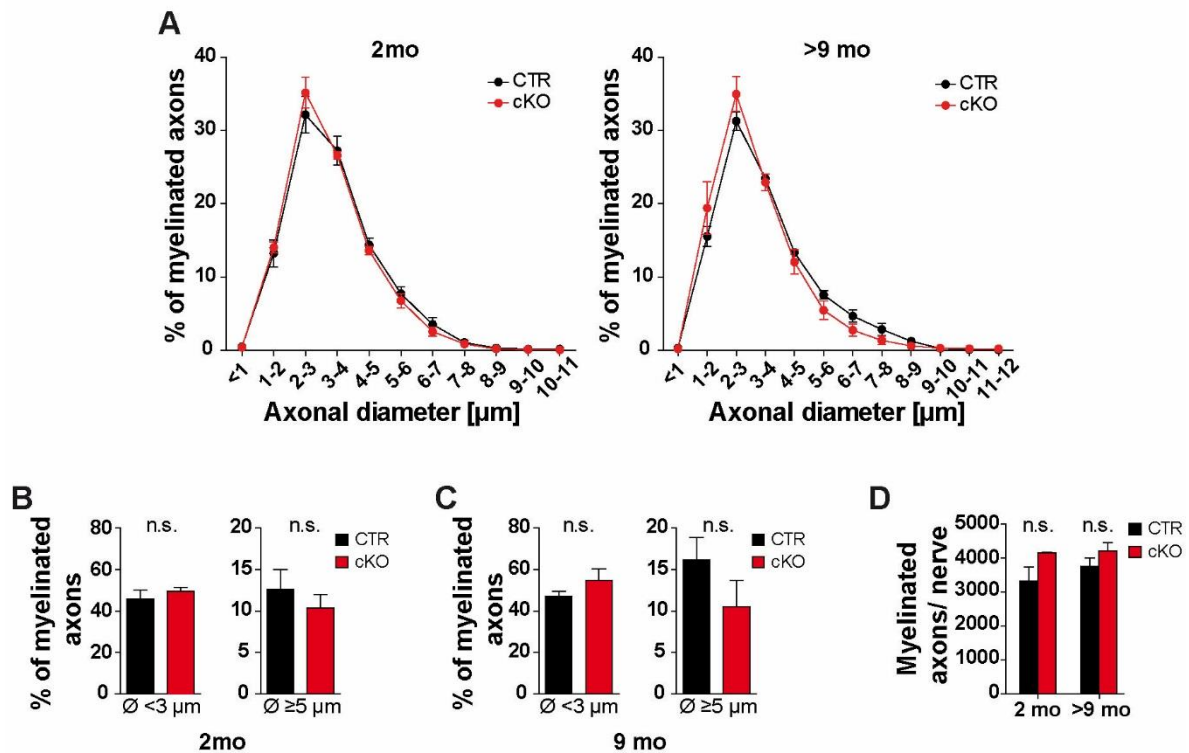


Fig. 14: Normal distribution and number of myelinated axons in *Cnp-Cre::Pex5^{flox/flox}* sciatic nerves

A) Analysis of axon distribution in complete cross sections of sciatic nerves from 2 months (left) or 9 months old (right) mice. Percentage of axons having a certain diameter is similar between controls (black) and mutants (red). (2 months, $n=4$ (CTR), $n=3$ (cKO); >9 months, $n=4$ per group; error bars: mean \pm s.e.m; Two-way ANOVA followed by Bonferroni test).

B-C) Percentage of small ($\varnothing < 3 \mu\text{m}$) and big ($\varnothing \geq 5 \mu\text{m}$) axons per nerve is comparable between 2 months or 9 months old conditional mutants and controls. (2 months, $n=4$ (CTR), $n=3$ (cKO); >9 months, $n=4$ per group; error bars: mean + s.e.m; n.s. not significant; Student's T-test).

D) Number of myelinated axons per nerve is comparable between controls and conditional mutants. (2 months, $n=4$ (CTR), $n=3$ (cKO); >9 months, $n=4$ per group; error bars: mean + s.e.m; n.s. not significant; Student's T-test).

2.3.3 Mild macrophage activation with occasional T-cells infiltration

Neuroinflammation is a frequent observation in neurodegenerative diseases (Amor et al., 2010). Furthermore, activated microglia and macrophages, as well as gliosis and T-cell infiltration, were early findings in the CNS of Cnp-Pex5-deficient mice (Kassmann et al., 2007). To detect neuroinflammatory processes, longitudinal paraffin-embedded sciatic nerve section of 2 and 9 months old mice were stained for MAC-3 and CD3 using DAB. MAC-3, a marker for macrophages, was moderately elevated in 2 and 9 months old conditional mutants (Fig. 15A). To get a more precise insight into the number of activated macrophages in sciatic nerves, semithin cross sections were stained for methylene blue/ azure II to visualize lipid-laden macrophages (Fig. 15B). These were rarely observed in nerves of young (2 months) conditional mutants, but about 3-fold elevated at 9 months (Fig. 15C). Invading T-cells were visualized by chromogenic staining for CD3 on longitudinal sections. CD3-positive cells were absent from 2 months old mutants and were occasionally found within nerves of 9 months old controls and mutants (Fig. 15E). In conclusion, we suggest only a minor impact of neuroinflammation especially at early stages of the pathology in mutant nerves.

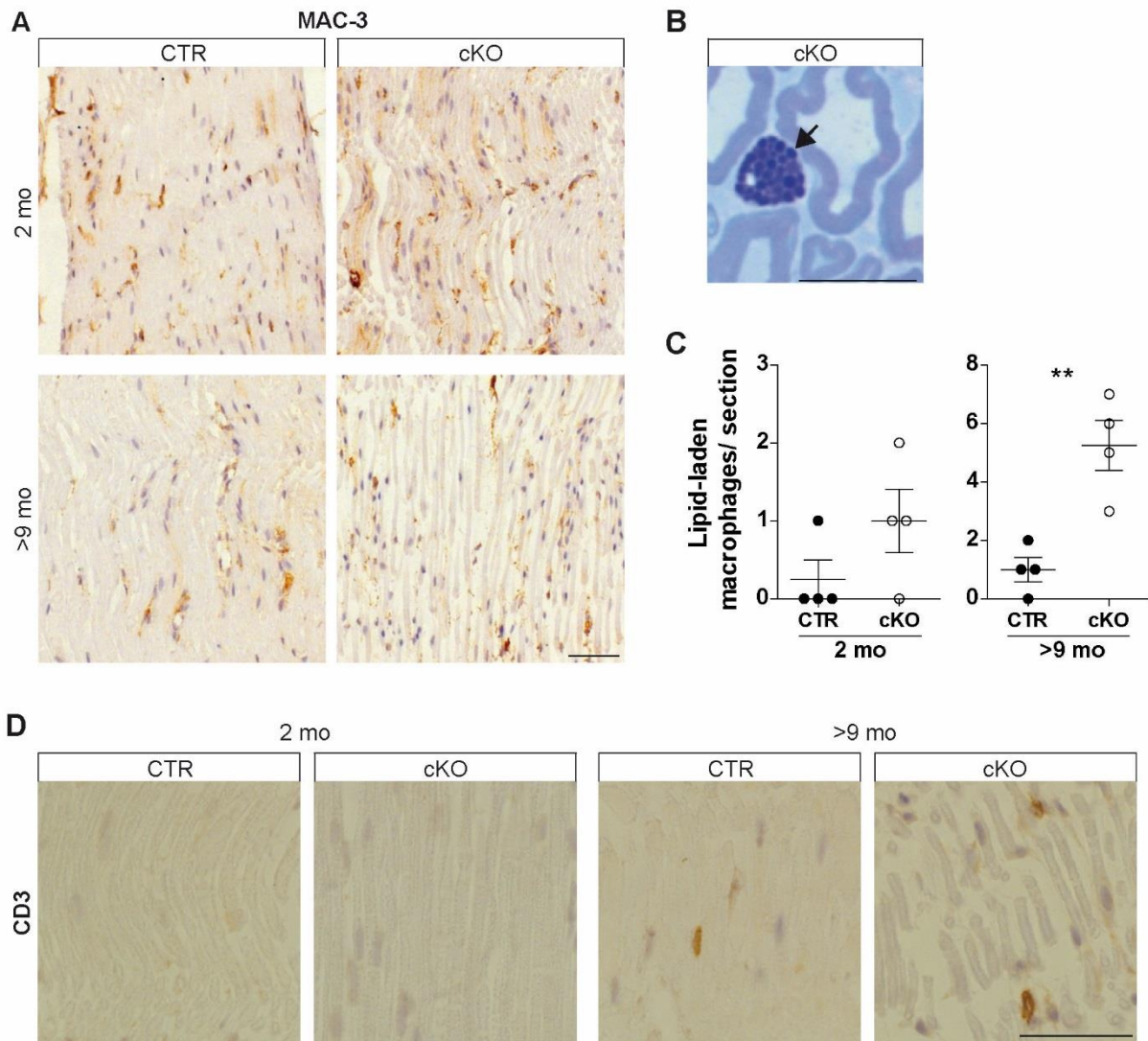


Fig. 15: Moderate neuroinflammation in *Cnp-Cre::Pex5^{flox/flox}* sciatic nerves

A) Chromogenic staining of longitudinal paraffin-embedded sciatic nerve sections from 2 and 9 months old mice shows slightly increased MAC-3 abundance in conditional mutants. Scale bar, 50 μ m.

B) Semithin cross section from 9 months old conditional mutant sciatic nerve, stained for methylene blue/ azure II, depicts a lipid-laden macrophage (arrow). Scale bar, 10 μ m.

C) Quantification of lipid-laden macrophages per nerve shows a minor increase of macrophages in 2 months old conditional mutant mice, which becomes significant in 9 months old conditional mutants. n=4 per group; error bars: mean + s.e.m; **p < 0.01; Student's T-test).

D) Chromogenic staining of longitudinal paraffin-embedded sciatic nerves sections from 2 and 9 months old mice occasionally shows CD3-positive cells, which were also observed in aged controls. Scale bar, 50 μ m.

2.4 Molecular composition of nodes of Ranvier

2.4.1 Normal formation of nodes and paranodal junctions

Neither myelin formation/compaction (Fig. 12 and 13), nor axon degeneration (Fig. 14) appeared to be a substantial feature of PNS pathology. Fast signal propagation is enabled by restriction of action potential generation to nodes of Ranvier. This is facilitated by high molecular and structural organization of myelinated axons through axo-glial interaction (Arroyo and Scherer, 2000; Salzer et al., 2008). Consequently, defects in this interplay especially at paranodes are a potential cause of impaired conduction due to leak currents (Arancibia-Carcamo and Attwell, 2014). Therefore, the integrity of paranodal junctions was investigated. Immunofluorescent teased fiber staining for axonal *contactin associated protein* (CASPR) and glial *neurofascin 155* (NF 155) showed clear colocalization of both proteins at paranodes (Fig. 16A). Also, ultrastructural analysis by electron microscopy revealed intact transverse bands, septate-like junctions between the axonal and adaxonal Schwann cell membrane (Fig. 16B). These were even observed at regions, where paranodal loops were enlarged due vesicular accumulations. Furthermore, contact sides between individual loops were intact, indicated by the presence of electron-dense autotypic junctions (Fig. 16C). To understand the occurrence of electrophysiological changes, the distribution of nodal ion channels was analyzed in sciatic nerve fibers from 2 and 9 months old mice. Immunohistochemistry of voltage-gated sodium ($\text{Nav}1.6$) and potassium ($\text{Kv}7.2$) channels showed normal localization at nodes, flanked by paranodal CASPR (Fig. 16D). This was evidenced by normal distribution of their axonal anchoring molecules *ankyrinG* (ANKG) and *β IV-spectrin* (Fig. 16E). These findings demonstrate intact axo-glial interaction at paranodes and excluded disturbed nodal sodium channels as a cause of diminished nerve responses.

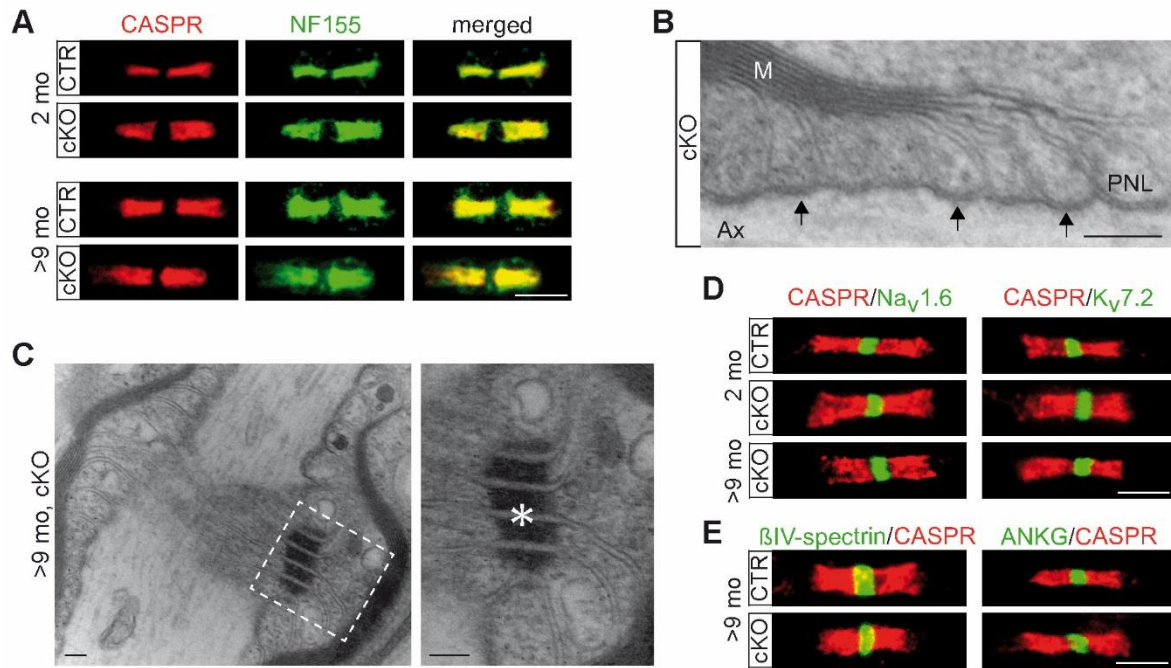


Fig. 16: Paranodal junctions are intact

A) Immunofluorescent staining of teased sciatic nerve fibers of 2 and 9 months old mice. Paranodal *contactin-associated protein* (CASPR, red) colocalized with its glial anchoring protein *neurofilament 155* (NF155, green) in controls and conditional mutants. Scale bar, 10 μm .

B) Electron microscopy demonstrates intact transverse bands (arrows), attaching the paranodal loops (PNL) of myelin (M) with the axon (Ax) of a mutant sciatic nerve aged 9 months. Scale bar, 500 nm.

C) Electron microscopy reveals intact autotypic junctions between individual paranodal loops (inset, asterisk), even when filled with vesicular accumulations. Scale bar, 500 nm.

D) Immunofluorescent teased fiber staining shows normal nodal sodium ($\text{Na}_v1.6$) and potassium ($\text{K}_v7.2$) channels (green) flanked by paranodal CASPR (red). Scale bar, 5 μm .

E) Axonal anchoring proteins of nodal ion channels are normally clustered in aged *Cnp-Cre::Pex5^{flx/flx}* nerves. Scale bar, 5 μm .

2.4.2 Ectopic localization of juxtapanodal Kv1.1 channels along internodes

Besides voltage-gated sodium and potassium channels, juxtapanodal Kv1.1 channels influence nerve excitability (Rasband and Shrager, 2000). Therefore, the distribution of these channels was investigated by immunofluorescent teased fibers staining of sciatic nerves from 2 and 9 months old mice. Interestingly, conditional mutant nerves showed already at 2 months of age additional, ectopic internodal Kv1.1 patches. When analyzing severely affected 9 months old nerves, this ectopic clustering was even more pronounced. Thus, aged animals showed considerably more Kv1.1 patches in the internode, which were also observed far from juxtapanodes (Fig. 17A). Nevertheless, normally localized Kv1.1 channels were still observed within the same fibers. However, these juxtapanodal clusters were shorter in most of the cases. These findings suggest a secondary problem in the maintenance of juxtapanodal Kv1 channels rather than disturbed initial formation. This was in line with preserved mesaxonal localization of Kv1.1 even in nerves with many ectopic clusters (Fig. 17B). To examine the progressive internodal shift of Kv1.1, its distribution was monitored at earlier time points during development (P19 and 1 months). This analysis demonstrated that already at P19, when Kv1.1 are just clustered at juxtapanodes, about 12% of nodes showed significant patches within internodes. Also, at 1 months of age, when myelination is completed, already 33% of nodes displayed internodal Kv1.1 clustering. This was progressive with age and affected almost 65% of nodes in 9 months old conditional mutants (Fig. 17C). Enhanced Kv1.1 protein abundance was proven by western blot analysis of sciatic nerve lysates from 9 months old mice, demonstrating a 2-fold increase of Kv1.1 protein amount in mutant nerves (Fig. 17D). In conclusion, these observations illustrate secondary problems of Kv1.1 maintenance at juxtapanodes due to disrupted peroxisomal function in Schwann cells, which suggests lipid metabolism-specific disturbances of axo-glia interaction.

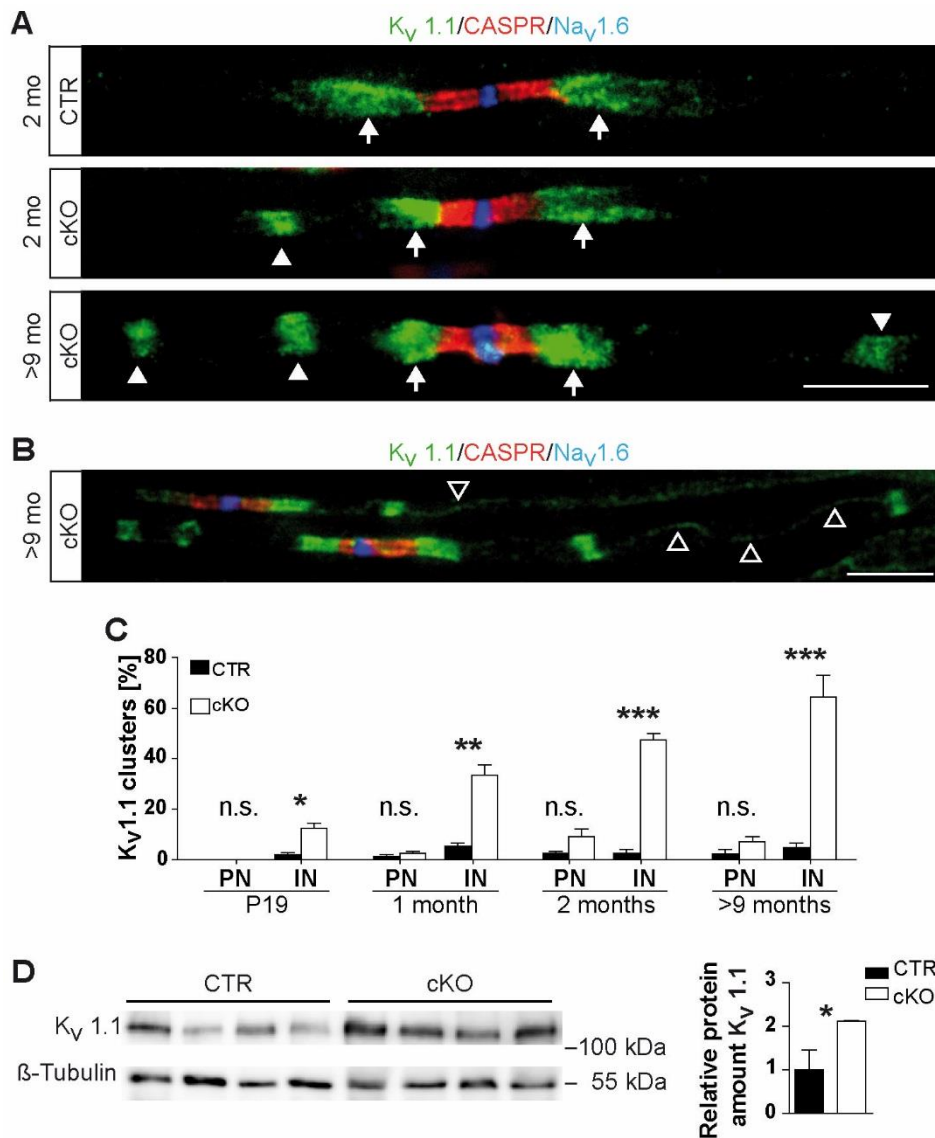


Fig. 17: Juxtaparanodal Kv1.1 proteins are progressively shifted towards internodes

A) Representative immunofluorescent images of teased fibers from 2 months and 9 months old mice stained for nodal Nav1.6 (blue), paranodal CASPR (red) and juxtaparanodal Kv1.1 (green). 2 months old conditional mutant nerves show, in addition to normal juxtaparanodal Kv1.1 channels (arrow), clusters within the internode (white arrow head). This ectopic internodal clustering is even pronounced in 9 months old animals (bottom panel). Scale bar, 10 μ m.

B) Immunofluorescent teased fiber staining for Nav1.6 (blue), CASPR (red) and Kv1.1 (green) shows preserved mesaxonal staining (non-filled arrow heads) of Kv1.1 even in severely affected nerves of 9 months old *Cnp-Cre::Pex5^{fllox/fllox}* animals. Scale bar, 10 μ m.

C) Percentage of Kv1.1 clusters in the paranode (PN) or internode (IN) at different ages. Quantification of Kv1.1 clusters highlights a progressive shift to internodes and not paranodes, starting at P19. (P19 and 1 months, n=3, ~ 100 nodes counted per animal; 2 months, n=5, ~ 40 nodes counted per animal; >9 months, n=7, ~ 30 nodes counted per animal; error bars: mean + s.e.m; *p < 0.05, **p < 0.01, ***p < 0.001; Student's T-test).

D) Western blot analysis indicates a 2-fold increase of total Kv1.1 protein amount in nerve lysates from 9 months old mutants. Beta-III tubulin was used as loading control. (n=4 per genotype, error bars: mean + s.e.m, *p < 0.05, Student's T-test).

2.4.3 Impaired anchoring of Kv1.1 channels

Kv1.1 anchoring and maintenance at juxtaparanodes depend on the axonal adhesion molecules CASPR2 and TAG-1. Disruption of either protein causes redistribution of K⁺ channels evenly along internodes (Poliak and Peles, 2003). Co-staining of paranodal CASPR with either CASPR2 or TAG-1 revealed a shift of both proteins into the internode already at 2 months of age. Similar to Kv1.1 channels, both anchoring proteins progressively showed extra clusters within internodes, additional to their normal juxtaparanodal position (Fig. 18A, B). Co-labeling of Kv1.1 with either CASPR2 (Fig. 18C) or TAG-1 (Fig. 18D) showed clear colocalization with Kv1.1, suggesting a shift of the entire juxtaparanodal complex into the internode. This was further verified by quantifying internodally located Kv1.1 that colocalized with TAG-1, demonstrating that the two proteins colocalized on 97% of ectopic patches (Fig. E). These results suggest impaired maintenance of juxtaparanodal proteins possibly due to defects in axo-glial interaction at these sites.

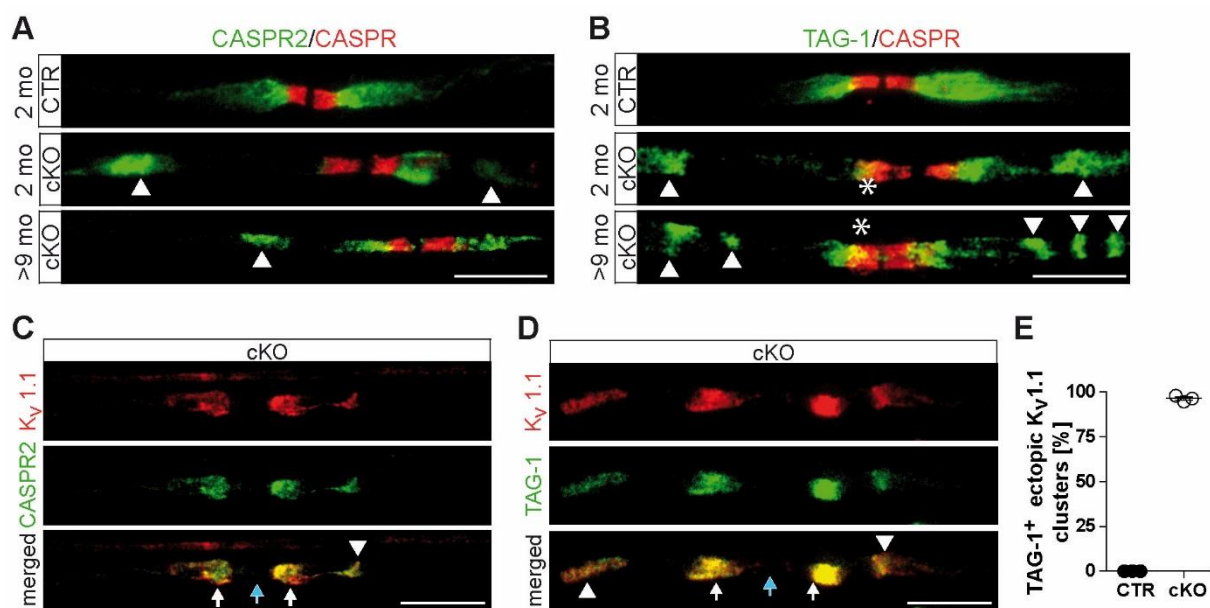


Fig. 18: The entire juxtaparanodal complex drifts into internodes

A-B) Representative immunofluorescent images of teased sciatic fibers, stained for paranodal CASPR (red) and juxtaparanodal CASPR2 or TAG-1 (green) reveals progressive internodal clustering of CASPR2 and TAG-1 (arrow head) in conditional mutants. TAG-1 occasionally shifts into paranodes (asterisk). Scale bar, 10 μ m.

C-D) Teased fiber staining of 9 months old conditional mutant nerves reveals clear colocalization of CASPR2 and TAG-1 (green) with normal juxtaparanodal (white arrow) or ectopic internodal (arrow head) Kv1.1 (red) clusters. Nodes are indicated by blue arrows. Scale bars, 10 μ m.

E) Quantification of ectopic Kv1.1 patches that colocalize with TAG-1. (~100 patches per animal were counted; error bars: mean + s.e.m).

2.5 Perturbation of gangliosides

Gangliosides are abundant glycosphingolipids that stabilize the molecular composition of nodes and are associated with TAG-1 (Sheikh et al., 1999; Kasahara et al., 2000; Loberto et al., 2003). Moreover, they contain increased amounts of VLCFA in white matter regions of brains from X-ALD patients (Igarashi et al., 1976b). Lipid mass spectrometry was performed on sciatic nerve lysates from 9 months old mice to investigate the composition of gangliosides. This analysis clearly showed increased proportion of GD1 species that were bound to VLCFA in nerves obtained from *Cnp-Cre::Pex5^{flox/flox}* mice. Altogether, there was a 14-fold enrichment of GD1 species with more than 41 carbon atoms (Fig. 19A). Given the fact, that the sphingosine chain of mammalian brain gangliosides primarily contains 18 carbons and is bound to a saturated fatty acid (C18:0; Schnaar et al., 2014), there is a significant increase in GD1 species bound to VLCFA (C23:0; C25:0; C26:0; C26:1). Moreover, only 0.74% of GD1 species in control lysates contained 41 C-atoms (C23:0) and species with more than 41 C-atoms were even absent (Fig. 19A).

To further analyze whether this difference in ganglioside composition has an impact on subcellular distribution of gangliosides, teased fibers of 9 months old nerves were stained, using ganglioside-specific antibodies. In addition, specific binding of the B-subunit of cholera toxin (CTB) to GM1 gangliosides was used to visualize GM1-distribution within sciatic nerve fibers (Holmgren et al., 1975; Jobling et al., 2012). Co-staining with an axonal marker (TUJ1) revealed CTB localization predominantly in close proximity to nodes of Ranvier. Thus, in control nerves the paranodal region was labeled by CTB. Mutant nerves interestingly demonstrated a more extended paranodal pattern (Fig. 19B). Similar differences at paranodes were observed with a GM1-specific antibody. Here, GM1 distribution at paranodes was even more distended towards internodes (Fig. 19C). Moreover, GM1 seemed to be more axonal compared to controls. GD1a another ganglioside that is produced from GM1 (Tettamanti et al., 1973) also presented altered subcellular distribution at nodes. Control nerves showed specific paranodal staining, which was in mutant nerves more disperse and spread towards internodes (Fig. 19D). Since gangliosides are a typical substrate of lysosomes, co-labeling was performed with LAMP1. Astonishingly, conditional mutant nerves displayed massively enlarged GD1a-positive accumulates, which were associated with LAMP1. These accumulations were especially found within internodes and were only

rarely observed in control nerves (Fig. 19E, F). In conclusion, ganglioside metabolism is perturbed in these mice due to deficient peroxisomal β -oxidation. Additionally, ganglioside distribution is altered most probably due to their enrichment in VLCFA. Finally, GD1a/LAMP1 staining suggests a secondary halt of ganglioside degradation within lysosomes.

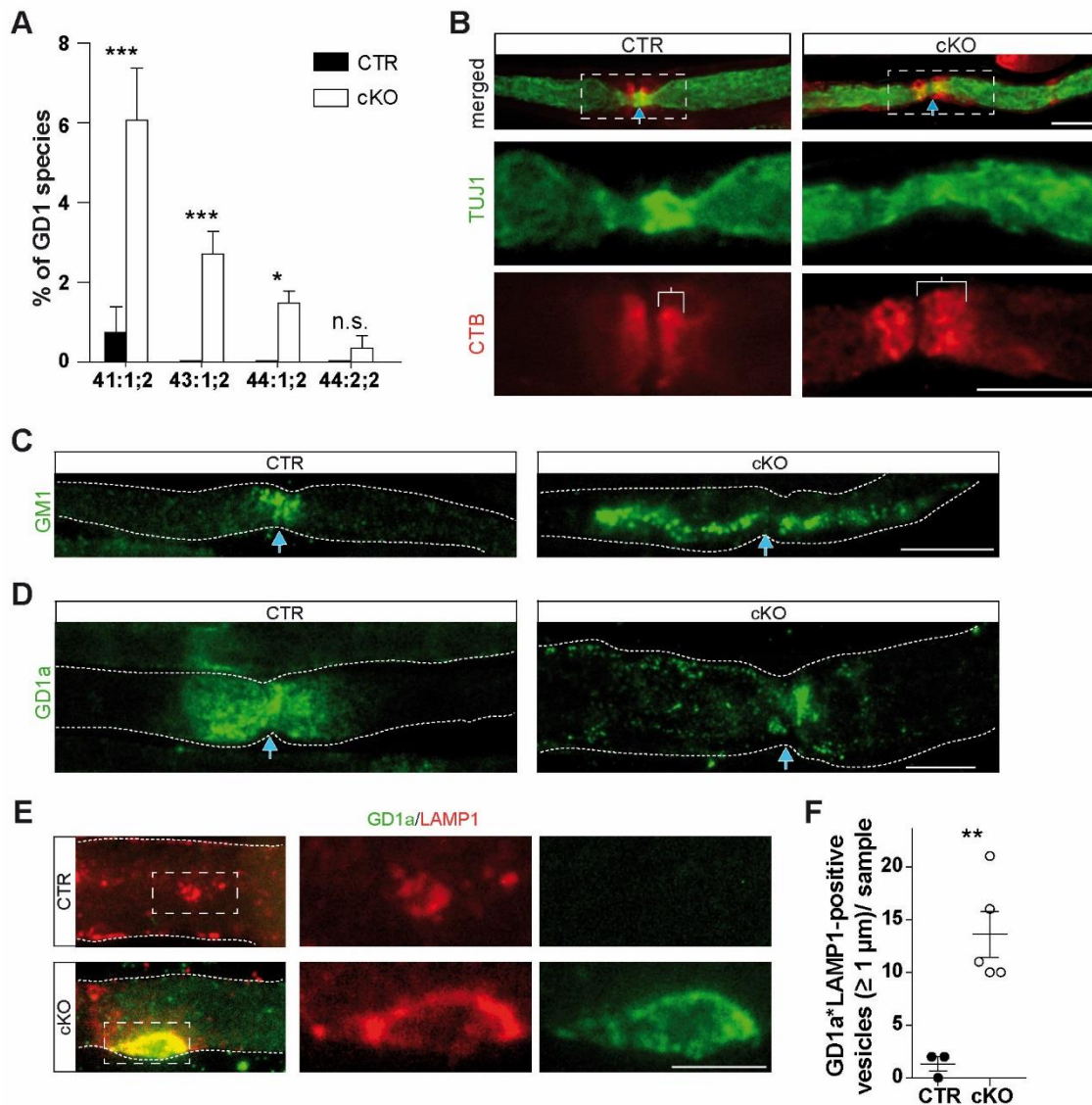


Fig. 19: Ganglioside metabolism and their distribution at nodes of Ranvier is disturbed

A) Mass spectrometry of sciatic nerve lysates from 9 months old mice reveals significantly increased percentage of GD1 species containing 41, 43, or 44 C-atoms (number of double bonds is separated by “:” and number of hydroxyl groups is separated with “;”). GD1 species with more than 41 C-atoms are absent in control nerve lysates. (n=4 per genotype, error bars: mean + s.e.m; *p < 0.05, ***p < 0.001; Student’s T-test).

B) Teased fiber staining of fluorescently labeled cholera-toxin subunit B (CTB, red) and axonal TUJ1 (green) reveals an extended paranodal CTB pattern in 9 months old mutant nerves. Blue arrow indicates nodes of Ranvier. Scale bar, 10 μm .

C) Control nerves show GM1 staining close to nodes of Ranvier (blue arrow), whereas in mutant nerves GM1 is increased and expands towards internodes. Dotted lines indicate myelinated fiber border. Scale bar, 10 μm .

D) Paranodal staining of GD1a is more disperse and internodally diffused in mutant nerves. Dotted lines indicate myelinated fiber border. Scale bar, 10 μm .

E) Co-labeling of GD1a (green) with LAMP1 (red) shows enlarged GD1a accumulates within internodes of mutant nerves that were also positive for LAMP1 (insets) and were very rarely observed in controls. Scale bars, 5 μm .

F) Number of GDa1-positive vesicles (bigger than 1 μm) that colocalize with LAMP1 was significantly elevated in nerves from 9 months old *Cnp-Cre::Pex5^{fllox/fllox}* mice. (~ 10% of total nerve material was analyzed, n=3, CTR; n=5, cKO; error bars: mean + s.e.m; **p < 0.01; Student’s T-test).

2.6 Secondary alterations of the endosomal-lysosomal system

2.6.1 Lysosomes are in close contact with peroxisomes

Recently, it has been shown that peroxisomes and lysosomes establish dynamic membrane contacts *in vitro*, through which cholesterol is transported from lysosomes to peroxisomes (Chu et al., 2015). According to this observation, the question arose if peroxisomes and lysosomes are also associated *in vivo*. Peroxisomes have been shown to be abundant in myelin rather than axons (Kassmann et al., 2011). To investigate whether lysosomes and peroxisomes are found in the same cellular compartments, which would at least afford spatial proximity, teased fiber preparations were stained for *neurofilament 200* (NF200) and either *peroxisomal membrane protein 70* (PMP70) or *lysosome-associated membrane protein 1* (LAMP1). Indeed, PMP70 was highly abundant at SC nuclei and never colocalized with NF200, indicating myelin association (Fig. 20A, upper panel). Similar observations were made for LAMP1, which was particularly abundant at nodes and was also never observed within the axonal compartment (Fig. 20A, lower panel). Furthermore, co-labeling of PMP70 and LAMP1 demonstrated close association of both organelles in the myelin compartment, which was most prominent at SC nuclei and nodes of Ranvier. Ring-like LAMP1-positive structures were observed at paranodes that were surrounded by PMP70-positive vesicles (Fig. 20B). These results strongly suggest *in vivo* interaction of peroxisomes and lysosomes.

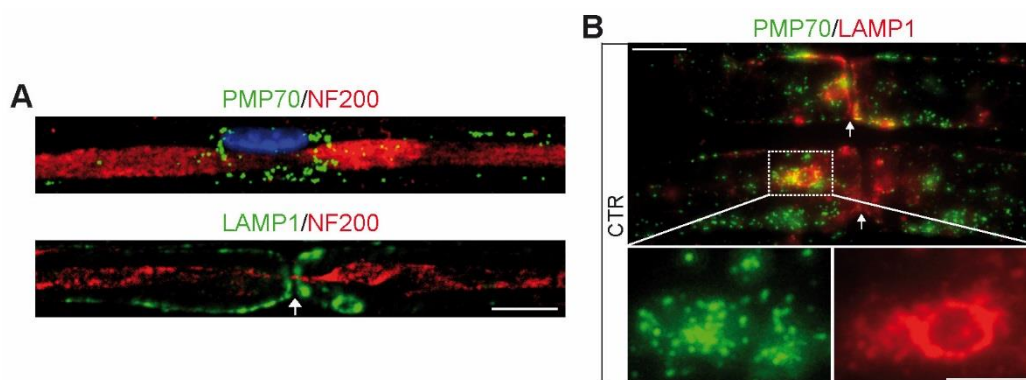


Fig. 20: Peroxisomes and lysosomes are closely associated in the paranodal Schwann cell compartment

A) Immunofluorescent teased fiber staining for NF200 (red) and either PMP70 or LAMP1 (green) indicates association of both organelles with SC rather than axons. SC nuclei are stained with DAPI (blue). Arrow indicates the node. Scale bar, 10 μm .

B) Peroxisomes (PMP70, green) and lysosomes (LAMP1, red) are highly abundant near nodes and show close association in 9 months old control sciatic nerves. Arrows indicate nodes. Scale bars, 10 μm .

2.6.2 Accumulation of lysosomes at paranodes

Ganglioside metabolism is disturbed in *Cnp-Cre::Pex5^{flox/flox}* mice due to deficient peroxisomal β -oxidation. As a consequence, these lipids are enriched at nodes and also within internodes (Fig. 19B-E). Interestingly, enlarged GD1a-positive vesicles colocalized with LAMP1 within internodes (Fig. 19E). Peripheral nerves of conditional mutants display paranodal swellings filled with vesicular inclusions and multivesicular bodies of so far unknown origin (Kassmann et al., 2011). In addition, we found peroxisomes and lysosomes closely associated at nodes of Ranvier (Fig. 20B). Thus, the question arose, if peroxisomal defects could provoke secondary problems in the lysosomal compartment, resulting in paranodal accumulations. To test whether paranodal vesicles are of lysosomal origin, immuno-electron microscopy and teased fiber staining for LAMP1 were performed. Indeed, electron microscopy of immunogold labeled ultrathin cryo sections identified LAMP1-positive vesicles within enlarged paranodal loops of 9 months old mutant nerves (Fig. 21A). Furthermore, immunofluorescent staining of teased fibers for LAMP1 (Fig. 21B) and *lysosome-integrated membrane protein 2* (LIMP2, Fig. 21C) evidenced abundant lysosome-associated vesicles around nodes. These vesicles appeared extremely enlarged in mutant nerves already at 2 months of age. In addition to paranodes, indicated by CASPR staining, lysosome-associated vesicles were also observed in more juxtaparanodal or even internodal regions (Fig. 21B-C). These findings suggest a secondary problem of the endosomal-lysosomal pathway within the Schwann cell compartment due to peroxisomal dysfunction.

Since the endosomal-lysosomal system is highly dynamic, it is difficult to clearly differentiate between primary lysosomes and late endosomes. Thus, LAMP1 is also expressed by late endosomes and autolysosomes (Clague, 1998; Huotari and Helenius, 2011). To validate the origin of paranodally accumulated vesicles, other components of the endosomal-lysosomal pathway were examined. Teased fiber staining of 9 months old nerves for *Ras-related protein 7* (RAB7), a marker protein of late endosomes, and *early endosome antigen 1* (EEA1) showed no increase of either protein at paranodes (Fig. 22A, B). Similar results were obtained for *autophagy protein 5* (ATG5), a marker for autophagy. Quantitative real-time PCR for *MAP1LC3A*, which is important in autophagosome formation, highlighted significantly less mRNA abundance in aged, but not young mutant nerves (Fig. 22D).

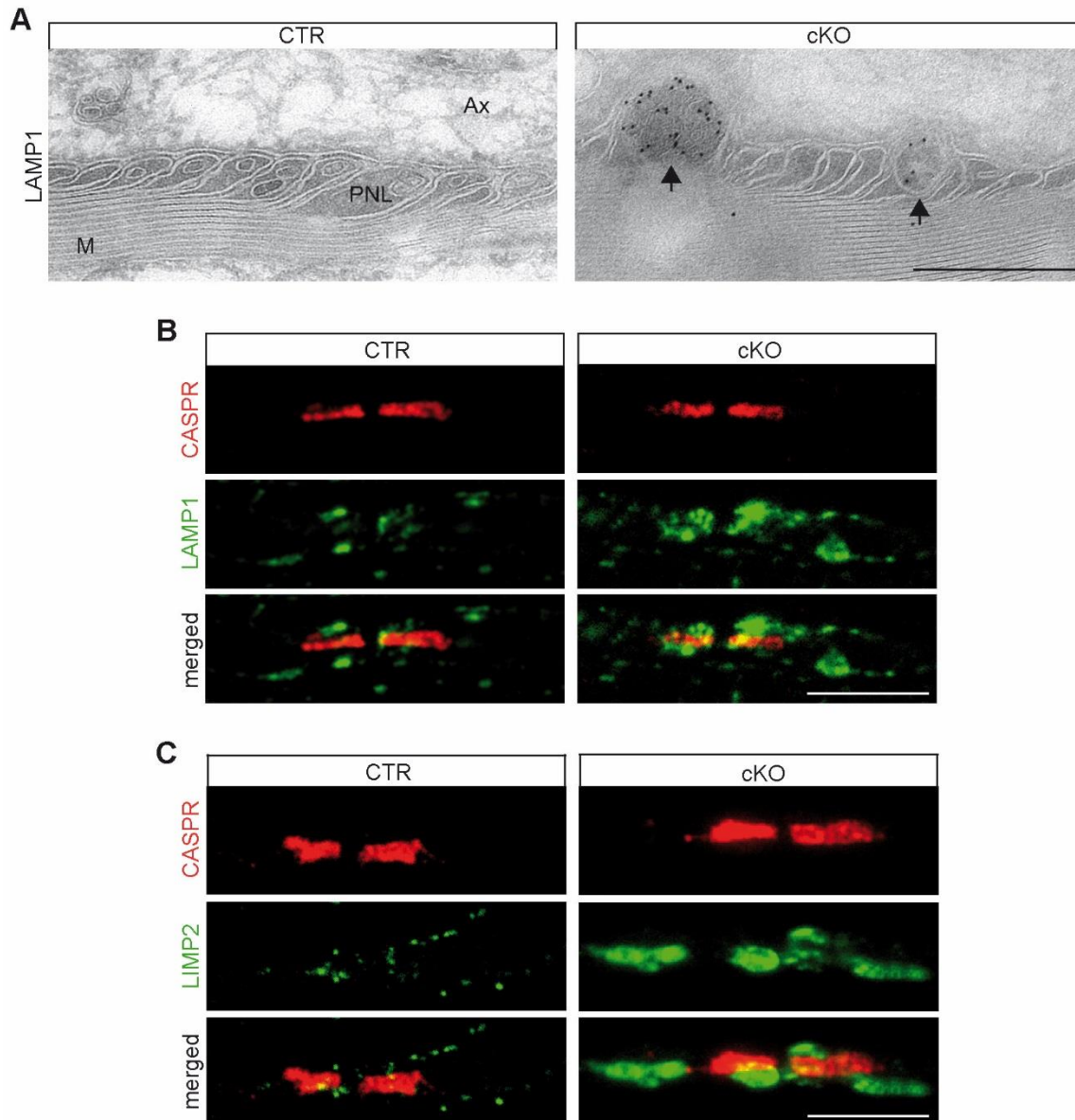


Fig. 21: Accumulation of enlarged lysosome-associated vesicles at paranodes

A) Immunogold labeling of ultrathin longitudinal sciatic nerve sections from 9 months old mice depicts enlarged paranodal loops (PNL) filled with LAMP1-positive vesicles (arrows) in conditional mutants. M, myelin; Ax, axon. Scale bar, 500 nm.

B-C) Immunofluorescent images of teased sciatic nerves from 2 months old mice show abundant and enlarged LAMP1- and LIMP2-positive vesicles (green) near paranodes (CASPR, red) of mutant nerves. Scale bars, 10 μ m.

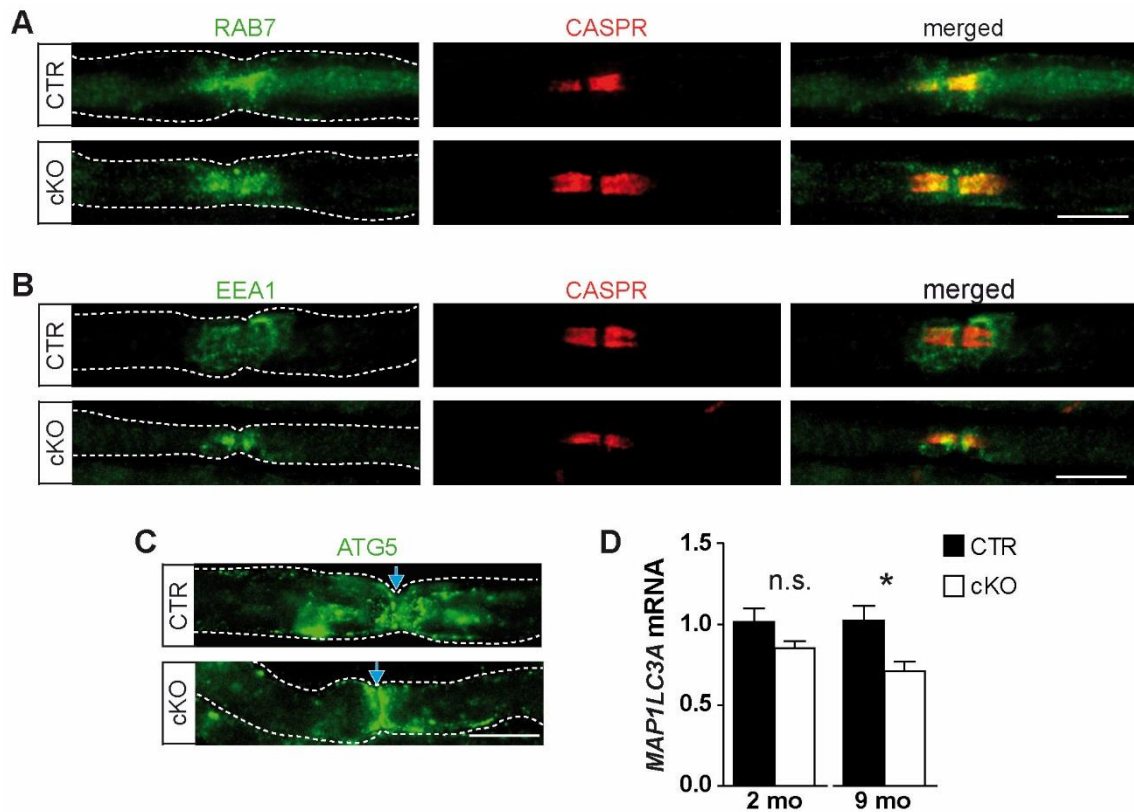


Fig. 22: Endosomal and autophagic vesicles are not accumulating at nodes of *Cnp-Cre::Pex5^{flox/flox}* nerves

A, B Immunofluorescent staining of late (RAB7, green) and early (EEA1, green) endosomes at nodes of Ranvier (CASPR, red). Scale bar, 10 μ m.

C Immunofluorescent staining of *autophagy protein 5* (ATG5, green) at nodes of Ranvier (blue arrow). Scale bar, 10 μ m.

D Quantitative real-time PCR demonstrates significantly less mRNA expression of *MAP1LC3A* in sciatic nerve lysates from 9 months old *Cnp-Cre::Pex5^{flox/flox}* mice. (n=6 per genotype; error bars: mean + s.e.m; n.s., not significant; *p < 0.05; Student's T-test).

2.6.3 Accumulation of lysosomes within enlarged Schmidt-Lanterman incisures

Like paranodal loops, Schmidt-Lanterman incisures are a region of non-compact myelin that is involved in axo-glia interaction and metabolic exchange (Hall and Williams, 1970; Nave, 2010b). Considering paranodal accumulation of LAMP1, lysosomal abundance within SLI was investigated. LAMP1-positive vesicles were found within SLI (indicated by MAG co-staining) of control nerves and were massively elevated in *Cnp-Cre::Pex5^{flox/flox}* nerves (Fig. 23A). Immunogold labeling of nerve sections from 9 months-aged mutants revealed abnormally enlarged SLI, which were filled with multivesicular bodies positive for LAMP1 (Fig. 23B). Immunofluorescent staining of MAG and 4.1G revealed a dramatically increased number of SLI in 9 months old conditional mutants. Thus, SLI were closely assembled and often spaced by only a few micrometer (Fig. 23C). Quantification of MAG-positive patches per 100 μm nerve length highlighted a 1.5-fold increase of SLI in 2 months old mutants and even a 3-fold increase of SLI in 9 months old mutants (Fig. 23D). Thus, the number of SLI increased progressively with age in *Cnp-Cre::Pex5^{flox/flox}* mice. Moreover and as expected from the literature, this was even most prominent in large fibers. Assuming a role for SLI in SC-axon communication these observations suggest a compensatory mechanism of disturbed interaction.

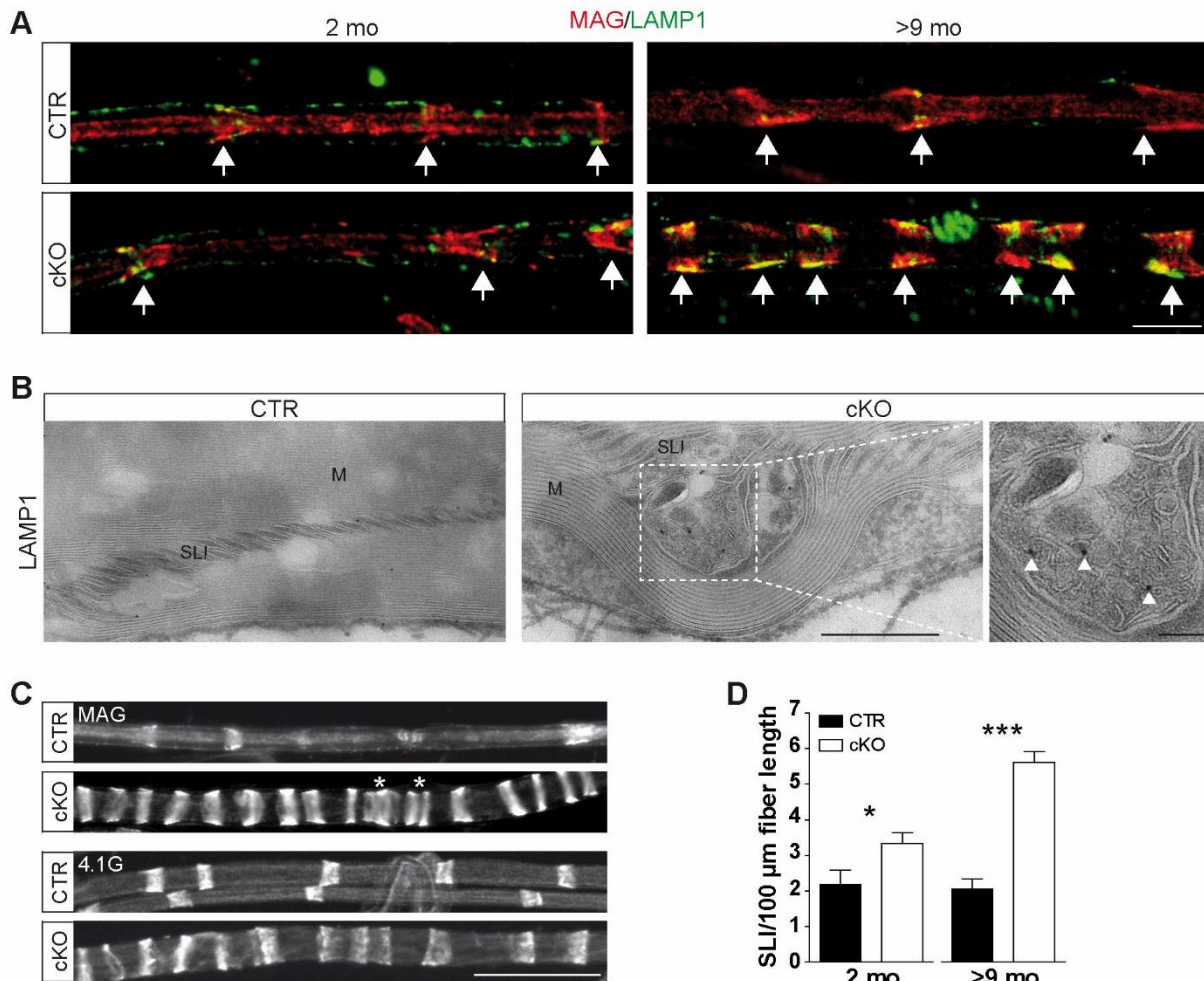


Fig. 23: Schmidt-Lanterman incisures are increased in number and contain LAMP1-positive vesicles

A) Immunofluorescent teased fiber staining for myelin-associated glycoprotein (MAG) and LAMP1 in 2 and 9 months old sciatic nerves. Funnel-shaped Schmidt-Lanterman incisures (MAG, red) contain LAMP1-positive vesicles (green), both in controls and conditional mutants (arrows). The number of SLI, as well the abundance of LAMP1 vesicles is progressively increased in conditional mutants. Scale bar, 10 μm.

B) Immunogold labeling of ultrathin longitudinal sciatic nerve sections from 9 months old mice shows Schmidt-Lanterman incisures (SLI) that contain multivesicular bodies, positive for LAMP1 (inset, arrow heads), in conditional mutants. M, myelin. Scale bars, 500 nm.

C) Immunofluorescent staining for MAG and 4.1G reveals a massive increase of SLI in 9 months old conditional mutants. Some SLI were closely assembled into rows, which were considered as one SLI for quantitative analysis (asterisk). Scale bar, 50 μm.

D) Quantification of SLI per 100 μm fiber length demonstrates increased number of SLI already at 2 months of age, which is further enhanced in 9 months old conditional mutants. (2 months, n=4; > 9 months, n=5; error bars: mean + s.e.m; *p < 0.05, ***p < 0.001; Student's T-test).

Next, lysosomal accumulation was investigated by western blot analysis of total sciatic nerve lysates from 9 months old mice, confirming excessive LAMP1 and LIMP2 protein abundance in mutant nerves (Fig. 24A). Quantitative analysis revealed a 4-fold increase of LAMP1 protein amount and a 2-fold elevated LIMP2 protein abundances in conditional mutants (Fig. 24B). To investigate whether elevated LAMP1 and LIMP2 protein amounts are related to higher mRNA expression, quantitative real-time PCR was applied. Interestingly, relative mRNA expression of LAMP1 and LIMP2 were significantly reduced in 2 months old mutant nerves. Moreover, LAMP1 showed significantly mRNA reduction even in 9 months old mutants (Fig. 24C). These results point to a secondary accumulation rather than enhanced biogenesis due to peroxisomal dysfunction.

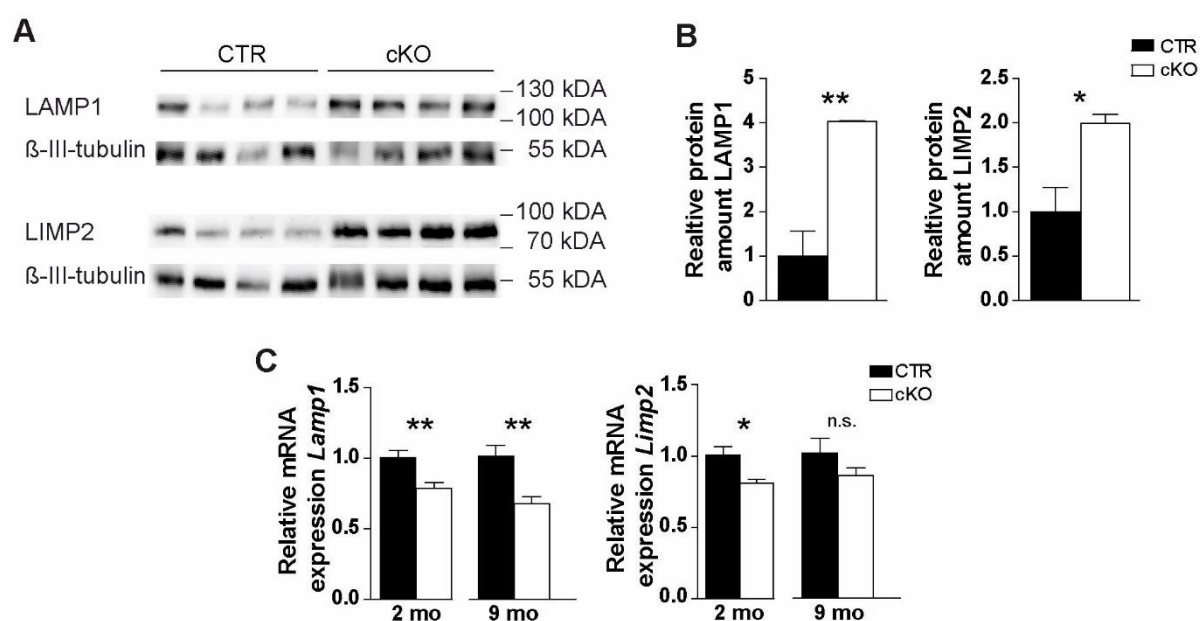


Fig. 24: Relative protein abundance and mRNA expression of LAMP1 and LIMP2

A) Western blot analysis of sciatic nerve lysates from 9 months old mice showing results from 4 individual animals per genotype. β-III-tubulin was used as loading control.

B) LAMP1 shows about 4-fold increased relative protein amount in conditional mutants. Relative LIMP2 protein amount is 2-fold elevated in mutants. (n=4 per genotype; error bars: mean + s.e.m; *p < 0.05, **p < 0.01; Student's T-test).

C) Quantitative real-time PCR reveals significantly reduced relative mRNA expression of *Lamp1* and *Limp2* in 2 months and for *Limp1* also in 9 months old mutant nerves. Values are represented as relative amounts of control results, which were set to one. (n=6 per genotype; error bars: mean + s.e.m; *p < 0.05, **p < 0.01; Student's T-test).

2.6.4 Alterations of lysosomal function

Lysosomal accumulation is a common feature of lysosomal storage disorders that mostly result from enzyme deficiencies (Jeyakumar et al., 2005; Braulke and Bonifacio 2009). Lysosomes contain a set of hydrolases to digest macromolecules. To study whether abundant lysosomes are still functional, the enzymatic activity of α -mannosidase and β -hexosaminidase was measured in sciatic nerve lysates from 2 and 9 months old mice. Both enzymes showed an elevated activity already in 2 months old mutant nerves. The increase in the enzymatic activity was further progressive with age and reached about 3-fold of control values in *Cnp-Cre::Pex5^{flox/flox}* mice aged 9 months (Fig. 25A-B). Most interestingly, β -hexosaminidase is essential for digestion of GM2 gangliosides (Sandhoff and Harzer, 2013), suspecting a direct link between disturbed ganglioside metabolism and elevated enzymatic activity.

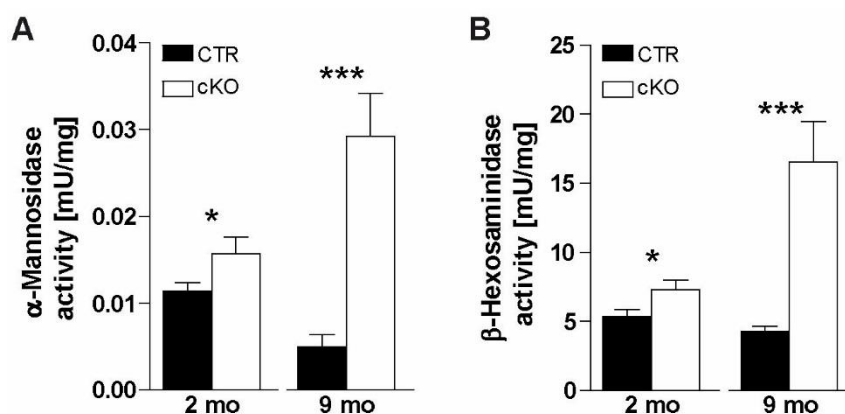


Fig. 25: Lysosomal enzyme activity is progressively enhanced in *Cnp-Cre::Pex5^{flox/flox}* nerves

A-B) Enzyme activity assay of sciatic nerves lysates from 2 and 9 months old mice reveals progressive elevation of α -mannosidase and β -hexosaminidase activity in *Cnp-Cre::Pex5^{flox/flox}* nerves, reaching a 3-fold increase in 9 months old mutants. (n=4; error bars: mean + s.e.m; *p < 0.05, ***p < 0.001; Student's T-test).

2.7 Comparative analysis of ABCD1-deficient mice, a model of human adrenomyeloneuropathy

To test whether the observed nerve pathology of conditional *Pex5* mutants is also relevant for other peroxisomal mouse models of disease, a comparative analysis of *Abcd1*^{-/-} mice, a model of X-linked adrenoleukodystrophy (X-ALD), was performed. These mice lack the peroxisomal ABCD1 transporter, which is required for import of very long-chain fatty acids into peroxisomes for subsequent degradation (van Roermund et al., 2008; Wiesinger et al., 2013). ABCD1-deficiency results in disturbed peroxisomal β -oxidation (Wanders, 2004a). Although, these mice lack cerebral symptoms, typical for the severe form of the disease (cerebral ALD), they develop a late-onset peripheral neuropathy, mimicking symptoms of the adult-onset form of the same disease, adrenomyeloneuropathy (AMN; (Forss-Petter et al., 1997; Lu et al., 1997; Pujol et al., 2002).

2.7.1 Behavioral analysis of nerve impairment in ABCD1-deficient mice

First electrophysiological and myelin alterations of sciatic nerves were observed in *Abcd1*^{-/-} mice between 15 and 16 months of age and the earliest motor impairment was recorded at 20 months of age, using the rotarod test (Pujol et al., 2002). Therefore, the aim was to find a more sensitive behavioral test, allowing earlier detection of possible motor defects. To this end, motor performance was assessed at three different time points: at 13 months of age, before detection of electrophysiological alterations; at 15 months, when neuropathy is obvious by electrophysiology; and at 18 months of age, just before behavior deficits became apparent by rotarod. The grid test was used to evaluate motor coordination (Fig. 26A). Mice had to run 1.5 m on a metal grid while their front and hind paw slips were counted. *Abcd1*^{-/-} mice tended to slip more frequently already at 13 months of age, which was more pronounced at front paws, but these differences were not significant. Although the same trend was observed at 15 months of age, there was no further increase in the number of slips. Only at 18 months of age, the mean number of slips had slightly risen. However, this was also observed in age-matched controls, indicating rather an aging than a genotype effect (Fig. 26A). Next, fore limb muscles strength was evaluated by the grip strength test. This test also failed to show significant differences between controls and *Abcd1*^{-/-} mice at 13 and 15

months of age, but revealed age-dependent muscle weakness (Fig. 26B). Finally, the elevated beam test was used to assess motor coordination and balance. Mice had to reach a box by walking an elevated beam. The number of slips, as well as the time animals needed to reach the box, were comparable between controls and *Abcd1*^{-/-} mice at 13 months of age. As expected, the walking speed was reduced in 15 months old animals of both genotypes. Thus, *Abcd1*^{-/-} mice were as fast as controls, showing slightly, however not significantly, more slips (Fig. 26C). Taken together, none of the tests was challenging enough to show more subtle motor deficits. Moreover, high variances between individual animals possibly disguised genotype-specific differences, but highlighted aging effects.

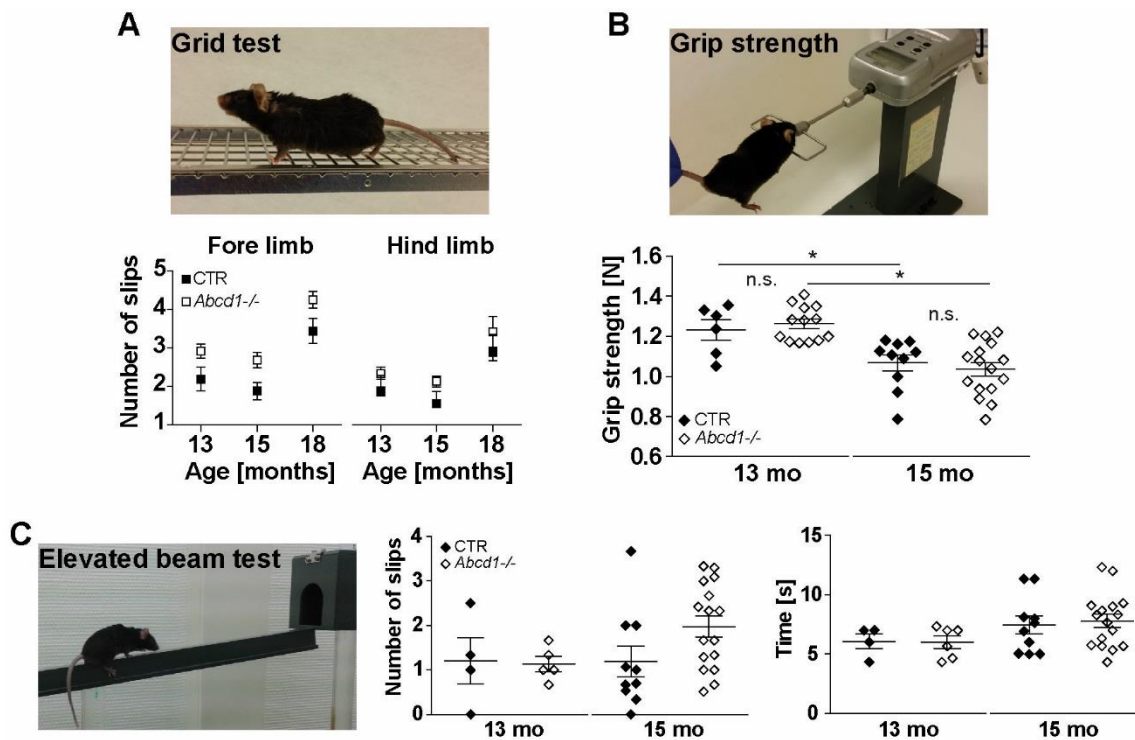


Fig. 26: Behavioral assessment of motor performance

A) Mouse performing on the grid (size of grid 1 x 1 cm). There is no significant difference between genotypes at any tested time point. There is an age-dependent, non-significant increase of slips at 18 months of age within both groups. (13 months, n=9 (CTR), n=20 (*Abcd1*^{-/-}); 15 months, n=13 (CTR), n=23 (*Abcd1*^{-/-}); 18 months, n= 7 (CTR), n=8 (*Abcd1*^{-/-}); error bars: mean \pm s.e.m; Student's T-test).

B) A mouse is gently pulled at the tale, while grasping the bar of the grip strengths device. The grasping force is comparable between controls and *Abcd1*^{-/-} mice at 13 and 15 months of age, but shows a significant age-dependent decline of grip strength (right graph). (13 months, n=5 (CTR), n=13 (*Abcd1*^{-/-}); 15 months, n=10 (CTR), n=16 (*Abcd1*^{-/-}); error bars: mean + s.e.m, n.s. not significant, *p < 0.05; Student's T-test).

C) Mouse performing on the elevated beam. *Abcd1*^{-/-} mice tend to make more hind limb slips than controls at the age of 15 months (left graph). *Abcd1*^{-/-} mice are slower reaching in the house (right graph). At 13 months of age, *Abcd1*^{-/-} performed similar to controls (13 months, n=4 (CTR), n=5-6 (*Abcd1*^{-/-}); 15 months, n=10 (CTR), n=16 (*Abcd1*^{-/-}); error bars: mean \pm s.e.m; n.s.; Student's T-test).

It has been shown that ABCD1-deficient mice develop reduced sensitive nerve conduction velocities at 20 months of age (Pujol et al., 2002). Furthermore, sensory impairment is a common feature of especially AMN patients (Moser et al., 2007). To associate published electrophysiological alterations with behavioral deficits, pressure and heat sensation was assessed in 13, 15 and 18 months old *Abcd1*^{-/-} mice and compared to corresponding controls. Here, *Abcd1*^{-/-} mice revealed slightly reduced reactions in response to mechanical stimuli at 13 months of age, which was however not significant. Moreover, at later time points (15 and 18 months of age) there was no distinct difference between controls and mutants (Fig. 27A). The same was true for

thermal stimuli. Although the latency was slightly increased at older ages (15 and 18 mo), this was not significant and showed again high variances within groups (Fig. 27B). In summary, neither the dynamic plantar aesthesiometer test (pressure sensation) nor the plantar Hargreaves test (heat sensation) reflected sensory deficits.

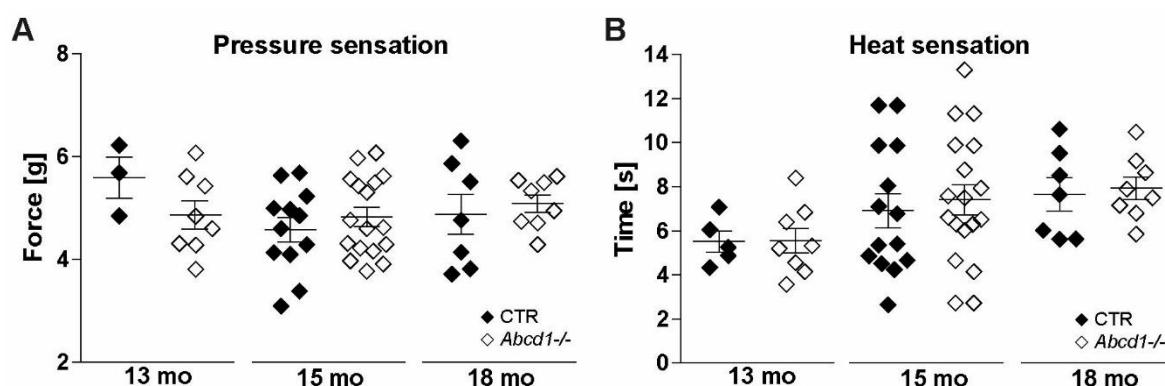


Fig. 27: Normal pressure and heat sensation in aged *Abcd1*^{-/-} mice

A) Behavioral assessment of pressure sensation, using the dynamic plantar aesthesiometer, reveals no significant difference between *Abcd1*^{-/-} mice and controls at any tested time point. (13 months, n=3 (CTR), n=8 (*Abcd1*^{-/-}); 15 months, n=12 (CTR), n=17 (*Abcd1*^{-/-}); 18 months, n=7 (CTR), n=8 (*Abcd1*^{-/-}); error bars: mean \pm s.e.m; Student's T-test was applied for each time point).

B) Behavioral assessment of heat sensation, using the plantar Hargreaves test, shows no significant difference between *Abcd1*^{-/-} mice and controls at all tested time points. (13 months, n=5 (CTR), n=8 (*Abcd1*^{-/-}); 15 months, n=14 (CTR), n=18 (*Abcd1*^{-/-}); 18 months, n=7 (CTR), n=8 (*Abcd1*^{-/-}); error bars: mean \pm s.e.m; Student's T-test was applied for each time point).

2.7.2 Absence of myelin alterations and axonal loss in aged *Abcd1*^{-/-} mice

Electrophysiological analysis of 20 months old *Abcd1*^{-/-} mice revealed reduced nerve conduction velocity, but no decrease of compound muscle action potential amplitudes. This led to the assumption that myelin abnormalities, rather than axonal loss, are a substantial feature of their pathology (Pujol et al., 2002). Nevertheless, acute demyelination is neither observed in CNS nor PNS of *Abcd1*^{-/-} mice until the age of 21 months (Forss-Petter et al., 1997; Kobayashi et al., 1997; Pujol et al., 2002). Hypomyelinated axons, interpreted as a result of demyelination or remyelination, were detected in 22 months old mice (Pujol et al., 2002). Therefore, semithin sciatic nerves cross sections of 22 months old *Abcd1*^{-/-} mice were stained for methylene blue/ azur II to analyze myelin sheaths. Also here, no signs of acute demyelination were observed

and myelin sheath thickness appeared comparable to age-matched controls (Fig. 28A). This was further evaluated by g-ratio analysis, confirming normal myelin sheath thickness for all analyzed axonal diameters and a similar mean g-ratio in *Abcd1*^{-/-} nerves (Fig. 28B). Besides potential demyelination, other myelin alterations could account for reduced nerve conduction velocities. Focal hypermyelination, as well as myelin infoldings, were observed in nerves from 16 and 21 months old *Abcd1*^{-/-} mice (Pujol et al., 2002). We detected similar myelin inclusions in nerves of 22 months old mice of both genotypes at comparable frequency, assuming these were age-dependent, not genotype-related effects (Fig. 28C).

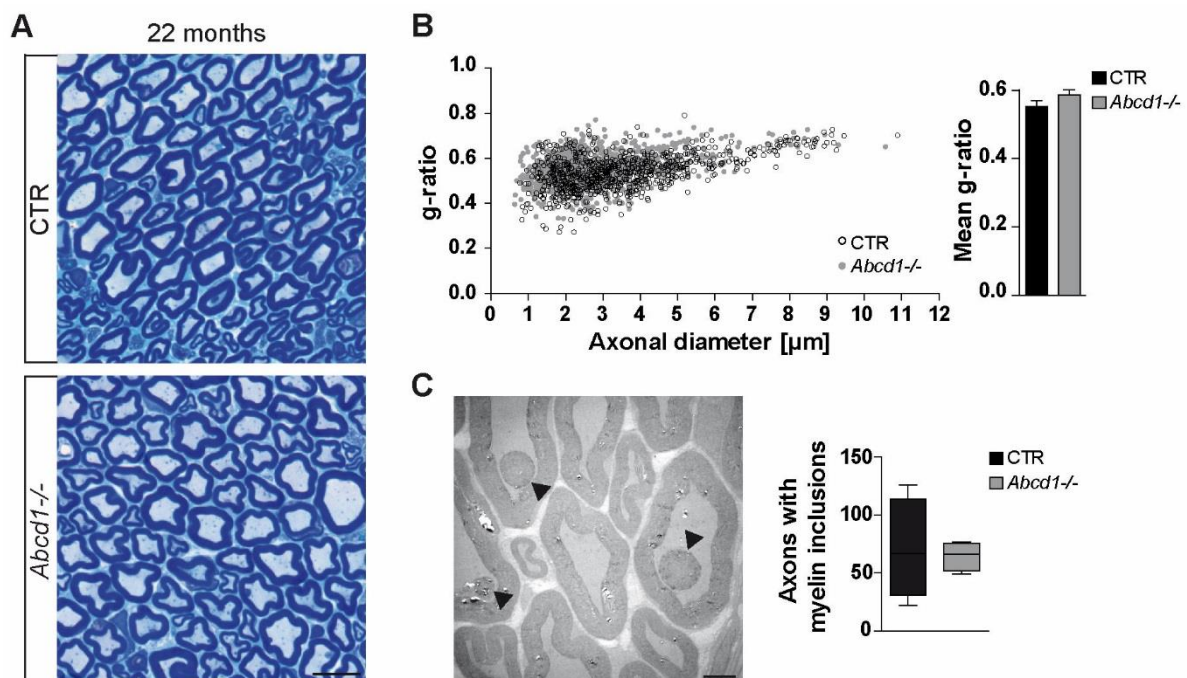


Fig. 28: Normal myelin thickness and age-related myelin inclusions

A) Methylene blue/azur II stained semithin cross sections of sciatic nerves from 22 months old mice reveal normally myelinated axons in *Abcd1*^{-/-} nerves. Scale bar: 10 μ m.

B) Quantification of myelin sheath thickness by g-ratio analysis (axonal diameter divided by complete fiber diameter) from ultrathin sciatic nerve cross sections of 22 months old controls (black) and *Abcd1*^{-/-} mice (grey). Myelin thickness is comparable between controls and mutants for all axonal diameters. Quantification of mean g-ratio depicts similar values for controls (0.55) and mutants (0.59). (n=3, \geq 100 randomly chosen axons per animal, error bars: mean + s.e.m, Student's T-test).

C) EM micrograph showing myelin inclusions (arrow head) in axons of 22 months old control nerves. Quantification of axons with myelin inclusions indicates no significant difference between control and *Abcd1*^{-/-} nerves. (n=4, error bars: mean + s.e.m, Student's T-test).

Despite normal CMAP amplitudes, Pujol et al. suggested signs of axonal damage secondary to myelin abnormalities in 21 months old *Abcd1*^{-/-} sciatic nerves. Moreover, axonal degeneration has been shown in spinal cord (Pujol et al., 2002). Therefore, axonal loss was investigated from complete sciatic nerve cross sections of 22 months old mice. Interestingly, the distribution of axons in *Abcd1*^{-/-} nerves was comparable to that of controls (Fig. 29A). Furthermore, there was neither loss of small (axonal diameter <3 μm) nor of large (axonal diameter $\geq 5\mu\text{m}$) caliber axons (Fig. 29B). Also, the number of myelinated axons per nerve was similar between both genotypes (Fig. 29C). Taken together, *Abcd1*^{-/-} sciatic nerves do not show considerable myelin alterations or axonal loss even at the age of 22 months of age. This suggests other structural nerve alterations, such as disturbed Kv1.1 clustering, as a cause of electrophysiological alteration.

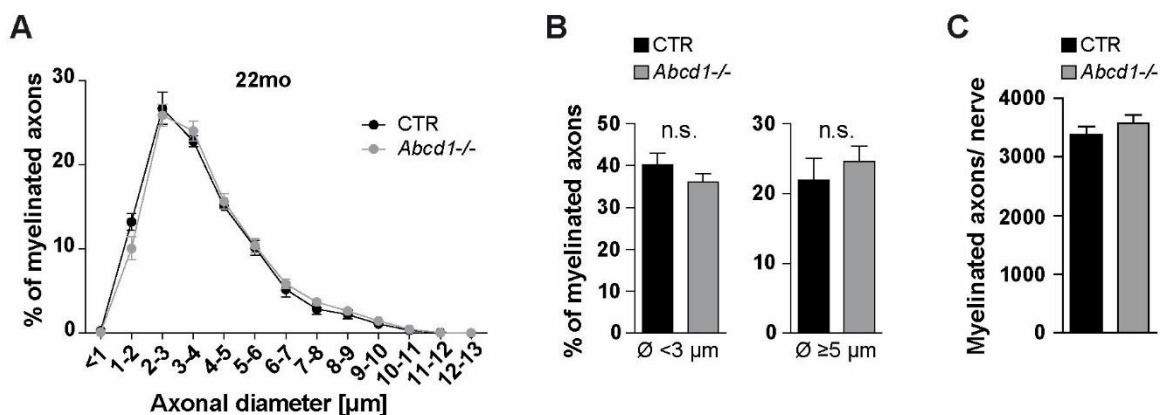


Fig. 29: No axonal loss in *Abcd1*^{-/-} sciatic nerves

A) Analysis of axon distribution in complete cross sections of sciatic nerves from 22 months old mice shows normal axon distribution in *Abcd1*^{-/-} nerves. (n=4 per group; error bars: mean \pm s.e.m, Two-way ANOVA followed by Bonferroni test).

B) Quantification of small caliber axons (diameter <3, left graph) and large caliber axons (diameter $\geq 5\mu\text{m}$; right graph) confirmed no axonal loss in 22 months old *Abcd1*^{-/-} nerves. (n=4 per group; error bars: mean \pm s.e.m; n.s., not significant; Student's T-test).

C) The number of myelinated axons is comparable between control and *Abcd1*^{-/-} nerves. (n=4 per group; error bars: mean + s.e.m, Student's T-test).

2.7.3 Kv1.1 channel clustering is impaired in aged *Abcd1*^{-/-} mice

Abcd1^{-/-} mice develop reduced nerve conduction velocities at around 16 months of age (Pujol et al., 2002), but like *Cnp-Cre::Pex5*^{flox/flox} animals they do not show considerable signs of peripheral demyelination or axonal degeneration (Fig. 28, 29). To test whether *Abcd1*^{-/-} mice acquire juxtaparanodal potassium channel alterations, the molecular organization of nodes was analyzed on teased sciatic nerve fibers. According to *Cnp-Cre::Pex5*^{flox/flox} mice, nodal ion channels (Nav1.6 and Kv7.2) and their anchoring proteins (β IV-spectrin and ANKG) were normally clustered even in 22 months old mice. Also, paranodal CASPR was unchanged (Fig. 30A, B). In contrast, ectopic internodal Kv1.1 channel clustering was already observed at 2 months of age (Fig. 30 C). Similar to *Cnp-Cre::Pex5*^{flox/flox} nerves, this was progressive with age, resulting in around 24% of nodes that showed internodal Kv1.1 clusters at 22 months of age (Fig. 30D). Interestingly and different from *Cnp-Cre::Pex5*^{flox/flox} mice, aged ABCD1-deficient mice displayed significant Kv1.1 clustering not only at internodes, but also at paranodes (Fig. 30D). In summary, *Abcd1*^{-/-} nerves show comparable, but less pronounced alterations of juxtaparanodal potassium channels like *Cnp-Cre::Pex5*^{flox/flox} nerves, suggesting a common pathomechanism caused by β -oxidation defects.

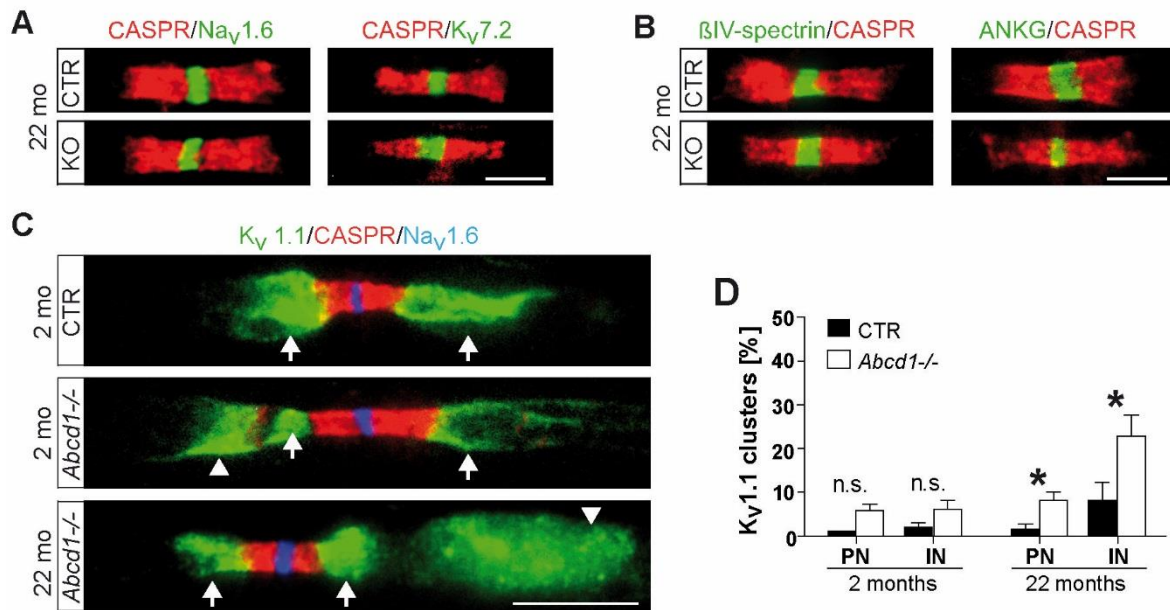


Fig. 30: Ectopic localization of juxtapanodal Kv1.1 proteins despite intact paranodal junctions

A) Immunofluorescent teased fiber staining of 22 months old mice shows normal nodal sodium (Nav1.6) and potassium (Kv7.2) channels (green) flanked by paranodal CASPR (red). Scale bar, 5 μm.

B) Nodal anchoring proteins are normal in *Abcd1*^{-/-} nerves. Scale bar, 5 μm.

C) Immunofluorescent teased fiber staining for nodal Nav1.6 (blue), paranodal CASPR (red) and juxtapanodal Kv1.1 (green) reveals Kv1.1 clusters (arrow head) in addition to normal juxtapanodal patches (arrow) in 2 months and 22 months old *Abcd1*^{-/-} nerves. Scale bar, 10 μm.

D) Percentage of Kv1.1 clusters in the paranode (PN) or internode (IN) is slightly enhanced in 2 months old *Abcd1*^{-/-} nerves and gets significantly increased in 22 months old *Abcd1*^{-/-} nerves. (2months, n=4, ~ 60 nodes counted per animal; 22 months, n=6, 20-40 nodes counted per animal; error bars: mean + s.e.m, n.s. not significant, *p < 0.05, Student's T-test).

2.7.4 Lysosomal alterations and abnormal Schmidt-Lanterman incisures

Considering incorporation of VLCFA in gangliosides as one major step towards secondary lysosome accumulation in *Cnp-Cre::Pex5^{flox/flox}* nerves, ABCD1-deficiency was expected to induce similar problems in the lysosomal compartment. To test this hypothesis, teased sciatic nerve fibers were co-stained with CASPR and LAMP1 or LIMP2 respectively. Like in *Cnp-Cre::Pex5^{flox/flox}* nerves, lysosome-associated vesicles were enlarged and enriched near nodes of Ranvier in nerves obtained from 22 months old *Abcd1*^{-/-} mice (Fig- 31A, B). Furthermore, immuno-electron microscopy highlighted abnormally enlarged Schmidt-Lanterman incisures (SLI) that contained LAMP1-positive accumulates (Fig. 31C). Additionally, immunofluorescent staining of MAG revealed increased number of SLI in 22 months old *Abcd1*^{-/-} nerves (Fig. 31D). This was further confirmed by quantification of SLI, showing significantly more incisures in *Abcd1*^{-/-} nerves aged 22 months, but not at 2 months of age (Fig. 31E). In conclusion, lysosomal alterations were also apparent in aged *Abcd1*^{-/-} nerves, speaking for a role of deficient β -oxidation in disease progression.

To clarify, if ABCD1-deficiency causes functional impairment of lysosomes, as in *Cnp-Cre::Pex5^{flox/flox}* mice, the enzymatic activity of α -mannosidase and β -hexosaminidase was measured in sciatic nerve lysates from 22 old mice. As expected from the less pronounced phenotype of SLI increase and ectopic K_v1.1 clusters, α -mannosidase enzyme activity was unaltered in aged *Abcd1*^{-/-} nerves (Fig. 32A). However, β -hexosaminidase enzyme activity almost reached significance, showing comparable values than 9 months old *Cnp-Cre::Pex5^{flox/flox}* nerves (14.75 ± 1.61 mU/mg in *Abcd1*^{-/-} nerves compared to 16.54 ± 1.68 mU/mg in *Cnp-Cre::Pex5^{flox/flox}* nerves, Fig. 25 and 32B). In summary, these findings suggest secondary lysosome alterations due to defects in peroxisomal β -oxidation.

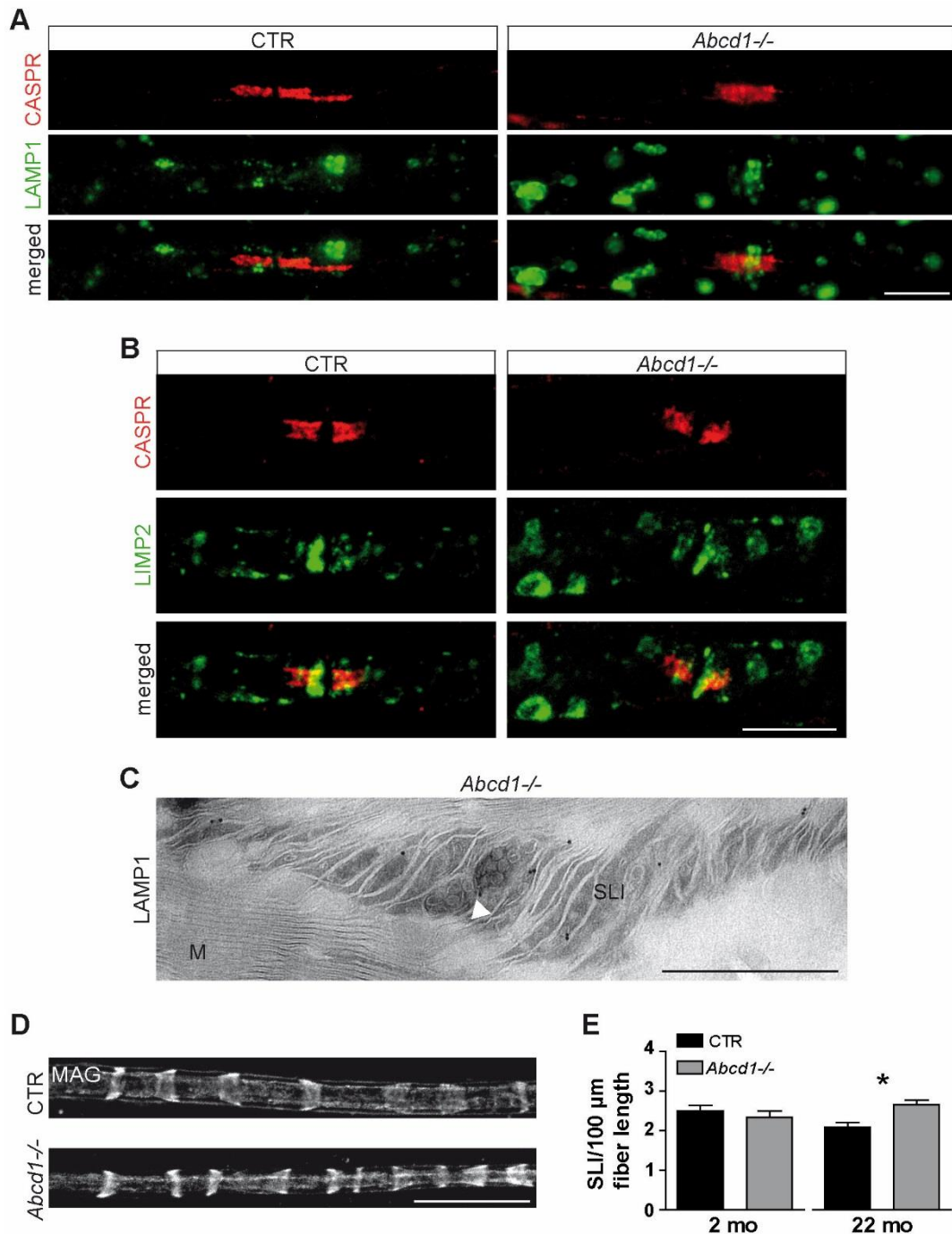


Fig. 31: Accumulation of lysosome-associated vesicles in regions of non-compact myelin

A-B) Immunofluorescent images of teased sciatic nerves from 22 months old mice shows abundant and enlarged LAMP1- and LIMP2-positive vesicles (green) at paranodes (CASPR, red) of *Abcd1*^{-/-} nerves. Scale bars, 10 μ m.

C) Immuno-gold labeling of ultrathin longitudinal sciatic nerve sections from 22 months old *Abcd1*^{-/-} mice demonstrates enlarged Schmidt-Lanterman incisures (SLI) that contain multivesicular bodies, positive for LAMP1 (arrow head). M, myelin. Scale bars, 500 nm.

D) Immunofluorescent staining for MAG indicates increased number of SLI in 22 months old *Abcd1*^{-/-} nerves. Scale bar, 50 μ m.

E) Quantification of SLI per 100 μ m fiber length demonstrates significantly increased number of SLI in *Abcd1*^{-/-} mice aged 22 months, but not in 2 months old mice. (2 months, n=3 (CTR), n=4 (*Abcd1*^{-/-}); 22 months, n=4 (CTR), n=5 (*Abcd1*^{-/-}); error bars: mean + s.e.m, *p < 0.05; Student's T-test).

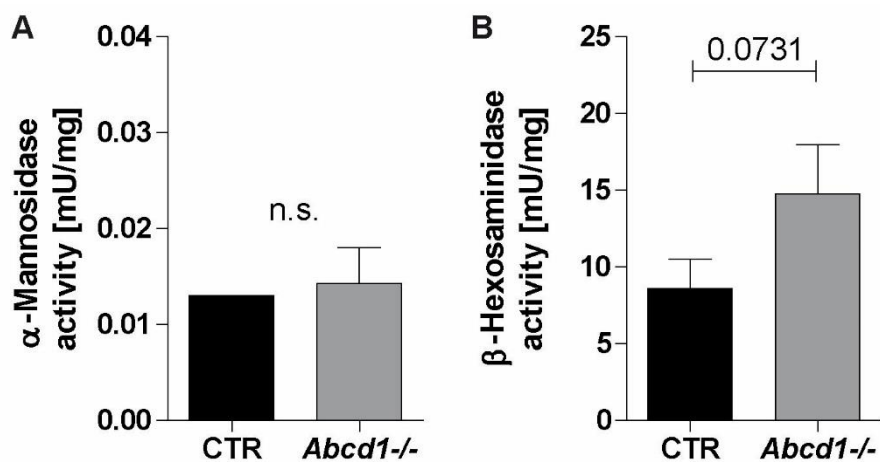


Fig. 32: Lysosomal enzyme activity in *Abcd1*^{-/-} nerves

A-B) Enzyme activity assay of sciatic nerves lysates from 22 months old mice reveals no differences in α -mannosidase activity, but almost significantly elevated β -hexosaminidase activity in *Abcd1*^{-/-} nerves (n=3 (CTR), n=4 (*Abcd1*^{-/-}); error bars: mean + s.e.m; Student's T-test).

3. Discussion

Electrical properties of myelinated axons depend on insulation through myelin and on the distinct molecular organization of ion channels at nodes of Ranvier (Waxman and Ritchie, 1985; Peles and Salzer, 2000). Complex interactions between axons and myelinating glia are required to achieve such properly functional myelination of axons (Pereira et al., 2012). Myelin membranes underlie continuous turnover (Ando et al., 2003) and alterations in their composition result in neural dysfunctions. Myelin sheaths are highly enriched in lipids (~70% of dry mass; Garbay et al., 2000), which are likely particularly vulnerable to deficiencies in lipid metabolism. The essential role of peroxisomes for the nervous system is evidenced by peroxisomal disorders (Gould and Valle, 2000; Steinberg et al., 2006; Wanders and Waterham, 2006). These organelles are associated with cellular lipid metabolism, but underlying molecular mechanism of peroxisomal dysfunction causing myelin abnormalities, axon degeneration, and neuroinflammation are unresolved. Therefore, the *Cnp-Pex5* mouse model was used to study the role of myelin-associated peroxisomes in SC-axon interaction.

3.1 PEX5-deficiency disrupts peroxisomal function in SC

Since PEX5 is the major import receptor of peroxisomal matrix proteins, its ablation causes widespread peroxisomal dysfunction (Gould and Valle, 2000; Stanley et al., 2006). One major function of peroxisomes is chain-shortening of fatty acids through β -oxidation. Since VLCFA are exclusively degraded by peroxisomes, they accumulate in plasma and tissue of patients with peroxisomal disorders and are therefore used as a biomarker for diagnosis (Wanders, 2004a; Wanders and Waterham, 2006). Using lipid mass spectrometry we verified disturbed peroxisomal β -oxidation by showing significantly enhanced C24:0 and C26:0 levels in sciatic nerves of *Cnp-Cre::Pex5^{lox/lox}* mice (Fig. 8D). High concentrations of these saturated VLCFA disturb cellular Ca^{2+} homeostasis, cause mitochondrial dysfunction, and enhance oxidative stress *in vitro* (Fourcade et al., 2008; Baarine et al., 2012). Moreover, cytotoxic effects especially impair oligodendrocytes (Hein et al., 2008). Nevertheless, plasmatic VLCFA-levels of X-ALD patients are not sufficient to induce cell death and organelle dysfunction *in vitro*

(Baarine et al., 2012). Therefore, the actual role of excess VLCFA in the disease progression is still under debate.

Ether phospholipid synthesis, another peroxisomal function, was also disturbed in conditional PEX5 mutants as evidenced by lipid mass spectrometry. Plasmalogens were reduced by almost 70% and phosphatidylethanolamines were significantly increased (Fig. 8A, B). *In vivo* studies showed that neurodegenerative symptoms, potentially caused by VLCFA-accumulation, can be modulated by plasmalogens (Brites et al., 2008). Since plasmalogens are highly abundant in myelin membranes, their reduction has further consequence for the nervous system, including progressive cerebral atrophy, myelin abnormalities and gliosis (Braverman and Moser 2012; Poulos et al., 1988). Structural membrane alteration as well signaling defects have been observed in fibroblast from patients with deficient plasmalogen synthesis (Thai 2001; Perichon 1998). *In vivo* studies revealed myelin defects and disturbed axo-glial interaction at paranodes of plasmalogen-deficient mice (Teigler et al., 2009; Braverman and Moser 2012). Peroxisomal dysfunction causes oxidative stress due to elevated reactive oxygen species (ROS), such as hydrogen peroxide, a typical byproduct of peroxisomal β -oxidation that has to be degraded via peroxisomal catalase (Fransen et al., 2012). We found peroxisomal catalase no longer colocalized with the peroxisomal membrane marker PMP70, but distributed in the cytoplasm (Fig. 7C). Deficient import of catalase is a frequent finding of peroxisomal defects and has been shown to provoke multiple peroxisomal enzyme deficiencies due to elevated ROS (Sheikh et al., 1998). In summary, we clearly demonstrated a general dysfunction of SC peroxisomes upon PEX5 ablation as indicated by deficient peroxisomal β -oxidation, reduced plasmalogen synthesis and cytoplasmic catalase.

3.2 Impaired nerve function despite normal myelin and axon distribution

Ex vivo electrophysiology revealed massively impaired sciatic nerve function in 2 months old *Cnp-Cre::Pex5^{flox/flox}* mice, which was comparable to electrophysiological alterations observed in myelin-deficient mice (e.g. *shiverer*, Sinha et al., 2005). Considering extensive lipid metabolism defects in sciatic nerves of conditional mutants and the recently published role of myelin-associated peroxisomes in myelin

maintenance (Kassmann et al., 2007), we analyzed sciatic nerves for myelin alterations as a potential cause of reduced nerve conduction. Astonishingly, 2 months old conditional mutants had preserved myelin, as indicated by g-ratio analysis and examination of methylene blue-stained complete nerve cross sections. Although axons with thinner myelin sheaths were occasionally observed in 9 months old conditional mutant nerves, g-ratio analysis did not show considerable differences in comparison to controls (Fig. 12A-C). Since g-ratio analysis includes only a fraction of nerve fibers due to technical restrictions of electron microscopy, analysis of complete nerve sections would potentially disclose minor differences of myelin sheath thickness in aged mutants, which however would not explain massive electrophysiological changes at 2 months of age. Myelin compaction and protein composition were normal, as evidenced by ultrastructural and western blot analysis (Fig. 13 A, B). Merely PLP, which comprises only 0.2% of total protein content in the PNS (Garbay et al., 2000; Patzig et al., 2011), showed significant reduction (Fig. 13C). Thus, reduced nerve conduction velocities that were already apparent at 2 months of age cannot be explained by myelin alterations. Assuming preserved myelin as a prerequisite of axon integrity, we did not expect significant axon loss in sciatic nerves. Indeed, axon distribution was not changed and also the total number of myelinated axons was comparable between controls and conditional mutants. Although very large caliber axons ($\varnothing \geq 7 \mu\text{m}$) were absent from g-ratio analysis of 9 months old *Cnp-Cre::Pex5^{flox/flox}* sciatic nerves, examination of complete nerve cross sections excluded the loss of big axons (Fig. 14). This can be further explained by an underrepresentation of big axons in the g-ratio analysis due to technical restrictions of electron microscopy. Thus, we exclude axonal loss as a cause of reduced amplitudes.

Interestingly, electrophysiological results of PEX5 conditional mutant sciatic nerves differ a lot between *in vivo* and the here performed *ex vivo* measurements, which were clearly more pronounced (Kassmann et al., 2011). Thus, we considered compensatory mechanisms at neuromuscular junctions (NMJs). However, quantification of NMJ number did not reveal significant differences (Fig. 10). Nevertheless, we cannot exclude other molecular changes at synapses that potentially influence *ex vivo* measurements. Most interestingly, peripheral neuropathy upon peroxisomal dysfunction differs fundamentally from CNS pathology, suggesting a rather minor role of peroxisomes in myelin maintenance of the PNS. It was shown that microglia invasion precedes myelin alterations, suspecting an inflammatory demyelination in the CNS of

Cnp-Cre::Pex5^{flox/flox} mice (Kassmann et al., 2007). In addition, studies on *Nes-Cre::Pex5^{flox/flox}* brains also demonstrated activation of the innate immune system upon peroxisome deficiency as the major cause of CNS demyelination (Bottelbergs et al., 2012). Considering only moderate levels of neuroinflammation in sciatic nerves of conditional mutants (Fig. 15), this potentially explains substantial differences between CNS and PNS concerning myelin maintenance. Furthermore, the PNS has a much higher regenerative ability than the CNS (Jessen and Mirsky, 2016). Recently, the capability of SC to degrade myelin after nerve injury was published (Gomez-Sanchez et al., 2015). Another possible explanation for less myelin alterations in the PNS is the distinct expression of PLP. In the CNS, PLP is the major myelin protein that is involved in stabilizing myelin membranes and is thereby essential for axonal function, whereas in the PNS, PLP plays only a minor role and is replaced by P0 (Garbay et al., 2000). Although PLP incorporates VLCFA (Bizzozero et al., 1991), this would have minor impacts on PNS myelin stability. In addition, it has been shown that reduced PLP protein amount has less serious consequences for the integrity of myelin than overexpression or mutations in the PLP gene (Seitelberger, 1995; Simons et al., 2002). We therefore conclude that neither demyelination nor axon degeneration are substantial features of PNS pathology in *Cnp-Cre::Pex5^{flox/flox}* mice.

3.3 Ectopic juxtaparanodal proteins and potential effects on nerve excitability

Fast signal propagation is ensured by distinct molecular domains of myelinated axons that restrict action potentials to nodes of Ranvier (Arroyo et al., 2004; Salzer et al., 2008). These are highly enriched in voltage-gated sodium channels (Nav1.6) that mediate action potential generation (Caldwell et al., 2000). We speculated that disturbed lipid metabolism in SC might alter axo-glial interactions and thereby causes differences in electrophysiological properties. There is evidence that reduced plasmalogen levels affect paranodal junctions through alterations in the synthesis and raft distribution of GPI-anchored contactin (Gorgas et al., 2006; Teigler et al., 2009). Disruption of paranodal junctions in contactin- or CASPR-deficient mice impairs axonal integrity and reduces nerve conduction velocity despite normal myelin compaction (Boyle et al., 2001; Bhat et al., 2001). An essential role of myelin galactolipids

(cerebroside and sulfatide) in the maintenance of axo-glia interactions became evident from mice deficient in galactosyltransferase (CGT^{-/-}; Dupree et al., 1999) and galactosylceramide sulfotransferase (CST^{-/-}, Ishibashi et al., 2002). Although structural changes are less pronounced in the PNS, all of these mutants display a shift of juxtaparanodal K_v1.1/2 channels into the paranodal region. However, the integrity of paranodal junctions was verified by intact transverse bands and preserved autotypic junctions between individual loops of *Cnp-Cre::Pex5^{flox/flox}* sciatic nerves (Fig. 16A-C). Furthermore, nodal ion channels and their axonal anchoring proteins were normally formed and maintained (Fig. 16D, E). In contrast, juxtaparanodal K_v1.1 channels were progressively shifted with age into internodes of *Cnp-Cre::Pex5^{flox/flox}* sciatic nerves (Fig. 17A, C). This unexpected observation was already apparent in 12% of nodes at P19, when potassium channels are just clustered. In compliance with intact paranodal junctions, a prerequisite for juxtaparanodal clustering, K_v1.1 channels were never found within paranodes of conditional mutant nerves. Interestingly, ectopic clusters most frequently appeared in addition to normally located juxtaparanodal patches. Moreover, the mesaxonal pattern of K_v1.1 was still obvious in conditional mutants (Fig. 17B). This led to assume that their initial formation is normal. Hence, their internodal distribution is likely a consequence of deficient maintenance that correlates with disease progression.

Juxtaparanodal K_v1.1 clustering and maintenance depend on CASPR2 and TAG-1, which form a heterodimer that is attached to the glial membrane via TAG-1 (Poliak and Peles, 2003; Traka et al., 2003). Immunofluorescent staining of teased fibers for CASPR2 and TAG-1 showed internodal clustering of both anchoring proteins, which was progressive with age (Fig. 18A, B). Costaining with K_v1.1 as well as quantification of TAG-1/K_v1.1 colocalization in ectopic patches clearly showed a shift of the complete juxtaparanodal complex to internodes (Fig. 18C-E). This is in line with published data obtained from *Caspr2^{-/-}* and *Tag-1^{-/-}* mice, demonstrating that juxtaparanodal clustering of both proteins is interdependent and deficiencies in either protein impair juxtaparanodal clustering of K⁺ channels (Poliak and Peles, 2003; Traka et al., 2003). Analyzing mice with a Schwann cell-specific defect, we hypothesized that disturbed juxtaparanodal clustering in conditional mutant nerves is provoked by deficient membrane anchoring of glial TAG-1 (Traka et al., 2002; 2003). Although this assumption cannot be proven by TAG-1 immunofluorescence, it has been shown by Savvaki et al. that glial TAG-1 is sufficient for juxtaparanodal organization and

maintenance of CASPR2 and Kv1.1 in the CNS (Savvaki et al., 2010). Additionally, Zhang et al. demonstrated that adhesion molecules are freely diffusible within membranes and accumulate through interactions with Schwann cell ligands, whereas ion channels and cytoskeletal proteins are rather immobile and rely on selective anterograde transport from neuronal cell bodies (Jensen et al., 2011; Zhang et al., 2012). These observations let assume that glial TAG-1 likely diffuses into internodes as a result of SC-specific signals. It has been shown that TAG-1 is a glycosylphosphatidylinositol (GPI)-anchored cell adhesion molecule that is associated with ganglioside-rich lipid rafts (Kasahara et al., 2000; Loberto et al., 2003). Since cholesterol is a major component of lipid rafts and is enriched in conditional mutant nerves, we suspect that this could further stabilize raft-associated binding of TAG-1. Consequently, the whole juxtaparanodal complex would drift into internodes. This would imply that newly synthesized Kv1.1, which is transported to nodes, is trapped at ectopic TAG-1/CASPR2 clusters. Western blot analysis highlighted elevated Kv1.1 protein amounts in sciatic nerves of aged conditional mutants (Fig. 17D). However, to confirm enhanced Kv1.1 expression its mRNA abundance in mutant sciatic nerves has to be analyzed by quantitative real-time PCR. Furthermore, it would be interesting to check for protein abundance and mRNA expression of TAG-1 and CASPR2 to evaluate the cause of additional ectopic clusters.

Despite their important role in nerve excitability during development (Vabnick et al., 1999), the function of juxtaparanodal Kv1.1 channels in mature myelinated fibers is still elusive. However, they are supposed to maintain the resting potential and prevent repetitive and aberrant firing. Thus, it has been shown that Kv1.1 ablation, as well as specific blocking with 4-aminopyridine (4-AP) or dendrotoxin-K (DTX-K), result in nerve hyperexcitability by decreasing firing thresholds (Sherratt et al., 1980; Smart et al., 1998; Chi and Nicol, 2007). Reduced or even absent juxtaparanodal clustering of Kv1-channels is also associated with nerve hyperexcitability in type 2 diabetes mellitus (Zenker et al., 2012). Sensory behavior tests highlighted increased responses to mechanical stimulation (mechanical allodynia) in conditional mutants, but failed to show differences in heat sensation (Fig. 11). Interestingly, similar findings were observed after decreased Kv1.1 expression or inhibition of Kv1.1 by DTX-K-injection into paws. These findings demonstrated that Kv1.1 is capable of regulating sensitivity of fibers associated with mechanical perception (Hao et al., 2013). Elevated Kv1.1 activity is associated with reduced nerve conduction velocities, smaller amplitudes,

reduced excitability, and even high-frequency conduction failure in myelin deficiencies due to exposure of juxtaparanodal K_v1.1 channels (Sinha et al., 2005; Bagchi et al., 2014). Assuming a role for juxtaparanodal K_v1.1 channels in dampening the conduction of myelinated fibers to prevent aberrant excitation, we suggest that additional internodal K_v1.1 clusters could have similar effects on nerve excitability due to gradual membrane hyperpolarization. This in turn would slow nerve conduction through elevated thresholds and, in severely affected fibers, may even cause conduction blocks. To directly proof this hypothesis, the functionality of internodal K_v1.1 channels has to be evaluated. However, voltage-clamp recordings of single axons underneath compact myelin is to our knowledge impossible so far. Another potential approach to check for the contribution of additional K_v1.1 channels on nerve excitability would be the specific block of these channels through 4-AP or DTX-K administration and subsequent recording of nerve responses upon stimulation. Nevertheless, it has been shown that intact compact myelin prevents the inhibitory effect that these blockers have on K_v1.1 channels (Vabnick et al., 1999).

3.4 Peroxisomal dysfunction disturbs ganglioside homeostasis

Gangliosides make up 10-12% of neuronal membrane lipids and rely on lysosomal degradation (Sandhoff and Harzer, 2013). It has been demonstrated that they incorporate excessive VLCFA (Saito and Saito, 1991). Accordingly, we detected an elevated portion of GD1-species bound to VLCFA (Fig. 19A). In compliance with suspected degradation defects of VLCFA-bound gangliosides, we found dispersed and elevated GM1 and GD1a staining in sciatic nerves (Fig. 19B-D). In line with our findings, brain gangliosides of X-ALD patients contain high percentages of fatty acids with chain lengths exceeding 22 C-atoms (Igarashi et al., 1976a) and secondary storage of GM1 and GM2 gangliosides were observed in Zellweger and infantile Refsum patients (Tatsumi et al., 2001). It is further speculated that VLCFA-esterified gangliosides trigger immune responses and impede membrane turnover, potentially provoking destabilization of myelin membranes in the brain (Ho et al., 1995). This in turn potentially disturbs axo-glial interaction and eventually causes axonal loss due to deficient support (Berger et al., 2014). Although GM1 accumulation can elicit neuronal cell death through the activation of an unfolded protein response (Vitner et al., 2010),

the number of axons was not changed in *Cnp-Cre::Pex5^{flox/flox}* nerves (Fig. 14). Due to its widespread influence on intracellular signaling, GM1 abundance might however have further effects on cellular homeostasis (de Chaves and Sipione, 2010). Since gangliosides regulate membrane dynamics and organize myelinated fibers (Susuki et al., 2007; Labasque and Faivre-Sarrailh, 2010), we propose that ganglioside perturbations likely cause juxtaparanodal alterations. This is supported by studies that show interaction of TAG-1 with GM3, GM1, and GD1b *in vitro* (Loberto et al., 2003; Prioni et al., 2004). Influence of gangliosides on TAG-1 activity in the cerebellum indicates similar functions in myelinated fibers (Kasahara et al., 2000; de Chaves and Sipione, 2010). Verifying the interaction of TAG-1 and GM1 in PEX5-deficient nerves would require immunofluorescent colabeling, which is however difficult to achieve *in vivo*. To approach the assumption of ectopic internodal TAG-1 due to altered ganglioside distribution, the proportion of gangliosides within the glial membrane will be analyzed in sciatic nerve membrane fractions using lipid mass spectrometry.

3.5 Pex5-deficiency in SC mimics symptoms of lysosomal storage disorders

Peroxisomal and lysosomal disorders share common pathological features (Faust et al., 2010) and deficiencies in either organelle appear to influence the other (Launay et al., 2015; Schedin et al., 1997; Haq et al., 2006). Recently, it has been shown that cholesterol is transported from peroxisomes to lysosomes through dynamic membrane contacts *in vitro*. These contacts appeared to be less prominent upon peroxisomal dysfunction, resulting in cholesterol accumulation within lysosomes (Chu et al., 2015). According to these findings, we could confirm close association of both organelles at paranodal regions *in vivo* (Fig. 20). In support of an *in vivo* interaction of the two organelles, peroxisome proliferator-activated receptor- α (PPAR- α), a transcription factor that is involved in regulating peroxisomal abundance (Mandard et al., 2004), is downregulated in Krabbe disease, a lysosomal storage disorder (Haq et al., 2006). In addition, peroxisomal β -oxidation as well as catalase activity are decreased in Niemann-Pick disease (NPC1; Schedin et al., 1997). Based on the perturbation of gangliosides, a common cause of lysosomal storage disorders, we suspected secondary alterations of the lysosomal compartment in *Cnp-Cre::Pex5^{flox/flox}* nerves.

Indeed, fluorescent teased fiber staining highlighted enlarged GD1a-positive vesicles that were engulfed by LAMP1-positive structures (Fig. 19E, F). This observation strongly indicates a backlog of lysosomal substrates due to a primary defect in peroxisomal lipid metabolism. Accordingly, gangliosides get stuck within lysosomes as a consequence of deficient VLCFA degradation in SC peroxisomes. In compliance with a secondary lysosomal problem, staining for lysosomal membrane proteins as well as western blot analysis revealed enlargement and increased number of lysosomes (Fig. 21, 24). Interestingly, abundant lysosomes occurred despite down-regulation of relative mRNA expression of *Lamp1* and *Limp2*, suggesting a secondary accumulation rather than an overproduction. Using endosomal-related markers, the lysosomal identity of accumulated vesicles was verified (Fig. 22). Decreased relative mRNA expression of *MAP1LC3* in aged *Cnp-Cre::Pex5^{flox/flox}* nerves potentially demonstrates less autophagic activity (Fig. 22). Inhibition of autophagy due to impaired autophagosome formation was recently shown in X-ALD-related *in vivo* and *in vitro* models (Launay et al., 2015). Moreover, lysosomal storage also elicits autophagy blocks due to deficient fusion of autophagosomes with lysosomes (Settembre et al., 2008). However, if autophagic flux is indeed impaired in conditional mutant nerves has to be clarified. This could be achieved by the investigation of LC3-II levels, using western blot analysis or immunofluorescent staining. In addition, hampered autophagosome-lysosome fusion would become evident by subcellular analysis of LC3-II colocalization with LAMP1.

Finding enlarged and excess lysosome-associated vesicles within cytoplasmic SC regions (i.e. within paranodal loops and SLI), the essential role of non-compacted myelin in SC metabolism and consequential support of axons was stressed. According to this, lysosomal origin of previously described paranodal inclusions was evidenced by immuno-electron microscopy (Fig. 21A). Similar secondary axonal abnormalities (e.g. spheroids) are typical observations in gangliosidoses (Walkley, 2004). Secondary and progressive lysosomal storage problems were also evidenced by significantly increased numbers of lipid-laden macrophages in 9 months old *Cnp-Cre::Pex5^{flox/flox}* nerves (Fig. 15B, C). GM1/GM2 gangliosidoses are known to elicit an inflammatory response through recruitment of macrophages (Jeyakumar et al., 2003). Similar to *Cnp-Cre::Pex5^{flox/flox}* nerves, T-cell infiltration plays only a minor role in GM1/GM2 gangliosidoses and is only barely detected in advanced disease situations (Fig. 15D, (Jeyakumar et al., 2003). Our hypothesis of secondary endosomal-lysosomal

perturbation was supported by the upregulation of lysosomal β -hexosaminidase and α -mannosidase activity, which is a typical compensatory mechanism of lysosomal storage disorders (Jeyakumar et al., 2005). Since β -hexosaminidase hydrolyses GM2 gangliosides, a precursor of GM1 and GD1a, we assume that its elevated enzyme activity attempts to compensate the secondary storage of these gangliosides in conditional mutant nerves.

Since most peroxisomal disorders as well as lysosomal storage disorders result in CNS pathology (Vellodi, 2005; Wanders and Waterham, 2006), one next step is to analyze whether peroxisomal dysfunction in oligodendrocytes has similar effects on lysosomal abundance and function in the CNS of *Cnp-Cre::Pex5^{flox/flox}* mice. Thus, the most important question is to which extent lysosomal alterations might affect disease progression in the CNS of conditional mutants. Potential *in vivo* interactions of peroxisomes and lysosomes in the brain would also facilitate the understanding of other neurodegenerative disorders, such as Alzheimer's disease or Niemann-Pick disease.

3.6 Increased number of SLI- a consequence of lysosomal storage?

Schmidt-Lanterman incisures provide a direct and fast radial diffusion pathway through myelin and are therefore supposed to have a metabolic function in myelin maintenance (Balice-Gordon et al., 1998; Arroyo and Scherer, 2000). Interestingly, morphology and increase of SLI, especially in 9 months old *Cnp-Cre::Pex5^{flox/flox}* mice, was comparable to observations made in sciatic nerves of *shiverer* mice. Gould et al. discussed that closely apposed SLI, either represent newly formed SLI or result from biochemical disturbances and subsequent defects in membrane-cytoskeleton interaction (Gould et al., 1995). It has been shown that the number of SLI correlates with the axonal diameter (Hiscoe, 1947; Small et al., 1980; Ghabriel and Allt, 1981) and is markedly increased when SC-axon interactions are disturbed (Gould et al., 1995; Dupree et al., 1998; Hoshi et al., 2007). Also, alterations of SLI play a role during Wallerian degeneration (Ghabriel and Allt, 1979). Thus, it is presumed that SLI protect peripheral nerves from mechanical stress by providing flexibility (Singer and Bryant, 1969). *Myelin-associated glycoprotein* (MAG), which is abundant in SLI, binds axonal gangliosides (GD1a, GT1b) to mediate adhesion to axonal membrane (Yang et al., 1996; Collins et al., 1997;

Pan et al., 2005). We therefore speculate that perturbed GD1a distribution likely affects this interaction. Thus, increased number of SLI may either result from excess GD1a or might be a compensatory process to sustain SC-axon interaction and thereby ensure axon stability. Studies on *Mag*-null mice revealed its essential function in controlling axon outgrowth, diameter, and integrity (McKerracher et al., 1994; Yin et al., 1998). *In vitro* studies further demonstrated that MAG protects neurons from acute toxicity through ganglioside-mediated signaling (Mehta et al., 2010). Another potential cause of enlarged and increased SLI is providing additional space for storage of excess lipid-containing vesicles. This hypothesis is underpinned by massive presence of LAMP1-positive accumulations within incisures (Fig. 23B). Regardless of the underlying reason of SLI abnormalities, increased portion of non-compacted myelin presumably adds to the observed nerve impairment by causing a decreased resistance, especially in aged conditional mutant nerves.

3.7 ABCD1-deficiency results in similar, but less severe neuropathy

Neuropathy of *Abcd1*^{-/-} mice is suggested to be triggered by early-onset oxidative stress rather than neuroinflammation (Fourcade et al., 2008; Galea et al., 2012). In consistence with previous studies, demyelination was not observed even in nerves of 22 months old *Abcd1*^{-/-} mice (Fig. 28A, B; Forss-Petter et al., 1997; Kobayashi et al., 1997). Moreover, focal hypermyelination and myelin infoldings, which had been observed in an X-ALD mouse model earlier (Pujol et al., 2002), were found to similar extent in age-matched controls (Fig. 28C). This let assume that in the here analyzed *Abcd1*^{-/-} mouse model these late-onset abnormalities are not genotype-specific but age-related. In line with this, several age-dependent myelin alterations have been described in monkeys and rats (Peters, 2002; Xie et al., 2014). The here reported age-dependent decline of motor performance, and especially grip strength when assessed in 13, 15, and 18 months was not a result of axonal loss (Fig. 26 and Fig. 29). These findings contradict previously published results, proposing axonal damage in 21 months old *Abcd1*^{-/-} sciatic nerves (Pujol et al., 2002). We assume that these distinct findings, regarding myelin alterations and axonal damage, might result from different technical approaches and the analysis of two different ABCD1 mouse models. Thus, the ABDC1 mouse model generated by Forss-Petter et al. was analyzed in the present

study, whereas Pujol et al. investigated the ABCD1 mouse model generated from Lu et al. (Forss-Petter et al., 1997; Lu et al., 1997; Pujol et al., 2002).

Despite different primary peroxisome defects, *Abcd1*^{-/-} and *Cnp-Cre::Pex5^{flox/flox}* sciatic nerves show similar pathological features, assuming a common pathomechanism related to dysfunction of peroxisomal β -oxidation that secondarily involves lysosomes. Thus, aged *Abcd1*^{-/-} mice display ectopic K_v1.1 channels and lysosomal impairment (Fig. 30, 31 and 32). Nevertheless, *Abcd1*^{-/-} mice are less affected and show abnormalities only very late. This can be further explained by a complete loss of peroxisomal function in *Cnp-Cre::Pex5^{flox/flox}* nerves, whereas *Abcd1*^{-/-} nerves exhibit only a partial defect of peroxisomal β -oxidation. Synergistic effects of disturbed peroxisomal β -oxidation and plasmalogen-deficiency on neurodegeneration have been shown in other *in vivo* mouse models and might explain the more pronounced neuropathology of *Cre::Pex5^{flox/flox}* nerves (Brites et al., 2008). Moreover, besides ABCD1, two other peroxisomal transporters (ABCD2 and ABCD3) are present in the peroxisomal membrane (Kamijo et al., 1990; Lombard-Platet et al., 1996). Although ABCD3 is less efficient than ABCD1 in mediating the peroxisomal import of VLCFA-CoA, it was shown to partially compensate the loss of ABCD1 and rescue metabolic defects in X-ALD patient's fibroblasts when overexpressed (Netik et al., 1999; Wiesinger et al., 2013). Also, ABCD2 overexpression prevents VLCFAs accumulation as well as neurodegenerative features of *Abcd1*^{-/-} mice (Pujol et al., 2004).

Electrophysiological measurements are commonly used in X-ALD patients to discriminate between demyelinating and axonal neuropathy. Our analysis of *Cnp-Cre::Pex5^{flox/flox}* however demonstrated that electrophysiological changes can result from other pathological features than myelin alterations or axonal loss. Therefore, additional diagnostic tools, such as nerve biopsies might help to precisely categorize the neurodegenerative cause of neuropathies.

3.8 Model of Cnp-Pex5-deficiency

This work showed that peroxisomal dysfunction in Schwann cells elicits secondary problems in other compartments of lipid metabolism such as lysosomes. We propose a model of deficient ganglioside digestion within lysosomes due to the incapability of PEX5-deficient SC to degrade VLCFA, including those that are incorporated into gangliosides. Consequently, VLCFA-esterified gangliosides are stored within lysosomes and will accumulate in myelin membranes. As a result of altered lipid composition of the glial membrane, glial GPI-anchored TAG-1 eventually shifts towards internodes. Subsequently, the complete juxtaparanodal complex, besides glial TAG-1, consisting of axonal TAG-1, CASPR2, and $K_v1.1$ -channels, drifts into the internode. Assuming intactness of extra $K_v1.1$ -channels, more K^+ ions are shuttled into the periaxonal space, provoking gradual membrane hyperpolarization, which consequently reduces nerve conduction (Fig. 33). Hence, this study expands the importance of SC lipid metabolism for normal nerve function, independent of myelin. Whether disturbed potassium channel clustering also plays a role in lysosomal storage disorders has to be investigated.

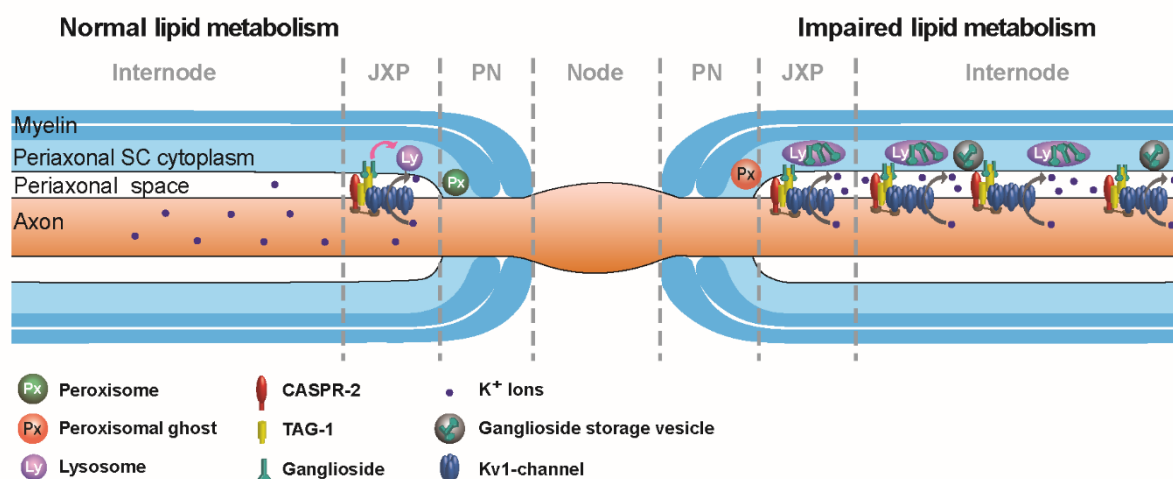


Fig. 33: Hypothetical model of Cnp-Pex5-mediated pathomechanism in myelinated fibers

Normal lipid metabolism (left) comprises the degradation of VLCFA within peroxisomes (green) through β -oxidation and ganglioside digestion within lysosomes (purple). Both organelles reside within cytoplasmic SC regions and are closely associated. When SC lipid metabolism is impaired (right) due to peroxisomal dysfunction (orange), gangliosides incorporate excess VLCFA, are consequently stored within lysosomes, and accumulate within membranes. The juxtaparanodal complex is thereby shifted towards internodes, resulting in additional $K_v1.1$ channels and potential membrane hyperpolarization.

4. Material

4.1. Equipment

All chemicals and materials that are not explicitly mentioned are obtained from Roche, BD Falcon, Eppendorf, Merck, Sartorius, Serva and Sigma.

Kits

DAB Zytomed Kit	Zytomed Systems GmbH
DC Protein Assay (Lowry)	Bio-Rad
LSAB2 kit	Dako
nexttec™ 1-Step DNA isolation	Nexttec Biotechnology
RNeasy Mini kit	Qiagen (Portland, USA)

Pipettes

Pipetboy2	Integra Biosciences
Pipettes	Gilson
Tips	Gilson

Protein biochemistry and enzyme assays

ChemoCam Imager ECL HR-16-3200	Intas
Eon microplate spectrophotometer	BioTek
Intas ChemoStar	Intas
Novex® Semi-Dry Blotter	Thermo Fisher Scientific
PowerPac 300 Powersupply	Bio-Rad
Precellys® 24	Precellys
SDS-PAGE gel casting and running units	Bio-Rad
Table-top centrifuge	Heraeus Sepatech
Table-top thermomixer	Eppendorf

Molecular biology

7500 Fast Real-Time PCR System	Applied Biosystems
PCR-machine	PeqLab
INTAS UV-system with Camera and printer	Intas
NanoDrop200 Spectrophotometer	Thermo Scientific
Thermomax microplate reader	MGW Biotech

Perfusion of mice

Microlance™ 30 G x ½	BD Bioscience
Peristaltic Pump PD 5101	Heidolph
Preparation platform with drainage	In-house made
Syringe 1 ml	BD Bioscience
Venofix® 0.4 x 10 mm	Braun
Waterbath	ÖTTI

Histology

Cover glass (50 x 24 mm, 0.17 ± 0.01 mm)	Assistant
Dumont forceps (#3, #5)	Fine Science Tools
HistoBond® slides	Marienfeld
Embedding station HMP110	Microm
Leica Jung Cryocut CM3000	Leica
Menzel slides	Thermo Fisher Scientific
Microwave	Daewoo
Paraffin embedding center AP280-1/-2/-3	Microm
pH meter inoLab pH 720	WTW
Shandon coverplates	Thermo Fisher Scientific
Sliding microtome HM400	Microm
Tissue cassettes IV	Polyscience Inc.

Electron microscopy

Copper grids	Science Services
Cryonizer	Leica
Cryo chamber FC-6	Leica
Cryo-immuno diamond knife	Diatome
Cryo-Trim 20	Diatome
Heatplate	Leica
Ultracut S	Leica
Ultra 45° diamond knife	Diatome
Vibratom VT 1000s	Leica

Microscopes

2048 X 2048 CCD camera	Proscan
Axiocam MRm	Zeiss

Axio Observer. Z1 (HXP120 UV-lamp, Power Supply 23, SMC 2009 stage control)	Zeiss
Axiophot	Zeiss
LEO EM 912AB electron microscope	Zeiss
Stereomicroscope Stemi DV4	Zeiss

Behavior

Dynamic Plantar Aesthesiometer	ugo basile
Elevated beam	In-house made
Grid	In-house made
Plantar Hargreaves Apparatus	ugo basile

Software

Adobe Illustrator CS5
 Fiji
 GraphPad Prism 5
 Mekentosj Papers 3
 Microsoft Excel 2013
 Microsoft Power Point 2013
 Microsoft Word 2013
 Zen 2012 (Zeiss)

4.2 Molecular biology

DNase-Mix

10 μ l DNase
 70 μ l RDD buffer

10 mM dNTP (50x stock)

2.5 mM each nucleotide (dATP, dCTP, dGTP, dTTP) (Boehringer-Ingelheim)
 200 μ M final concentration in a PCR reaction (50 μ M each nucleotide)

TBE 20x (stock solution)

1.8 M TrisBase
 1.8 M Boric acid
 200 mM EDTA

2 % agarose gel

3.5 g agarose
350 ml 1 x TBE buffer

Enzymes

GOTaq DNA polymerase (Promega)
Superscript III-reverse transcriptase (Thermo Fisher Scientific)

4.3 Protein biochemistry**Modified Ripa buffer (protein lysis buffer)**

50 mM Tris-HCl (pH 7.5)
150 mM NaCl
1% [v/v] NP-40
1% [v/v] Triton X-100

Complete Mini protease inhibitor (Roche Diagnostics GmbH, Mannheim, Germany) was added freshly before use (1 tablet/10ml of RIPA buffer).

SDS separating gel (1.5 mm thickness)

10/15% [v/v] Acrylamide / Bisacrylamide 29: 1
0.4 M Tris-HCl pH 8.8
0.1% [w/v] SDS
0.03% [v/v] Ammonium persulfate
0.08% [v/v] TEMED

SDS stacking gel (1.5 mm thickness)

4% [v/v] Acrylamide / Bisacrylamide 29: 1
125 mM Tris-HCl pH 6.8
0.1% [w/v] SDS
0.05% [w/v] Ammonium persulfate
0.1% [v/v] TEMED

4x SDS sample buffer

40% [v/v] Glycerol
240 mM Tris/HCl pH 6.8

8% [w/v] SDS
0.04% [w/v] Bromophenol blue

1x SDS running buffer (Laemmli buffer)

25 mM Tris (hydroxymethyl)-aminomethan (Tris)
192 mM Glycine
1% [w/v] SDS
Dissolved in ddH₂O

10x Transfer buffer

390 mM Glycine
480 mM Tris-Base
10% Methanol was added directly before use and dissolved in ddH₂O to obtain a 1x transfer buffer.

20x Tris buffered saline (TBS)

1 M Tris/HCl, pH 7.4
3 M NaCl

1x TBS with Tween-20 (TBST)

50 mM Tris/HCl, pH 7.5
150 mM NaCl
0.05% [v/v] Tween-20

Blocking buffer

5% [w/v] nonfat dry milk
Dissolved in 1 x TBS

4.4 Lysosomal enzyme assay

Lysis buffer

1% [v/v] Triton X-100
50 mM Tris-HCl pH 7.5
150 mM NaCl
1% [v/v] NP-40

Complete Mini protease inhibitor (Roche Diagnostics GmbH) was added freshly before use (1 tablet/10ml of lysis buffer).

0.2 M Citrate buffer (pH 4.6)

38.4 g Citric acid (M=210,14g/mol)
 0.8 g Sodium azide
 4 g Bovine albumin serum (BSA)

0.9% NaCl solution

0.9 g NaCl
 Dissolved in 100 ml ddH₂O.

0.4 M Glycine/ NaOH (Stop solution)

15 g Glycine
 Dissolved 500ml ddH₂O, pH was adjusted with 1 M NaOH (~200 ml) to 10.4.

Substrates (10 mM)

Dissolved in 0.2 M citrate buffer.

enzyme	substrate	molecular weight	mg in 25 ml buffer
a-Mannosidase	p-nitrophenyl-a-D-mannopyranosid (Sigma N 2127)	301,3	75,3
β-Hexosaminidase	p-Nitrophenyl-N-acetyl-β-D-glucosaminide (Sigma N 9376)	342,3	85,6

4.5 Immunohistochemistry

Avertin

2 g 2,2,2 Tribromethanol 99%
 2 ml tert-Amylalkohol
 96 ml H₂O (40°C)

Avertin was stirred for 30 min and was sterile filtered. The solution was stored at -20°C and heated to 37°C before usage.

Paraformaldehyde (4%)

400 ml 0.2 M NaH₂PO₄ solution

100 ml	0.2 M Na ₂ HPO ₄ solution
100 ml	37% Formaldehyde solution
400 ml	ddH ₂ O

10x Phosphate buffered saline (PBS)

1.7 M	NaCl
0.04 M	KCl
0.04 M	Na ₂ HPO ₄
0.018 M	KH ₂ PO ₄

Dissolved in ddH₂O and adjusted to pH 7.2 with 1 M NaOH.

Blocking buffer teased fibers

10% [v/v]	Horse Serum
0.05% [v/v]	Triton X-100

Dissolved in 1 x PBS

Blocking buffer cryo sections

0.5% [w/v]	Bovine albumin serum (BSA)
0.25% [v/v]	Triton X-100
1% [v/v]	Horse serum

0.01 M Citrate buffer (pH 6.0)

1.8 mM	Citric acid
8.2 mM	Sodium citrate

Prepared freshly before use.

BSA/PBS

0.04 M	NaH ₂ PO ₄
0.16 M	Na ₂ HPO ₄
1.8% [w/v]	NaCl
1.0% [w/v]	Bovine serum albumin (BSA)

Tris buffer (pH 7.6)

50 mM	Tris/HCl, pH 7.6
0.9% [w/v]	NaCl

Prepared freshly before usage.

Mayer's haematoxylin solution

0.1% [w/v] Haematoxylin

0.02% [w/v] NaIO_3

5% [w/v] $\text{K}_2\text{Al}_2(\text{SO}_4)_4 \cdot 24\text{H}_2\text{O}$

Were added under constant shaking.

5% [w/v] Chloral hydrate

0.1% [w/v] Citric acid added

Added and filtered before usage.

Scott's solution

0.2% [v/v] KHCO_3

2% [w/v] MgSO_4

HCl - alcohol

0.09% [v/v] HCl

70% [v/v] Ethanol

Artificial cerebrospinal fluid (ACSF)

126 mM NaCl

3 mM KCl

1.25 mM NaH_2PO_4

26 mM NaHCO_3

2 mM MgSO_4

10 mM Glucose

2 mM CaCl_2

Dissolved in ddH₂O. CaCl_2 was added after 10-20 min oxygenation. The pH was adjusted to 7.2 using 37% HCl.

Mounting media

Aqua-Poly/Mount (Polysciences)

ProLong® Gold (Thermo Fisher Scientific)

Eukitt (Kindler)

Tissue-Tek® O.C.T. Compound (VWR)

4.6 Immuno-electron microscopy

Fixing solution (Immuno Karlsson-Schultz fixative)

4% Formaldehyde solution

0.25% Glutaraldehyde

0.5% NaCl

Dissolved in ddH₂O.

Sucrose (2.3 M)

80 g Sucrose

100 ml Phosphate buffer (0.1 M)

Blocking Buffer

1% BSA

Dissolved in 1 x PBS

Uranyl acetate

4% [w/v] Uranyl acetate

Filtered before use.

4.7 Electron microscopy

Karlsson-Schultz fixative

4% [w/v] PFA

2.5% [v/v] Glutaraldehyde

0.1 M Phosphate buffer

Epon

171.3 g Glycidether 100

115 g DDSA (Dodecenyl succinic anhydride)

89 g MNA (Methyl nadic anhydride)

Mixed for 10 min using a magnet stirrer.

6.5 ml DMP-30

Added and again mixed for 20 min.

Methylene blue/ azure II

1% Na-tetraborat (Borax)

1% Methylene blue

1% Azure II

Methylene blue and Azure II were freshly mixed 1:1 before use.

Formvar solution

1.25% [w/v] Formvar

50 ml Chloroform

Stir for at least 30 min. Protect from light. Store at room temperature.

4.8 Antibodies**Primary antibodies**

4.1G	1:100	IHC	(Ivanovic et al., 2012)
AnkG	1:100	IHC	Prof Matthew Rasband, PhD
ATG5	1:100	IHC	Covalab pab50264
β IV-spectrin	1:400	IHC	Matthew Rasband
CASPR	1:1000	IHC	NeuroMab 75-001
CASPR2	1:500	IHC	Prof. Elior Peles, PhD
Catalase	1:200	IHC	Sigma C0979
CD3	1:150	IHC	Serotec MCA1477
EEA1	1:300	IHC	Abcam ab2900
K _v 1.1	1:50	IHC	Santa Cruz sc11184
K _v 1.1	1:50	IHC	NeuroMab clone 20/78
K _v 7.2	1:1000	IHC	ThermoScientific PA1-929
LAMP1	1:200, 1:400	IHC, IEM, WB	BD Biosciences 553792
LIMP2	1:1000	IHC	Dr. Judith Blanz
MAC-3	1:400	IHC	BD Bioscience 564844
MAG	1:100	IHC, WB	Chemicon #MAB1567 mouse
GD1a	1:150	IHC	Hugh J Willison
GM1	1:50	IHC	Hugh J Willison
Nav1.6	1:500	IHC	Alomone labs ASC-009
NF155	1:000	IHC	Prof. Peter Brophy, PhD
NF200	1:100	IHC	Sigma N4142
P0	1:1000	IHC, WB	(Archelos et al., 1993)
P2	1:5000	WB	Santa Cruz sc-49304
PLP	1:5000	WB	(Jung et al., 1996)
PMP70	1:600	IHC	Abcam ab3421

Rab7	1:500	IHC	Sigma R4779
TAG-1	1:500	IHC	Prof. Elior Peles, PhD
TUJ1/ β -III Tubulin	1:500, 1:1000	IHC, WB	Covance MMS-435P

Secondary antibodies

α -rabbit-HRP	1:10000	WB	Dianova
α -mouse-HRP	1:10000	WB	Dianova
α -rabbit-Alexa488	1:2000	IHC	ThermoScientific A-21206
α -rabbit-Alexa555	1:2000	IHC	ThermoScientific A-31572
α -mouse-Alexa488	1:2000	IHC	ThermoScientific A-21202
α -mouse-Alexa555	1:2000	IHC	ThermoScientific A-31570
α -rat-Alexa488	1:2000	IHC	ThermoScientific A-21208
α -rat-Alexa594	1:2000	IHC	ThermoScientific A-21209
α -goat-Alexa488	1:2000	IHC	ThermoScientific A-11055
α -goat-Alexa555	1:2000	IHC	ThermoScientific A-21432
α -rabbit-Dyelight633	1:1000	IHC	Yo proteins 356

4.9 Dyes and marker

DAPI	Roche
GeneRuler 100 bp DNA ladder	Thermo Fisher Scientific
PageRuler™ Plus Prestained Protein Ladder	Thermo Fisher Scientific
Cholera Toxin Subunit B, Alexa Fluor® 555 conjugate	Thermo Fisher Scientific
α -Bungarotoxin, Alexa Fluor® 647 conjugate	Thermo Fisher Scientific

4.10 Primer

Genotyping PCR primer

Alds

7408:	3'-CCCTTCCTGCCACTTTCATC-5'
7409:	3'- TCTCAACCTGCCCCACCTCA-5'
1747:	3'- TCTCAACCTGCCCCACCTCA-5'

Cnce

1955: 3'-CATAGCCTGAAGAACGAGA-5'
2016: 3'-GCCTTCAAACGTCCATCTC-5'
7315: 3'-CCCAGCCCTTTTATTACCAC-5'

Pex5-loxp

2870: 3'-CGGGGAGTACGACAAGGCTGTGGACT-5'
2871: 3'-TCTGGTTCCCATTTGGCCAGGGTGGC-5'

Quantitative real-time PCR primer

β-actin

Forward: 5'-CTTCCTCCCTGGAGAAGAGC-3'
Reverse: 5'-ATGCCACAGGATTCCATACC-3'

Lamp1

Forward: 5'-CCTACGAGACTGCGAATGGT-3'
Reverse 5'-CCACAAGAACTGCCATTTTTC-3'

Limp2

Forward 5'-TGGAGATCCTAACGTTGACTTG-3'
Reverse 5'-GGCCAGATCCACGACAGT-3'

MAP1LC3A

Forward 5'-GACCAGCACCCCAGTAAGAT-3'
Reverse 5'-TGGGACCAGAACTTGGTCT-3'

Pex5

Forward: 5'-CACATCCGCTTCCTATGACA-3'
Reverse: 5'-AAAAGGCTGAGGGTGGTCA-3'

4.11 Mouse lines

Cnp-Cre::Pex5^{flox/flox} (Lappe-Siefke et al., 2003; Kassmann et al., 2011)

Abcd1^{-/-} (Forss-Petter et al., 1997)

5. Methods

5.1 Animals

All mice used in this study were bred and kept in individually ventilated cages under SPF conditions in the animal facility of the Max Planck Institute (MPI) for Experimental Medicine. All animal experiments were performed in compliance with animal policies of the State of Lower Saxony, Germany. Mice were sacrificed by cervical dislocation or by perfusion after deep anesthesia. Mice from both sex were analyzed for all experiments.

5.1.1 Tail digest and genotyping PCR

To evaluate the genotypes of mice, tail biopsies were taken from every animal at around P21 (after weaning). Tails were digested using the nexttec™ kit (Nexttec Biotechnology) according to manufacturer's instructions. Each tail was digested for 75 min on a shaker (1050 rpm) at 62°C. After equilibration of columns, 120 µl of tail digest were added and centrifuged for 1 min at 2158 rpm. Samples were eluted in 800 µl ddH₂O and stored at 4°C.

Pex5 loxP

1 µl	DNA (diluted 1:5)
0.5 µl	Primer (2870)
0.5 µl	Primer (2971)
2 µl	dNTP's (2 mM)
4 µl	Go-Taq buffer (5x)
0.1 µl	Go-Taq

ddH₂O was added to total of 21 µl.

PCR program:

95°C	3 min	
60°C	30 sec	} 35x
72°C	90 sec	
95°C	1 min	
60°C	1 min	

72°C 10 min
4°C break

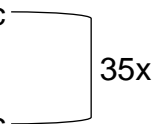
CNCE

1 µl DNA (diluted 1:5)
0.5 µl Primer (1955)
0.75 µl Primer (2016)
0.25 µl Primer (7315)
2 µl dNTP's (2 mM)
4 µl Go-Taq buffer (5x)
0.1 µl Go-Taq

ddH₂O was added to total of 21 µl.

PCR program:

95°C 3 min
50°C 30 sec
72°C 1 min
95°C 30 sec
50°C 1 min
72°C 10 min
4°C break

**ALDS**

1 µl DNA (diluted 1:5)
1 µl Primer (7408)
1 µl Primer (7409)
0.25 µl Primer (1747)
2.2 µl dNTP's (2 mM)
4.4 µl Go-Taq buffer (5x)
1.1 µl MgCl₂
1.1 µl Q
0.1 µl Go-Taq

ddH₂O was added to total of 21 µl.

PCR program:

95°C 3 min

56°C	30 sec	} 36x
72°C	1 min	
95°C	30 sec	
56°C	2 min	
72°C	10 min	
4°C	break	

To visualize DNA fragments under UV light, 5 µl of GelRed (1:40.000) was added to each PCR reaction. Samples were loaded to a 2% agarose gel. Gel electrophoresis was done in a running chamber filled with 1x TBE buffer for 90-120 min at 120 V.

5.2 Molecular biology

5.2.1 RNA isolation from sciatic nerves

RNA isolation was performed using the RNeasy Mini kit (Qiagen). Sciatic nerves were transferred into 2 ml Precelly's tubes filled with 500 µl QIAzol lysis reagent and 1.4 mm ceramic (zirconium oxide) beads. Homogenization was done via Precellys® 24 (10 sec at 5500 rpm, break on ice, 10 sec at 5500 rpm). After incubation at room temperature for 5 min, 100 µl of chloroform were added to nerve lysates and incubated for 2-3 min at room temperature. Lysates were centrifuged for 15 min at 13,000 rpm and supernatants were transferred to new tubes. One volume of 70% ethanol was added, directly mixed and applied to RNeasy columns. After centrifugation at 13,000 rpm for 15 s, 350 µl RW1 buffer were added and again centrifuged for 1 minute at 13,000 rpm. 80 µl of DNase-Mix were added and incubated for 15 minutes at room temperature. After another washing and centrifugation with RW1 buffer, columns were washed three times with 500 µl of RPE buffer. Finally, RNA was eluted with 30 µl of RNase-free ddH₂O. RNA quality and concentration was determined using the Agilent RNA 6000 Nano KIT and the Agilent 2100 Bioanalyzer according to company's instructions. Only samples with a RNA integrity number >8.5 were further used for cDNA synthesis.

5.2.2 Complementary single stranded DNA (cDNA) synthesis

To further analyze RNA expression, a complementary single stranded DNA (cDNA) library was generated from isolated RNA using a reverse transcriptase (SuperScript III, Thermo Fisher Scientific). First strand cDNA was synthesized at 55°C as follows:

2 µl	RNA (1 µg)
1 µl	dT mix Primer (0.6 pmol/µl)
1 µl	N9 (random nonamers 120 pmol/µl)

Samples were incubated at 70°C for 2 minutes and then put on ice.

The following mix was added to the reaction:

1.5 µl	ddH ₂ O
2 µl	5x first strand buffer
0.5 µl	dNTP (10 mM)
1 µl	DTT (100 mM)
1 µl	SuperScript III reverse transcriptase (200 U/µl)

The final 10µl reaction mixture was briefly spun down and incubated in a thermocycler (lid 65°C) with the following settings:

25°C	10 min
50°C	45 min
55°C	45 min

Synthesized cDNA was diluted with ddH₂O to a final concentration of 0.5 ng/µl.

5.2.3 Quantitative real-time PCR (qRT-PCR)

qRT-PCR was done using six biological replicates per genotype. SYBR[®] Green Master Mix (Applied Biosystems) was used according to the manufacturer's instructions to perform qRT-PCR. The mix contained:

4 µl	cDNA (0.5 ng/µl)
5 µl	SYBR [®] Green
0.1 µl	each primer (10 pmol/µl)
0.8 µl	ddH ₂ O

Reactions were performed in quadruplicates using the following PCR protocol:

50°C	120 s warm up
95°C	600 s melting
60°C	20 s annealing
72°C	30 s elongation and detection
95°C	10 s melting → back to step 3 → 45 cycles

Measurements were analyzed with the Applied Biosystems 7500 Fast Real-Time PCR System resulting in histograms of relative RNA abundance with respect to cyclophilinA (Ppia). Values were normalized to β -actin abundance using Microsoft Excel 2013. Quantification was done with GraphPad Prism 5, applying Student's t-test. Values were related to control values that were set to one.

5.2.4 Enzyme activity assay

Sciatic nerves were homogenized on ice in 150 μ l lysis buffer (1% Triton X-100, 50 mM Tris-HCl pH 7.5, 150 mM NaCl, 1% NP-40, with protease inhibitor (Complete, Roche) using Precellys® 24 (2 x 20 sec at 5000 rpm). Nerve lysates were centrifuged for 15 min at 12,000 rpm. Supernatants were incubated at 37°C with corresponding substrates (see table 4.4). Reactions were stopped with 500 μ l 0.4 M Glycine-NaOH (pH 10.4, adjusted with 1 M NaOH). After centrifugation at 13,000 rpm for 10 minutes, the supernatant was measured at 405 nm with an Eon microplate spectrophotometer (BioTek). In each experiment two technical replicates were measured. Student's T-test was applied to evaluate statistical significances.

5.2.5 Mass spectrometry

Sciatic nerves were homogenized in 200 μ l 0.29 M sucrose with complete Mini protease inhibitor (Roche Diagnostics GmbH) using the Precellys® 24 (10 sec at 5000 rpm, break on ice, 5 sec at 5500 rpm). Lysates were centrifuged at 4000 rpm for 10 minutes to remove cell nuclei. To separate samples into a cytosolic and a membranous fraction, lysates were centrifuged at 34,000 rpm for 1 h at 4 °C. The pellet (membranous fraction) was diluted in 50 μ l 1 X PBS. Both eluted pellet and supernatant

(cytosolic fraction) were stored at -80°C . Samples were sent for mass spectrometry to Dr. Britta Brügger (Biochemistry Center, Heidelberg). Experiments were performed with six biological replicates per genotype. Quantification was done in GraphPad Prism 5, applying Student's T-test.

5.3 Protein biochemistry

5.3.1 Sample preparation

Sciatic nerves were dissected and frozen on either dry ice or in liquid nitrogen. Nerves were stored at -80°C . Frozen nerves were transferred into 2 ml tubes filled with 200 μl RIPA buffer and 1.4 mm ceramic (zirconium oxide) beads. Homogenization was done via Precellys® 24 (10 sec at 5000 rpm, break on ice, 5 sec at 5500 rpm). Nerve lysates were centrifuged for 10 min at 4000 rpm to remove cell nuclei. Supernatants were used for protein biochemistry.

5.3.2 Lowry protein assay

The Bio-Rad DC Protein Assay kit was used according to the Lowry method to measure protein concentrations. 5 μl of samples were pipetted in a 96-well plate into 25 μl of solution A. After submission of 200 μl of solution B, the reaction was incubated for 15 min at RT. Standards with defined protein concentrations were used to calculate sample concentrations. Absorbance was measured at 650 nm with an Eon microplate spectrophotometer (BioTek).

5.3.3 Protein separation using SDS-PAGE

SDS-polyacrylamide gels with an acrylamide concentration of 10 or 15% (for myelin proteins) and a thickness of 1.5 mm were prepared using the Bio-rad system. The separating gel was filled into the gel cassettes and covered with isopropanol to prevent air bubbles. The isopropanol was carefully removed after 1h polymerization and the stacking gel was added. After inserting a 10 well comb the gel was polymerized for another 30-60 min at RT. Gels were either directly used or stored in wet tissues for up

to 3 days at 4°C. Nerve lysates were diluted in 2x SDS sample buffer, containing 5% 2-Mercaptoethanol to break down disulfide bonds. After incubation on a thermo shaker for 10 min at 40°C, appropriate amounts of samples, as well as 5 µl of the marker (PageRuler™ Plus Prestained Protein Ladder), were loaded on the gel. The Mini-Protean 3 system (BIO-RAD) was used to separate proteins according to their size by SDS-polyacrylamide gel electrophoresis (SDS-PAGE). The chamber and gels were assembled according to the manufacturer's instructions and filled with 1 X SDS running buffer. The gel was run at 80 V and 40-50 mA for approximately 10 min and voltage was then increased to 120 V and 60-70 mA at RT for 1-2 h.

5.3.4 Western blotting

Transfer of proteins from the SDS gel to a polyvinylidene difluoride membrane (Hybond P, Amersham Biosciences, pore size 0.45 µm) was done using a semi-dry (Novex® Semi-Dry Blotter, Thermo Fisher Scientific) or wet blotting system. Therefore, membranes were activated for 1 min in 100% methanol, washed briefly in ddH₂O, and kept in transfer buffer until blotting. Blotting was done for approximately 70 min at RT applying a constant voltage of approximately 30-40 V and a current of 250 mA. Membranes were blocked with 5% milk powder in TBST (0.05% Tween-20 in TBS) at room temperature for 1 h. Primary antibodies (4.8), diluted in blocking solution, were incubated overnight at 4°C. HRP-conjugated secondary antibodies (see 4.8, 1:5000) were incubated for 1h at room temperature after three times washing for 15 min each in TBS-T (0.1% Tween-20 in TBS). Membranes were again washed three times in TBS-T. 2 ml of Western-Lighting Plus-ECL Reagent (PerkinElmer) were applied for 1 min. Chemiluminescence was detected by scanning the membranes for 15 min with the Intas ChemoCam Imager. Signals were normalized to loading controls and analyzed using Fiji software. Protein abundance of control animals were set to 1 and mutant values were displayed as relative protein amounts.

5.4 Fluorescence microscopy

5.4.1 Teased fiber preparation

Sciatic nerves were dissected and directly transferred into 1x PBS. The epineurium was removed with fine forceps (Dumont #5) under a binocular and each nerve was pre-teased into 10 equal fiber bundles. Each bundle was transferred onto a glass slide and teased into single axons. Finally, the slides were dried at room temperature and stored at -20°C.

5.4.2 Immunofluorescence of teased fibers

Slides were directly taken from -20°C and fixed for 5 min with 4% PFA at room temperature and then incubated for 3-5 min in methanol at -20°C. After three times washing in 1x PBS, samples were incubated for 1 h at room temperature in 10% horse serum in 0.05% Triton X-100 to block unspecific bindings. Slides were incubated with primary antibodies (diluted in blocking solution, see 4.8) at 4°C overnight or for 90 minutes at room temperature. After washing in PBS, secondary antibodies (diluted in blocking solution) and DAPI (1:10,000), were incubated for 1h at room temperature. After washing in PBS and H₂O, the slides were mounted with ProLong®Gold or Aqua Poly Mount and stored at 4°C. Fluorescence light microscopy was done with the Axio Observer (Zeiss) equipped with an AxioCam MRm (Zeiss). Images were processed with the Zen 2012 software (Zeiss). The number of Schmidt-Lanterman incisures and the localization of Kv1.1 clusters was analyzed and quantified using Fiji (Schindelin et al., 2012) and GraphPad Prism 5.

5.4.3 *Ex vivo* fluorescent staining of gangliosides

Sciatic nerves were dissected and pre-teased in oxygenated artificial cerebrospinal fluid (ACSF) solution. Monoclonal anti-ganglioside antibodies specific for GM1 and GD1a (kindly provided by R. McGonigal and H. Willison) or CTB were diluted in ACSF and incubated at room temperature for 1.5 h. After three times washing in ACSF solution, samples were incubated with isotype-specific fluorescent secondary antibodies (Alexa-488 IGg3 and IG2b goat anti-mouse, Life Technologies). After washing, samples were fixed in 4% PFA for 5 min at room temperature. After

consecutive washing in 1x PBS and 0.1 M glycine, fibers were teased on glass slides, dried and finally stored at -20°C. Slides were treated according the teased fiber protocol for co-labeling. For quantification of GDa1 colocalization with LAMP1, about 10% of total nerve material was analyzed from three (controls) or five (conditional mutants) independent 9 months old animals. The number of GDa1-positive vesicles that were bigger than 1 µm and colocalized with LAMP1 was quantified and statistically analyzed by Student's T-test using GraphPad Prism 5.

5.4.4 Immunofluorescence of cryo sections

Gastrocnemius muscles were dissected and were fixed overnight in 4 % PFA at 4°C. For dehydration, muscles were transferred to 10% glucose overnight and then incubated in 30% sucrose for approximately 6 h. Muscles were mounted in Tissue-Tek® O.C.T. Compound media and stored at -20°C. Cryo sections (40 µm) were obtained with cryostat (Leica Jung Cryocut CM3000). Sections were washed for 30 min in 1x PBS and then permeabilized in precooled 95% methanol with 5% acetone for 15 min at -20°C. Sections were washed in 1x PBS (3 x 5 min) and were then permeabilized in cryofix (7 ml Polyethylenglycol, 50 ml 100% Ethanol in 47 ml ddH₂O) for 7 min at room temperature. After another washing in 1x PBS, unspecific bindings were blocked (0.5% BSA, 1% horse serum, 0.25% Triton X-100) for 30 min. Slides were consecutively washed in 1x PBS (3 x 10 min), followed by 15 min 0.5% BSA in 1 % horse serum. α-Bungarotoxin was diluted in 0.5% BSA and 1 % horse serum in DAPI solution (1:10.000) and were applied for 1.5 h. After washing in 1 x PBS and distilled water, slides were mounted with AquaPolymount and imaged with the Axio Observer. Z1 (Zeiss) equipped with an AxioCam MRm (Zeiss). Images were processed with the Zen 2012 software (Zeiss) and the number of neuromuscular junctions (NMJs) per mm² was counted with Fiji and quantified with GraphPad Prism5.

5.5 Histology

5.5.1 Perfusion and paraffin embedding

Mice were intraperitoneally anesthetized with 0.2 ml/ 10 g avertin and intracardially perfused with 50 ml HBSS, containing 750 µl EDTA (0.5 M). Fixation with 4% PFA, was performed for approximately 15 minutes. Sciatic nerves were dissected and post-fixed in 4% PFA for 2 h and in 1% PFA o/n at 4°C. Fixed nerves were washed in 1X PBS and transferred to tissue cassettes. For paraffin embedding, the paraplast embedding station was used with the following program:

50% Ethanol	1 h
70% Ethanol	2x 2 h
96% Ethanol	2x 2 h
100% Ethanol	2x 2 h
Isopropanol	1 h
Xylol	2x 2 h
Paraffin	2x 2 h

Subsequently, nerves were transferred to metal forms and casted in blocks with 60°C warm paraffin. Paraffin blocks were cooled to dry and stored at RT. Nerves were cut in 10 µm thick sections using the microtome (HM 400, MICROM) and dried at RT.

5.5.2 DAB staining of paraffin sections

Paraffin sections were deparaffinized by the following steps:

60°C	10 min
Xylol	2x 10 min
Xylol/Isopropanol (1:1)	10 min
100% Ethanol	5 min
90% Ethanol	5 min
70% Ethanol	5 min
50% Ethanol	5 min
ddH ₂ O	5 min

For MAC-3 and CD3 staining, deparaffinized sections were incubated and cooked in TE buffer (650 watts, 10 min). Samples were cooled for about 20 min and then 5 min incubated in Tris buffer containing 2% milk powder. Shandon coverplates (Thermo Fisher Scientific) were used for even distribution of solutions. Slides were rinsed again with Tris buffer containing 2% milk powder and then blocked for 10 min in inactivated goat serum (1:5). Slides were again washed with Tris buffer containing 2% milk powder. Slides were incubated with the α -rat-biotinylated antibody (1:100) for 30 min. Subsequently, the Vector Elite ABC Kit (Vector Labs) was incubated for 30 min. After removal of coverplates, slides were washed with Tris buffer without milk-powder and the HRP substrate 3, 3'-Diaminobenzidine (DAB) was applied for 10 min by using the DAB Zytomed Kit (Zytomed Systems GmbH). Antibody binding was apparent by brown labeling. After washing with ddH₂O, blue nuclear staining was achieved by 5 min incubation with 0.1% Haematoxylin. Samples were consecutively rinsed with ddH₂O, HCl-Alcohol for 5-10 sec, Scott's solution for 5 min and finally ddH₂O. Sections were dehydrated by an increasing alcohol gradient (50%, 70%, 90%, and 100% for 5 min each) followed by Xylol/Isopropanol (1:1, 5 min) and two times Xylol (5 min). Finally, sections were mounted using Eukitt.

5.6 Immuno-electron microscopy

5.6.1 Perfusion and tissue preparation

Mice were intraperitoneally anesthetized with 0.2 ml/ 10 g avertin and intracardially perfused with 50 ml HBSS, containing 750 μ l EDTA (0.5 M). Fixation with Karlsson-Schultz (Schultz and Karlsson, 1965), containing 0.25% glutaraldehyde, was performed for approximately 15 minutes. Sciatic nerves were dissected and post-fixed in 4% PFA for 2 h. Dissected nerves were stored in 1% PFA at 4°C. For dehydration, nerves were incubated on a rotator in 2.3 M sucrose at 4°C overnight. Finally, nerves were trimmed into small fractions, were put on degreased aluminum pins and stored in liquid nitrogen.

5.6.2 Preparation of ultrathin cryo sections

Ultrathin cryo sections were obtained according to the “Tokuyasu technique” (Tokuyasu, 1973). Sciatic nerves were trimmed such that surface of around 230x350 μm was obtained. A diamond knife (Diatome) was used to obtain longitudinal ultrathin section (50 nm) at -120°C in an Ultracut S ultramicrotome (Leica). Sections were picked up with a loop containing a small drop of sucrose solution (2.3 M sucrose, 2% methylcellulose in H_2O) and transferred onto formvar film-coated and carbon-stabilized copper grids. Grids were stored at 4°C .

5.6.3 Immunolabeling of ultrathin cryo sections

Staining was performed at RT on parafilm stripes according to the “Tokuyasu technique” (Tokuyasu, 1973). To remove the pick-up-solution, grids were first washed in PBS (3 x 2 min) and then treated with 0.1% glycine in PBS (3 x 2 min). After 3 minutes blocking with 1% BSA in PBS, samples were incubated for 1 h with an anti-LAMP1 antibody (mk, rat; 1:200). Grids were washed in PBS (5 x 2 min) and then incubated for 30 min with a species-specific secondary rabbit antibody (1:200). After washing in 0.1 % BSA in PBS, sections were incubated with protein-A-gold (1:60 in blocking solution, 10 nm) for 20 min. After another washing with PBS, antibodies were fixed for 5 min with 1% glutaraldehyde in PBS. Grids were cleared of phosphates by repetitive washing (10 x 1min) with distilled water. Samples were treated on ice with neutral uranylacetate and methylcellulose-uranylacetate for 5 min each to contrast and embed sections. Eventually, grids were picked up with a loop, dried and stored at 4°C . Sections were examined with a LEO EM 912AB electron microscope (Zeiss) equipped with an on-axis 2048 X 2048 CCD camera (Proscan).

5.7 Electron microscopy

5.7.1 Perfusion and epon embedding

Mice were intraperitoneally anesthetized, intracardially perfused and fixed with Karlsson-Schultz (Schultz and Karlsson, 1965). Sciatic nerves were dissected and post-fixed in 4% PFA for 2 h. Dissected nerves were stored in 1% PFA at 4°C . Epon

embedding was done with an automated system (EMTP, Leica) using the following protocol:

Phosphate buffer	3 x 10 min	4°C
2% OsO ₄	4 hours	
ddH ₂ O	3 x 10 min	
30% Ethanol	20 min	
50% Ethanol	20 min	
70% Ethanol	20 min	
90% Ethanol	20 min	
100% Ethanol	4 x 10 min	
Propylenoxid	3 x 10 min	RT
Propylenoxid/Epon 2:1	2 hours	
Propylenoxid/Epon 1:1	2 hours	
Propylenoxid/Epon 1:2	4 hours	
Epon	4 hours	

Samples were then polymerized o/n at 60°C.

5.7.2 Preparation of semi- and ultra-thin sections

Semi-thin (500 nm) and ultra-thin (50 nm) cross sections of epon embedded sciatic nerves were obtained with a Ultracut S microtome (Leica) equipped with an Ultra 45° diamond knife (Diatome). Semi-thin sections were transferred to glass slide and dried on a hot plate (60°C). Ultra-thin sections were placed on formvar polyvinyl-coated copper grids.

5.7.3 Staining of semi-thin sections and quantification of axon number

Semi-thin sections were incubated with methylene blue/ azure II for approximately 1 min on a 60°C hot plate to visualize myelin sheaths. After washing with ddH₂O, slides were dried and mounted with Eukitt. Samples were imaged with the Zeiss Axiophot using a Plan NEOFLUAR 100x/1.30 oil objective (Zeiss). Total number of axons per

nerve was counted from 2 individual sections of at least three animals per group using Fiji. Axon distribution was quantified using GraphPad Prism5.

5.7.4 Contrasting of ultra-thin sections

Grids were incubated for 30 min with 4% uranyl acetate (protected from light), washed 3 times for 1 min in ddH₂O and the incubated for 6 min with Reynolds lead citrate. After 4 times washing with ddH₂O, grids were carefully dried using filter papers.

5.7.5 Electron microscopy and g-ratio analysis

Images of ultra-thin sections were obtained with the Zeiss EM900 (Zeiss) and digital equipped with a wide-angle dual speed 2K-CCD-Camera (TRS). Myelin thickness was evaluated by g-ratio analysis (dividing the axonal by the fiber diameter) using Fiji software. Results derived from at least 100 randomly chosen fibers per nerve. Quantification was done using Microsoft Excel 2013 and GraphPad Prism 5 applying Student's T-test.

5.8 Electrophysiology

Sciatic nerves were dissected and transferred into a perfusion chamber filled with ACSF (pH of 7.4) and continuous gassing (95% O₂, 5% CO₂). The length of nerve was measured and placed into suction electrodes for stimulation and recording. Electrophysiological measurements were performed by Jenniffer Günther. After an adaptation of approximately 30 minutes, electrical stimulation was performed at different intensities (0.13 mA - 0.3 mA). The stimulus intensities were increased manually in step-width of 0.05 mA, with inter-stimulus intervals of 3 seconds. Each stimulus intensity was used 10 times, while compound action potentials (CAP) were continuously measured. Recorded signals were acquired at 100 kHz, amplified x100 by Ext-2F (NPI Electronic), and a further 50-fold by SR560 (Stanford Research Systems), and filtered. Patchmaster software equipped with an EPC9 amplifier interface (HEKA) was used to control recordings. Stimulus intensities were altered

using Stimulus Isolator A385 (World Precision Instruments). Data analysis was done by Dr. Livia de Hoz. Each nerve was analyzed separately using Matlab by averaging same stimulus repetitions. Nerve conduction velocity was calculated for each stimulus intensity as the mean across trials of the ratio between the length of the nerve and the time between peaks of stimulus-artifact (first small positive peak) and response (3rd positive peak).

5.9 Behavior

5.9.1 Grid test

Mice were put on a metal grid (49.5 x 15 x 13 cm) with a distance of 1 x 2 cm between single rods. Animals had to run a distance of 1.5 m and their slips were counted. Mice were habituated to the device before they were tested on 3 consecutive days. This test was used to evaluate motor performance and coordination. Values were analyzed with Student's T-test.

5.9.2 Grip strength

This test was used to evaluate muscle strength. Therefore, animals had to grasp a grid, connected to a sensor measuring the force, with their forelimbs. The mice were gently pulled horizontally by their tail. Thereby, the maximal grip strength was measured by the device. This procedure was consecutively repeated seven times per animal

5.9.3 Elevated beam

This test was used to assess motor coordination and balance. Mice have to walk across an elevated narrow beam (1 m length) to reach a safe and light protected box. Mice were trained and then tested three times on one day. Their performance was evaluated by the number of hind limb slips they made and the time they needed to reach the box.

5.9.4 Dynamic plantar aesthesiometer

The dynamic plantar aesthesiometer (ugo basile) was used to investigate the mechanical sensitivity threshold. Therefore, animals were put on a grid, each surrounded by plastic side glass enclosures. After a habituation period of about 1 h, the mechanical sensitivity threshold of hind paws was determined by the use of electronic von Frey filaments. This filament automatically recorded through a blunt probe the maximum vertical contact force (in grams) when mice lifted their hind paw. Each measurement was carried out 5 times per hind paw. A cut-off in the amount of 30 grams prevents injuries of the hind paws.

5.9.5 Plantar Hargreaves Test

The plantar Hargreaves test (ugo basil) was used to determine the thermal sensitivity threshold. For this purpose, mice are sitting on an acrylic glass bottom each surrounded by plastic side glass enclosures. Mice were habituated for about an hour before the measurements started. The threshold determination was made by the use of an electronic punctual infrared heat source that is positioned underneath the hind paw. The device automatically determined the time needed until the animal lifts the paw. Each measurement was performed 5 times per hind paw. A cut-off infrared intensity of 99 units ($380 \text{ mW} / \text{cm}^2 / \text{sec}$) prevents injuries on the hind paws.

References

- Adamo AM, Aloise PA, Pasouini JM (1986) A possible relationship between concentration of microperoxisomes and myelination. *Int J Dev Neurosci* 4:513–517.
- Ahlemeyer B, Neubert I, Kovacs WJ, Baumgart-Vogt E (2007) Differential expression of peroxisomal matrix and membrane proteins during postnatal development of mouse brain. *J Comp Neurol* 505:1–17.
- Alberts B, Johnson A, Lewis J, Raff M, Roberts K, Walter P (2002) *Molecular Biology of the Cell; Peroxisomes*. 4th edition. New York: Garland Science.
- Amor S, Puentes F, Baker D, van der Valk P (2010) Inflammation in neurodegenerative diseases. *Immunology* 129:154–169.
- Ando S, Tanaka Y, Ono YT, Kon K (2003) Turnover of Myelin Lipids in Aging Brain. *Neurochem Res* 28:5–13.
- Arancibia-Carcamo IL, Attwell D (2014) The node of Ranvier in CNS pathology. *Acta Neuropathol* 128:161–175 Available at: <http://link.springer.com/10.1007/s00401-014-1305-z>.
- Archelos JJ, Roggenbuck K, Scheider-Schaulies J, Linington C, Toyka KV, Hartung HP (1993) Production and characterization of monoclonal antibodies to the extracellular domain of P0. *J Neurosci Res* 35:46–53.
- Arroyo EJ, Scherer SS (2000) On the molecular architecture of myelinated fibers. *Histochem Cell Biol* 113:1–18.
- Arroyo EJ, Sirkowski EE, Chitale R, Scherer SS (2004) Acute demyelination disrupts the molecular organization of peripheral nervous system nodes. *J Comp Neurol* 479:424–434.
- Baarine M, Ragot K, Athias A, Nury T, Kattan Z, Genin EC, Andreoletti P, Ménétrier F, Riedinger J-M, Bardou M, Lizard G (2012) Incidence of Abcd1 level on the induction of cell death and organelle dysfunctions triggered by very long chain fatty acids and TNF- α on oligodendrocytes and astrocytes. *Neurotoxicology* 33:212–228.
- Baes M, van Veldhoven PP (2012) Mouse models for peroxisome biogenesis defects and β -oxidation enzyme deficiencies. *Biochim Biophys Acta* 1822:1489–1500.
- Bagchi B, Al-Sabi A, Kaza S, Scholz D, O'Leary VB, Dolly JO, Ovsepian SV (2014) Disruption of Myelin Leads to Ectopic Expression of KV1.1 Channels with Abnormal Conductivity of Optic Nerve Axons in a Cuprizone-Induced Model of Demyelination. *PLoS ONE* 9:e87736.
- Balice-Gordon RJ, Bone LJ, Scherer SS (1998) Functional Gap Junctions in the Schwann Cell Myelin Sheath. *J Cell Biol* 142:1095–1104.
- Ballabio A, Ballabio A, Ballabio A, Ballabio A, Ballabio A (2009) Lysosomal disorders: From storage to cellular damage. *Biochim Biophys Acta* 1793:684–696.

- Barry DS, O’Keeffe GW, Barry DS, O’Keeffe GW, Barry DS, Barry DS, Barry DS (2013) Peroxisomes: The neuropathological consequences of peroxisomal dysfunction in the developing brain. *Int J Biochem Cell Biol* 45:2012–2015.
- Berger J, Forss-Petter S, Eichler FS (2014) Pathophysiology of X-linked adrenoleukodystrophy. *Biochimie* 98:135–142.
- Berger J, Gärtner J (2006) X-linked adrenoleukodystrophy: Clinical, biochemical and pathogenetic aspects. *Biochim Biophys Acta* 1763:1721–1732.
- Beyenbach KW, Wieczorek H (2006) The V-type H⁺ ATPase: molecular structure and function, physiological roles and regulation. *J Exp Biol* 209:577–589.
- Bezman L, Moser HW (1998) Incidence of X-linked adrenoleukodystrophy and the relative frequency of its phenotypes. *Am J Med Genet* 76:415–419.
- Bhat MA, Rios JC, Lu Y, Garcia-Fresco GP, Ching W, Martin MS, Li J, Einheber S, Chester M, Rosenbluth J, Salzer JL, Bellen HJ (2001) Axon-Glia Interactions and the Domain Organization of Myelinated Axons Requires Neurexin IV/Caspr/Paranodin. *Neuron* 30:369–383.
- Bizzozero OA, Zuñiga G, MB Lees (1991) Fatty Acid Composition of Human Myelin Proteolipid Protein in Peroxisomal Disorders. *J Neurochem* 56:872.
- Bottelbergs A, Verheijden S, Hulshagen L, Gutmann DH, Goebbels S, Nave K-A, Kassmann CM, Baes M (2010) Axonal integrity in the absence of functional peroxisomes from projection neurons and astrocytes. *Glia* 58:1532–1543.
- Bottelbergs A, Verheijden S, Just W, Van Veldhoven PP, Devos R, Baes M (2012) Peroxisome deficiency but not the defect in ether lipid synthesis causes activation of the innate immune system and axonal loss in the central nervous system. *J Neuroinflammation* 9:1–21.
- Bowen P, Lee CS, Zellweger H, Lindenberg R (1964) A familial syndrome of multiple congenital defects. *Bull Johns Hopkins Hosp* 114:402–414.
- Boyle MET, Berglund EO, Murai KK, Weber L, Peles E, Ranscht B (2001) Contactin Orchestrates Assembly of the Septate-like Junctions at the Paranode in Myelinated Peripheral Nerve. *Neuron* 30:385–397.
- Braulke T, Bonifacino JS (2009) Sorting of lysosomal proteins. *Biochim Biophys Acta* 1793:605-614.
- Braverman NE, Moser AB (2012) Functions of plasmalogen lipids in health and disease. *Biochim Biophys Acta* 1822:1442–1452.
- Bremer J, Norum KR (1982) Metabolism of very long-chain monounsaturated fatty acids (22:1) and the adaptation to their presence in the diet. *J Lipid Res* 23:243–256.
- Brinkmann BG, Agarwal A, Sereda MW, Garratt AN, Müller T, Wende H, Stassart RM, Nawaz S, Humml C, Velanac V, Radyushkin K, Goebbels S, Fischer TM, Franklin RJ, Lai C, Ehrenreich H, Birchmeier C, Schwab MH, Nave KA (2008) Neuregulin-1/ErbB Signaling Serves Distinct Functions in Myelination of the Peripheral and Central Nervous System. *Neuron* 59:581–595.

- Brites P, Mooyer PAW, Mrabet el L, Waterham HR, Wanders RJA (2008) Plasmalogens participate in very-long-chain fatty acid-induced pathology. *Brain* 132:482–492.
- Brites P, Waterham HR, Wanders RJA (2004) Functions and biosynthesis of plasmalogens in health and disease. *Biochim Biophys Acta* 1636:219–231.
- Clague MJ (1998) Molecular aspects of the endocytic pathway. *Biochem J* 336:271–282.
- Caldwell JH, Schaller KL, Lasher RS, Peles E, Levinson SR (2000) Sodium channel Nav1.6 is localized at nodes of Ranvier, dendrites, and synapses. *PNAS* 97:5616–5620.
- Chen C-S, Patterson MC, O'Brien JF, Pagano RE, Wheatley CL (1999) Broad screening test for sphingolipid-storage diseases. *Lancet* 354:901–905.
- Chi XX, Nicol GD (2007) Manipulation of the Potassium Channel Kv1.1 and Its Effect on Neuronal Excitability in Rat Sensory Neurons. *J Neurophysiol* 98:2683–2692.
- Chu B-B, Liao Y-C, Qi W, Xie C, Ximing du, Wang J, Yang H, Miao H-H, Li B-L, Song B-L (2015) Cholesterol Transport through Lysosome-Peroxisome Membrane Contacts. *Cell* 161:291–306.
- Cifuentes-Diaz C, Chareyre F, Garcia M, Devaux J, Carnaud M, Levasseur G, Niwa-Kawakita M, Harroch S, Girault J-A, Giovannini M, Goutebroze L (2011) Protein 4.1B Contributes to the Organization of Peripheral Myelinated Axons Chédotal A, ed. *PLoS ONE* 6:1–15.
- Collins BE, Yang LJ-S, Mukhopadhyay G, Filbin MT, Kiso M, Hasegawa A, Schnaar RL (1997) Sialic Acid Specificity of Myelin-associated Glycoprotein Binding. *J Biol Chem* 272:1248–1255.
- Davis JQ, Lambert S, Bennett V (1996) Molecular composition of the node of Ranvier: identification of ankyrin-binding cell adhesion molecules neurofascin (mucin+/third FNIII domain-) and NrCAM at Nodal Axon Segments. *J Cell Biol* 135:1355–1367.
- De Chaves E P, Sipione S (2010) Sphingolipids and gangliosides of the nervous system in membrane function and dysfunction. *FEBS Lett* 584:1748-1759.
- De Duve C, Baudhuin P (1966) Peroxisomes (microbodies and related particles). *Physiol Rev* 46:323–357.
- Devaux JJ, Kleopa KA, Cooper EC, Scherer SS (2004) KCNQ2 Is a Nodal K⁺ Channel. *J Neurosci* 24:1236–1244.
- Dupree JL, Coetzee T, Suzuki K, Popko B (1998) Myelin abnormalities in mice deficient in galactocerebroside and sulfatide. *J Neurocyt* 27:649–659.
- Dupree JL, Girault J-A, Popko B (1999) Axo-glial Interactions Regulate the Localization of Axonal Paranodal Proteins. *J Cell Biol* 147:1–7.
- Einheber S, Zanazzi G, Ching W, Scherer S, Milner TA, Peles E, Salzer JL (1997) The Axonal Membrane Protein Caspr, a Homologue of Neurexin IV, Is a Component of the

- Septate-like Paranodal Junctions That Assemble during Myelination. *J Cell Biol* 139:1495–1506.
- Engelen M, Kemp S, de Visser M, van Geel BM, Wanders RJ, Aubourg P, Poll-The B (2012) X-linked adrenoleukodystrophy (X-ALD): clinical presentation and guidelines for diagnosis, follow-up and management. *J Rare Dis* 7:51.
- Eshed Y, Feinberg K, Poliak S, Sabanay H, Sarig-Nadir O, Spiegel I, Bermingham JR Jr., Peles E (2005) Gliomedin Mediates Schwann Cell-Axon Interaction and the Molecular Assembly of the Nodes of Ranvier. *Neuron* 47:215–229.
- Faivre-Sarrailh C, Devaux JJ (2013) Neuro-glial interactions at the nodes of Ranvier: implication in health and diseases. *Front Cell Neurosci* 7:1–13.
- Fang Y, Morrell JC, Jones JM, Gould SJ (2004) PEX3 functions as a PEX19 docking factor in the import of class I peroxisomal membrane proteins. *J Cell Biol* 164:863–875.
- Fannon AM, Sherman DL, Ilyina-Gragerova G, Brophy PJ, Friedrich VL Jr, Colman DR (1995) Novel E-cadherin-mediated adhesion in peripheral nerve: Schwann cell architecture is stabilized by autotypic adherens junctions. *J Cell Biol* 129:189–202.
- Faust PL, Kaye EM, Powers JM (2010) Myelin lesions associated with lysosomal and peroxisomal disorders. *Rev Neurother* 10:1449–1466.
- Ferguson B, Matyszak MK, Esiri MM, Perry VH (1997) Axonal damage in acute multiple sclerosis lesions. *Brain* 120:393–399.
- Ferrer I, Aubourg P, Pujol A (2010) General Aspects and Neuropathology of X-Linked Adrenoleukodystrophy. *Brain Pathol* 20:817–830.
- Forss-Petter S, Werner H, Berger J, Lassmann H, Molzer B, Schwab MH, Bernheimer H, Zimmermann F, Nave K-A (1997) Targeted inactivation of the X-linked adrenoleukodystrophy gene in mice. *Journal of Neuroscience Research* 50:829–843.
- Fourcade S, Lopez-Erauskin J, Galino J, Duval C, Naudi A, Jove M, Kemp S, Villarroja F, Ferrer I, Pamplona R, Portero-Otin M, Pujol A (2008) Early oxidative damage underlying neurodegeneration in X-adrenoleukodystrophy. *Hum Mol Genet* 17:1762–1773.
- Fransen M, Nordgren M, Wang B, Apanasets O (2012) Role of peroxisomes in ROS/RNS-metabolism: Implications for human disease. *Biochim Biophys Acta* 1822:1363–1373.
- Fünfschilling U et al. (2012) Glycolytic oligodendrocytes maintain myelin and long-term axonal integrity. *Nature* 485:517–521.
- Galea E, Launay N, Portero-Otin M, Ruiz M, Pamplona R, Aubourg P, Ferrer I, Pujol (2012) Oxidative stress underlying axonal degeneration in adrenoleukodystrophy: A paradigm for multifactorial neurodegenerative diseases?. *Biochim Biophys Acta* 1822:1475–1488.
- Garbay B, Heape AM, Sargueil F, Cassagne C (2000) Myelin synthesis in the peripheral nervous system. *Prog Neurobiol* 61:267–304.

- Garbern JY, Yool DA, Moore GJ, Wilds IB, Faulk MW, Klugmann M, Nave KA, Siermans EA, van der Knaap MS, Bird TD, Shy ME, Kamholz JA, Griffiths IR (2002) Patients lacking the major CNS myelin protein, proteolipid protein 1, develop length-dependent axonal degeneration in the absence of demyelination and inflammation. *Brain* 125:551–561.
- Garratt AN, Voiculescu O, Topilko P, Charnay P, Birchmeier C (2000) A Dual Role of erbB2 in Myelination and in Expansion of the Schwann Cell Precursor Pool. *J Cell Biol* 148:1035.
- Gatzinsky KP, Berthold CH (1990) Lysosomal activity at nodes of Ranvier during retrograde axonal transport of horseradish peroxidase in alpha-motor neurons of the cat. *J Neurocyt* 19:989–1002.
- Gatzinsky KP, Persson GH, Berthold CH (1997) Removal of retrogradely transported material from rat lumbosacral alpha-motor axons by paranodal axon-schwann cell networks. *Glia* 20:115–126.
- Ghabriel MN, Allt G (1979) The role of Schmidt-Lanterman incisures in Wallerian degeneration. *Acta Neuropathol* 48:83–93.
- Ghabriel MN, Allt G (1981) Incisures of Schmidt-Lanterman. *Progr Neurobiol* 17:25–58.
- Ghaedi K, Tamura S, Okumoto K, Matsuzono Y, Fujiki Y (2000) The Peroxin Pex3p Initiates Membrane Assembly in Peroxisome Biogenesis. *Mol Biol Cell* 11:2085–2102.
- Ghosh A, Manrique-Hoyos N, Voigt A, Kreutzfeldt M, Merkler D, Simons M (2011) Targeted Ablation of Oligodendrocytes Triggers Axonal Damage. *PLoS ONE* 6:e22735.
- Ghosh P, Dahms NM, Kornfeld S (2003) Mannose 6-phosphate receptors: new twists in the tale. *Nat Rev Mol Cell Biol* 4:202–212.
- Giese KP, Martini R, Lemke G, Soriano P, Schachner M (1992) Mouse P0 gene disruption leads to hypomyelination, abnormal expression of recognition molecules, and degeneration of myelin and axons. *Cell* 71:565–576.
- Goldman BM, Blobel G (1978) Biogenesis of peroxisomes: intracellular site of synthesis of catalase and uricase. *PNAS* 75:5066–5070.
- Gomez-Sanchez JA, Carty L, Iruarrizaga-Lejarreta M, Palomo-Irigoyen M, Marta Varela-Rey M, Griffith M, Hantke J, Macias-Camara N, Azkargorta M, Aurrekoetxea I, Gutiérrez De Juan V, Jefferies HBJ, Aspichueta P, Elortza F, Aransay AM, Martínez-Chantar ML, Baas F, Mato JM, Mirsky R, Woodhoo A, Jessen KR (2015) Schwann cell autophagy, myelinophagy, initiates myelin clearance from injured nerves. *J Cell Biol* 210:153–168.
- Gorgas K, Teigler A, Komljenovic D, Just WW (2006) The ether lipid-deficient mouse: Tracking down plasmalogen functions. *Biochim Biophys Acta* 1763:1511–1526.
- Gould RM, Byrd AL, Barbarese E (1995) The number of Schmidt-Lanterman incisures is more than doubled in shiverer PNS myelin sheaths. *J Neurocyt* 24:85–98.

- Gould SG, Keller GA, Subramani S (1987) Identification of a peroxisomal targeting signal at the carboxy terminus of firefly luciferase. *J Cell Biol* 105:2923–2931.
- Gould SJ, Valle D (2000) Peroxisome biogenesis disorders: Genetics and cell biology. *Genet* 16:340–345.
- Grant BD, Donaldson JG (2009) Pathways and mechanisms of endocytic recycling. *Nat Rev Mol Cell Biol* 10:597–608.
- Greenfield S, Brostoff S, Eylar EH, Morell P (1973) Protein composition of myelin of the peripheral nervous system. *J Neurochem* 20:1207–1216.
- Griffin JW, Thompson WJ (2008) Biology and pathology of nonmyelinating Schwann cells. *Glia* 56:1518–1531.
- Griffiths G, Simons K (1986) The trans Golgi network: sorting at the exit site of the Golgi complex. *Science* 234:438–443.
- Griffiths I (2011) Axonal Swellings and Degeneration in Mice Lacking the Major Proteolipid of Myelin. *Science* 280:1610–1613.
- Hall SM, Williams PL (1970) Studies on the “Incisures” of Schmidt and Lanterman. *J Cell Sci* 6:767–791.
- Hanson MG, Fregoso VL, Vrana JD, Tucker CL, Niswander LA, Hanson MG, Fregoso VL, Vrana JD, Tucker CL, Niswander LA (2014) Peripheral nervous system defects in a mouse model for peroxisomal biogenesis disorders. *Dev Biol* 395:84–95.
- Hao J, Padilla F, Dandonneau M, Lavebratt C, Lesage F, Noël J, Delmas P, Hao J, Padilla F, Dandonneau M, Lavebratt C, Lesage F, Noël J, Delmas P (2013) Kv1.1 Channels Act as Mechanical Brake in the Senses of Touch and Pain. *Neuron* 77:899–914.
- Haq E, Contreras MA, Giri S, Singh I, Singh AK (2006) Dysfunction of peroxisomes in twitcher mice brain: A possible mechanism of psychosine-induced disease. *Biochem Biophys Res Commun* 343:229–238.
- Hein S, Schonfeld P, Kahlert S, Reiser G (2008) Toxic effects of X-linked adrenoleukodystrophy-associated, very long chain fatty acids on glial cells and neurons from rat hippocampus in culture. *Hum Mol Genet* 17:1750–1761.
- Hirsch NP (2007) Neuromuscular junction in health and disease. *Br J Anaesth* 99:132–138.
- Hiscoe HB (1947) Distribution of nodes and incisures in normal and regenerated nerve fibers. *Anat Rec* 99:447–475.
- Hivert B, Pinatel D, Labasque M, Tricaud N, Goutebroze L, Faivre-Sarrailh C (2016) Assembly of juxtaparanodes in myelinating DRG culture: Differential clustering of the Kv1/Caspr2 complex and scaffolding protein 4.1B. *Glia* 64:840–852.
- Ho JK, Moser H, Kishimoto Y, Hamilton JA (1995) Interactions of a very long chain fatty acid with model membranes and serum albumin. Implications for the pathogenesis of adrenoleukodystrophy. *J Clin Invest* 96:1455–1463.

- Hoepfner D, Schildknecht D, Braakman I, Philippsen P, Tabak HF (2005) Contribution of the Endoplasmic Reticulum to Peroxisome Formation. *Cell* 122:85–95.
- Holmgren J, Lönnroth I, Mansson JE, Svennerholm L (1975) Interaction of cholera toxin and membrane GM1 ganglioside of small intestine. *PNAS* 72:2520–2524.
- Hoshi T, Suzuki A, Hayashi S, Tohyama K, Hayashi A, Yamaguchi Y, Takeuchi K, Baba H (2007) Nodal protrusions, increased Schmidt-Lanterman incisures, and paranodal disorganization are characteristic features of sulfatide-deficient peripheral nerves. *Glia* 55:584–594.
- Howell OW, Palser A, Polito A, Melrose S, Zonta B, Scheiermann C, Vora AJ, Brophy PJ, Reynolds R (2006) Disruption of neurofascin localization reveals early changes preceding demyelination and remyelination in multiple sclerosis. *Brain* 129:3173–3185.
- Hu Y-B et al. (2015) The endosomal-lysosomal system: from acidification and cargo sorting to neurodegeneration. *Transl Neurodegener* 4:1–10.
- Huang J, Lam GY, Brumell JH (2011) Autophagy Signaling Through Reactive Oxygen Species. *Antioxid Redox Signal* 14:2215–2231.
- Hughes RAC, Cornblath DR (2005) Guillain-Barré syndrome. *Lancet* 366:1653–1666.
- Hulshagen L, Krysko O, Bottelbergs A, Huyghe S, Klein R, van Veldhoven PP, de Deyn PP, D'Hooge R, Hartmann D, Baes M (2008) Absence of Functional Peroxisomes from Mouse CNS Causes Dysmyelination and Axon Degeneration. *J Neurosci* 28:4015–4027.
- Huotari J, Helenius A (2011) Endosome maturation. *EMBO J* 30:3481–3500.
- Huxley AF, Stämpeli R (1949) Evidence for saltatory conduction in peripheral myelinated nerve fibres. *J Physiol* 108:315–339.
- Igarashi M, Schaumburg HH, Powers J, Kishimoto Y, Kolodny E, Suzuki K (1976a) Brain gangliosides in adrenoleukodystrophy. *J Neurochem* 27:327–328.
- Igarashi M, Schaumburg HH, Powers J, Kishimoto Y, Kolodny E, Suzuki K (1976b) Fatty acid abnormality in adrenoleukodystrophy. *J Neurochem* 26:851–860.
- Ishibashi T, Dupree JL, Ikenaka K, Hirahara Y, Honke K, Peles E, Popko B, Popko B, Suzuki K, Suzuki K, Nishino H, Nishino H, Baba H (2002) A Myelin Galactolipid, Sulfatide, Is Essential for Maintenance of Ion Channels on Myelinated Axon But Not Essential for Initial Cluster Formation. *J Neurosci* 22:6507–6514.
- Ivanovic A, Horresh I, Spiegel I, Golan N, Sabanay H, Frechter S, Ohno S, Terada N, Möbius W, Rosenbluth J, Brose N, Peles E (2012) The cytoskeletal adapter protein 4.1G organizes the internodes in peripheral myelinated nerves. *J Cell Biol* 196:337–344.
- Jenkins SM, Bennett V (2002) Developing nodes of Ranvier are defined by ankyrin-G clustering and are independent of paranodal axoglial adhesion. *Proc Natl Acad Sci U S A* 99:2303–2308.
- Jennings JJ, Zhu JH, Rbaibi Y, Luo X, Chu CT, Kiselyov K (2006) Mitochondrial Aberrations in Mucopolysaccharidosis Type IV. *J Biol Chem* 281:39041–39050.

- Jensen CS, Rasmussen HB, Misonou H (2011) Neuronal trafficking of voltage-gated potassium channels. *Mol Cell Neurosci* 48:288–297.
- Jessen KR, Mirsky R (1992) Schwann cells: early lineage, regulation of proliferation and control of myelin formation. *Curr Opin Neurobiol* 2:575–581.
- Jessen KR, Mirsky R (1999) Schwann cells and their precursors emerge as major regulators of nerve development. *Neurosci* 22:402–410.
- Jessen KR, Mirsky R (2005) The origin and development of glial cells in peripheral nerves. *Nat Rev Neurosci* 6:671–682.
- Jessen KR, Mirsky R (2016) The repair Schwann cell and its function in regenerating nerves. *J Physiol* 594:3521–3531.
- Jeyakumar M, Dwek RA, Butters TD, Platt FM (2005) Storage solutions: treating lysosomal disorders of the brain. *Nat Rev Neurosci* 6:713–725.
- Jeyakumar M, Thomas R, Elliot-Smith E, Smith DA, van der Spoel AC, d'Azzo A, Perry VH, Butters TD, Dwek RA, Platt FM (2003) Central nervous system inflammation is a hallmark of pathogenesis in mouse models of GM1 and GM2 gangliosidosis. *Brain* 126:974–987.
- Jobling MG, Yang Z, Kam WR, Lencer WI, Holmes RK (2012) A Single Native Ganglioside GM1-Binding Site Is Sufficient for Cholera Toxin To Bind to Cells and Complete the Intoxication Pathway. *mBio* 3:e00401–00412.
- Jung M, Sommer I, Schachner M, Nave K-A (1996) Monoclonal Antibody O10 Defines a Conformationally Sensitive Cell-Surface Epitope of Proteolipid Protein (PLP): Evidence that PLP Misfolding Underlies Dysmyelination in Mutant Mice. *J Neurosci* 16:7920–7929.
- Kaida K, Ariga T, Yu RK (2009) Antiganglioside antibodies and their pathophysiological effects on Guillain-Barre syndrome and related disorders. *Glycobiology* 19:676–692.
- Kamijo K, Taketani S, Yokota S, Osumi T, Hashimoto T (1990) The 70-kDa peroxisomal membrane protein is a member of the Mdr (P-glycoprotein)-related ATP-binding protein superfamily. *J Biol Chem* 265:4534–4540.
- Kasahara K, Watanabe K, Takeuchi K, Kaneko H, Oohira A, Yamamoto T, Sanai Y (2000) Involvement of Gangliosides in Glycosylphosphatidylinositol-anchored Neuronal Cell Adhesion Molecule TAG-1 Signaling in Lipid Rafts. *J Biol Chem* 275:34701–34709.
- Kassmann CM (2014) Myelin peroxisomes – Essential organelles for the maintenance of white matter in the nervous system. *Biochimie* 98:111–118.
- Kassmann CM, Lappe-Siefke C, Baes M, Brügger B, Mildner A, Werner HB, Natt O, Michaelis T, Prinz M, Frahm J, Nave K-A (2007) Axonal loss and neuroinflammation caused by peroxisome-deficient oligodendrocytes. *Nat Genet* 39:969–976.
- Kassmann CM, Quintes S, Rietdorf J, Möbius W, Sereda MW, Nientiedt T, Saher G, Baes M, Nave K-A (2011) A role for myelin-associated peroxisomes in maintaining paranodal loops and axonal integrity. *FEBS Lett* 585:2205–2211.

- Kemp S, Wanders R (2010) Biochemical Aspects of X-Linked Adrenoleukodystrophy. *Brain Pathol* 20:831–837.
- Jung CH, Ro SH, Cao J, Otto MN, Kim DH. (2010) mTOR regulation of autophagy. *FEBS Lett* 584:1287-1295.
- Kim PK, Mullen RT, Schumann U, Lippincott-Schwartz J (2006) The origin and maintenance of mammalian peroxisomes involves a de novo PEX16-dependent pathway from the ER. *J Cell Biol* 173:521–532.
- Kobayashi T, Shinnoh N, Kondo A, Yamada T (1997) Adrenoleukodystrophy Protein-Deficient Mice Represent Abnormality of Very Long Chain Fatty Acid Metabolism. *Biochem Biophys Res Commun* 232:6311–6636.
- Komada M, Soriano P (2002) β IV-spectrin regulates sodium channel clustering through ankyrin-G at axon initial segments and nodes of Ranvier. *J Cell Biol* 156:337–348.
- Korkotian E, Schwarz A, Pelled D, Schwarzmann G, Segal M, Futerman AH (1999) Elevation of Intracellular Glucosylceramide Levels Results in an Increase in Endoplasmic Reticulum Density and in Functional Calcium Stores in Cultured Neurons. *J Biol Chem* 274:21673–21678.
- Labasque M, Devaux JJ, Leveque C, Faivre-Sarrailh C (2011) Fibronectin Type III-like Domains of Neurofascin-186 Protein Mediate Gliomedin Binding and Its Clustering at the Developing Nodes of Ranvier. *J Biol Chem* 286:42426–42434.
- Labasque M, Faivre-Sarrailh C (2010) GPI-anchored proteins at the node of Ranvier. *FEBS Lett* 584:1787–1792.
- Lappe-Siefke C, Goebbels S, Gravel M, Nicksch E, Lee J, Braun PE, Griffiths IR, Nave K-A (2003) Disruption of *Cnp1* uncouples oligodendroglial functions in axonal support and myelination. *Nat Genet* 33:366–374.
- Launay N, Aguado C, Fourcade S, Ruiz M, Grau L, Riera J, Guilera C, Giròs M, Ferrer I, Knecht E, Pujol A (2015) Autophagy induction halts axonal degeneration in a mouse model of X-adrenoleukodystrophy. *Acta Neuropathol* 129:399–415.
- Levine B, Kroemer G (2008) Autophagy in the Pathogenesis of Disease. *Cell* 132:27–42.
- Loberto N, Prioni S, Prinetti A, Ottico E, Chigorno V, Karagogeos D, Sonnino S, Braverman NE, Braverman NE, Moser AB (2003) The adhesion protein TAG-1 has a ganglioside environment in the sphingolipid-enriched membrane domains of neuronal cells in culture. *J Neurochem* 85:224–233.
- Lombard-Platet G, Savary S, Sarde CO, Mandel JL, Chimini G (1996) A close relative of the adrenoleukodystrophy (ALD) gene codes for a peroxisomal protein with a specific expression pattern. *PNAS* 93:1265–1269.
- Lu J-F, Lawler AM, Watkins PA, Powers JM, Moser AB, Moser HW, Smith KD (1997) A mouse model for X-linked adrenoleukodystrophy. *PNAS* 94:9366–9371.
- Ma C, Agrawal G, Subramani S (2011) Peroxisome assembly: matrix and membrane protein biogenesis. *J Cell Biol* 193:7–16.

- Ma Q, Kobayashi M, Sugiura M, Ozaki N, Nishio K, Shiraishi Y, Furukawa K, Furukawa K, Sugiura Y (2003) Morphological study of disordered myelination and the degeneration of nerve fibers in the spinal cord of mice lacking complex gangliosides. *Arch Histol Cytol* 66:37–44.
- Maccioni HJF (2007) Glycosylation of glycolipids in the Golgi complex. *J Neurochem* 103:81–90.
- Mandard S, Miller M, Kersten S (2004) Peroxisome proliferator-activated receptor a target genes. *Cell Mol Life Sci* 61:393–416.
- Marshansky V, Futai M (2008) The V-type H⁺-ATPase in vesicular trafficking: targeting, regulation and function. *Curr Opin Cell Biol* 20:415–426.
- Matsuzaki T, Fujiki Y (2008) The peroxisomal membrane protein import receptor Pex3p is directly transported to peroxisomes by a novel Pex19p- and Pex16p-dependent pathway. *J Cell Biol* 183:1275–1286.
- Maxfield FR, Yamashiro DJ (1987) Endosome Acidification and the Pathways of Receptor-Mediated Endocytosis. *Adv Exp Med Biol* 225:189–198.
- McKerracher L, David S, Jackson DL, Kottis V, Dunn RJ, Braun PE (1994) Identification of myelin-associated glycoprotein as a major myelin-derived inhibitor of neurite growth. *Neuron* 13:805–811.
- McNew JA, Goodman JM (1994) An oligomeric protein is imported into peroxisomes in vivo. *J Cell Biol* 127:1245–1257.
- Mehta NR, Nguyen T, Bullen JW, Griffin JW, Schnaar RL (2010) Myelin-Associated Glycoprotein (MAG) Protects Neurons from Acute Toxicity Using a Ganglioside-Dependent Mechanism. *ACS Chem Neurosci* 1:215–222.
- Meinecke M, Cizmowski C, Schliebs W, Krüger V, Beck S, Wagner R, Erdmann R (2010) The peroxisomal importomer constitutes a large and highly dynamic pore. *Nat Cell Biol* 12:273–277.
- Meresse S, Gorvel JP, Chavrier P (1995) The rab7 GTPase resides on a vesicular compartment connected to lysosomes. *J Cell Sci* 108:3349–3358.
- Michailov GV, Sereda MW, Brinkmann BG, Fischer TM, Haug B, Birchmeier C, Role L, Lai C, Schwab MH, Nave KA (2004) Axonal Neuregulin-1 Regulates Myelin Sheath Thickness. *Science* 304:700–703.
- Mizushima N, Yamamoto A, Matsui M, Yoshimori T, Ohsumi Y (2003) In Vivo Analysis of Autophagy in Response to Nutrient Starvation Using Transgenic Mice Expressing a Fluorescent Autophagosome Marker. *Mol Biol Cell* 15:1101–1111.
- Moser HW, Mahmood A, Raymond GV (2007) X-linked adrenoleukodystrophy. *Nat Clin Pract Neurol* 3:140–151.
- Mosser J, Douar A-M, Sarde C-O, Kioschis P, Feil R, Moser H, Poustka A-M, Mandel J-L, Aubourg P (1993) Putative X-linked adrenoleukodystrophy gene shares unexpected homology with ABC transporters. *Nature* 361:726–730.

- Mousavi SA, Malerød L, Berg T, Kjekken R (2004) Clathrin-dependent endocytosis. *Biochem J* 377:1–16.
- Mullock BM, Bright NA, Fearon CW, Gray SR, Luzio J (1998) Fusion of Lysosomes with Late Endosomes Produces a Hybrid Organelle of Intermediate Density and Is NSF Dependent. *J Cell Biol* 140:591–601.
- Tasaki I (1939) The electro-saltatory transmission of the nerve impulse and the effect of narcosis upon the nerve fiber. *Am J Physiol* 127:211–227.
- Naguib M, Flood P, McArdle JJ, Brenner HR (2002) Advances in Neurobiology of the Neuromuscular Junction: Implications for the Anesthesiologist. *Anesthesiology* 96:202–231.
- Nave K-A (2010a) Myelination and support of axonal integrity by glia. *Nature* 468:244–252.
- Nave K-A (2010b) Myelination and the trophic support of long axons. *Nat Rev Neurosci* 11:275–283.
- Nave K-A, Sereda MW, Ehrenreich H (2007) Mechanisms of Disease: inherited demyelinating neuropathies—from basic to clinical research. *Nat Clin Pract Neurol* 3:453–464.
- Neefjes J, van der Kant R (2014) Stuck in traffic: an emerging theme in diseases of the nervous system. *Cell* 37:66–76.
- Netik A, Forss-Petter S, Holzinger A, Molzer B, Unterrainer G, Berger J (1999) Adrenoleukodystrophy-related protein can compensate functionally for adrenoleukodystrophy protein deficiency (X-ALD): implications for therapy. *Hum Mol Genet* 8:907–913.
- Noda T, Ohsumi Y (1998) Tor, a Phosphatidylinositol Kinase Homologue, Controls Autophagy in Yeast. *J Biol Chem* 273:3963–3966.
- Nuttall JM, Motley A, Hetteema EH (2011) Peroxisome biogenesis: recent advances. *Curr Opin Cell Biol* 23:421–426.
- Oswald RE, Freeman JA (1981) Alpha-bungarotoxin binding and central nervous system nicotinic acetylcholine receptors. *Neuroscience* 6:1–14.
- Pan B, Fromholt SE, Hess EJ, Crawford TO, Griffin JW, Sheikh KA, Schnaar RL (2005) Myelin-associated glycoprotein and complementary axonal ligands, gangliosides, mediate axon stability in the CNS and PNS: neuropathology and behavioral deficits in single- and double-null mice. *Exp Neurol* 195:208–217.
- Patzig J, Jahn O, Tenzer S, Wichert SP, de Monasterio-Schrader P, Rosfa S, Kuharev J, Yan K, Bormuth I, Bremer J, Aguzzi A, Orfaniotou F, Hesse D, Schwab MH, Mobius W, Nave KA, Werner HB (2011) Quantitative and Integrative Proteome Analysis of Peripheral Nerve Myelin Identifies Novel Myelin Proteins and Candidate Neuropathy Loci. *J Neurosci* 31:16369–16386.
- Peles E, Salzer JL (2000) Molecular domains of myelinated axons. *Curr Opin Neurobiol* 10:558–565.

- Pereira JA, Lebrun-Julien F, Suter U (2012) Molecular mechanisms regulating myelination in the peripheral nervous system. *Trends Neurosci* 35:123–134.
- Périchon R, Moser AB, Wallace WC, Cunningham SC, Roth GS, Moser HW (1998) Peroxisomal Disease Cell Lines with Cellular Plasmalogen Deficiency Have Impaired Muscarinic Cholinergic Signal Transduction Activity and Amyloid Precursor Protein Secretion. *Biochem Biophys Res Commun* 248:57–61.
- Peters A (2002) The effects of normal aging on myelin and nerve fibers: A review. *J Neurocyt* 8/9:581–593.
- Pham-Dinh D, Birling M-C, Roussel G, Dautigny A, Nussbaum J-L (1991) Proteolipid DM-20 predominates over PLP in peripheral nervous system. *Neuroreport* 2:89–92.
- Platt FM, Boland B, van der Spoel AC, Bol B (2012) The cell biology of disease: Lysosomal storage disorders: The cellular impact of lysosomal dysfunction. *J Cell Biol* 199:723–734.
- Platta HW, Erdmann R (2007) Peroxisomal dynamics. *Trends Cell Biol* 17:474–484.
- Platta HW, Magraoui El F, Schlee D, Grunau S, Girzalsky W, Erdmann R (2007) Ubiquitination of the peroxisomal import receptor Pex5p is required for its recycling. *J Cell Biol* 177:197–204.
- Poliak S, Gollan L, Martinez R, Custer A, Einheber S, Salzer JL, Trimmer JS, Schragar P, Peles E (1999) Caspr2, a New Member of the Neurexin Superfamily, Is Localized at the Juxtaparanodes of Myelinated Axons and Associates with K⁺ Channels. *Neuron* 24:1037–1047.
- Poliak S, Peles E (2003) The local differentiation of myelinated axons at nodes of Ranvier. *Nat Rev Neurosci* 4:968–980.
- Poulos A, Sheffield L, Sharp P, Sherwood G, Johnson D, Beckman K, Fellenberg AJ, Wraith JE, Chow CW, Usher S, Singh H (1988) Rhizomelic chondrodysplasia punctata: Clinical, pathologic, and biochemical findings in two patients. *J Pediatr* 113:685–690.
- Prioni S, Mauri L, Loberto N, Casellato R, Chigorno V, Karagogeos D, Prinetti A, Sonnino S (2004) Interactions between gangliosides and proteins in the exoplasmic leaflet of neuronal plasma membranes: A study performed with a tritium-labeled GM1 derivative containing a photoactivable group linked to the oligosaccharide chain. *Glycoconj J* 21:461–470.
- Pujol A, Ferrer I, Camps C, Metzger E, Hindelang C, Callizot N, Ruiz M, Pampols T, Giros M, Mandel JL (2004) Functional overlap between ABCD1 (ALD) and ABCD2 (ALDR) transporters: a therapeutic target for X-adrenoleukodystrophy. *Hum Mol Genet* 13:2997–3006.
- Pujol A, Hindelang C, Callizot N, Bartsch U, Schachner M, Mandel JL (2002) Late onset neurological phenotype of the X-ALD gene inactivation in mice: a mouse model for adrenomyeloneuropathy. *Hum Mol Genet* 11:499–505.
- Quarles RH (2002) Myelin sheaths: glycoproteins involved in their formation, maintenance and degeneration. *Cell Mol Life Sci* 59:1851–1871.

- Rasband MN, Shrager P (2000) Ion channel sequestration in central nervous system axons. *J Physiol* 525:63–73.
- Rasband MN, Trimmer JS, Schwarz TL, Levinson SR, Ellisman MH, Schachner M, Shrager P (1998) Potassium Channel Distribution, Clustering, and Function in Remyelinating Rat Axons. *J Neurosci* 18:36–47.
- Reddy JK, Mannaerts GP (1994) Peroxisomal Lipid Metabolism. *Ann Rev Nutr* 14:343–370.
- Reuber BE, Germain-Lee E, Collins CS, Morrell JC, Ameritunga R, Moser HW, Valle D, Gould SJ, Wraith JE (1997) Mutations in PEX1 are the most common cause of peroxisome biogenesis disorders. *Nat Genet* 17:445–448.
- Rink J, Ghigo E, Kalaidzidis Y, Zerial M (2005) Rab Conversion as a Mechanism of Progression from Early to Late Endosomes. *Cell* 122:735–749.
- Rios JC, Rubin M, Martin MS, Downey RT, Einheber S, Rosenbluth J, Levinson SR, Bhat M, Salzer JL (2003) Paranodal Interactions Regulate Expression of Sodium Channel Subtypes and Provide a Diffusion Barrier for the Node of Ranvier. *J Neurosci* 23:7001–7011.
- Rosenbluth J (2009) Multiple functions of the paranodal junction of myelinated nerve fibers. *J Neurosci Res* 87:3250–3258.
- Rubinsztein DC (2006) The roles of intracellular protein-degradation pathways in neurodegeneration. *Nature* 443:780–786.
- Saito M, Saito M (1991) Incorporation of Very-Long-Chain Fatty Acids into Sphingolipids of Cultured Neural Cells. *J Neurochem* 57:465.
- Salzer JL, Brophy PJ, Peles E (2008) Molecular domains of myelinated axons in the peripheral nervous system. *Glia* 56:1532–1540.
- Salzer JL, Bunge RP (1980) Studies of Schwann cell proliferation. I. An analysis in tissue culture of proliferation during development, Wallerian degeneration, and direct injury. *J Cell Biol* 84:739–752.
- Sandhoff K, Harzer K (2013) Gangliosides and Gangliosidoses: Principles of Molecular and Metabolic Pathogenesis. *J Neurosci* 33:10195–10208.
- Savvaki M, Theodorakis K, Zoupi L, Stamatakis A, Tivodar S, Kyriacou K, Stylianopoulou F, Karagogeos D (2010) The Expression of TAG-1 in Glial Cells Is Sufficient for the Formation of the Juxtaparanodal Complex and the Phenotypic Rescue of Tag-1 Homozygous Mutants in the CNS. *J Neurosci* 30:13943–13954.
- Schedin S, Sindelar PJ, Pentchev P, Brunk U, Dallner G (1997) Peroxisomal Impairment in Niemann-Pick Type C Disease. *J Biol Chem* 272:6245–6251.
- Scherer SS (1997) The biology and pathobiology of Schwann cells. *Curr Opin Neurol* 10:386–397.
- Schindelin J, Arganda-Carreras I, Frise E, Kaynig V, Longair M, Pietzsch T, Preibisch S, Rueden C, Saalfeld S, Schmid B, Tinevez J-Y, White DJ, Hartenstein V, Eliceiri K,

- Tomancak P, Cardona A (2012) Fiji: an open-source platform for biological-image analysis. *Nat Meth* 9:676–682.
- Schnaar RL, Gerardy-Schahn R, Hildebrandt H (2014) Sialic Acids in the Brain: Gangliosides and Polysialic Acid in Nervous System Development, Stability, Disease, and Regeneration. *Physiol Rev* 94:461–518.
- Schrader M, Bonekamp NA, Islinger M, (2012) Fission and proliferation of peroxisomes. *Biochim Biophys Acta* 1822:1343–1357.
- Schrader M, Fahimi HD (2004) Mammalian peroxisomes and reactive oxygen species. *Histochem Cell Biol* 122:383–393.
- Schultz RL, Karlsson U (1965) Fixation of the central nervous system for electron microscopy by aldehyde perfusion: II. Effect of osmolarity, pH of perfusate, and fixative concentration. *J Ultrastruct Res* 12:187–206.
- Seitelberger F (1995) Neuropathology and Genetics of Pelizaeus-Merzbacher Disease. *Brain Pathol* 5:267–273.
- Settembre C, Ballabio A, Settembre C, Ballabio A, Settembre C, Ballabio A (2014) Lysosome: regulator of lipid degradation pathways. *Trends Cell Biol* 24:743–750.
- Settembre C, Fraldi A, Jahreiss L, Spampinato C, Venturi C, Medina D, de Pablo R, Tacchetti C, Rubinsztein DC, Ballabio A (2008) A block of autophagy in lysosomal storage disorders. *Hum Mol Genet* 17:119–129.
- Sheikh FG, Pahan K, Khan M, Barbosa E, Singh I (1998) Abnormality in catalase import into peroxisomes leads to severe neurological disorder. *PNAS* 95:2961–2966.
- Sheikh KA, Sun J, Liu Y, Kawai H, Crawford TO, Proia RL, Griffin JW, Schnaar RL (1999) Mice lacking complex gangliosides develop Wallerian degeneration and myelination defects. *PNAS* 96:7532–7537.
- Sherratt RM, Bostock H, Sears TA (1980) Effects of 4-aminopyridine on normal and demyelinated mammalian nerv fibres. *Nature* 283:570–572.
- Simons M, Krämer E-M, Macchi P, Rathke-Hartlieb S, Trotter J, Nave K-A, Schulz JB (2002) Overexpression of the myelin proteolipid protein leads to accumulation of cholesterol and proteolipid protein in endosomes/lysosomes. *J Cell Biol* 157:327–336.
- Singer M, Bryant SV (1969) Movements in the Myelin Schwann Sheath of the Vertebrate Axon. *Nature* 221:1148–1150.
- Singh AK, Dhaunsi GS, Gupta MP, Orak JK, Asayama K, Singh I (1994) Demonstration of Glutathione Peroxidase in Rat Liver Peroxisomes and Its Intraorganellar Distribution. *Arch Biochem Biophys* 315:331–338.
- Singh I, Pujol A (2010) Pathomechanisms Underlying X-Adrenoleukodystrophy: A Three-Hit Hypothesis. *Brain Pathol* 20:838–844.
- Singh R, Kaushik S, Wang Y, Xiang Y, Novak I, Komatsu M, Tanaka K, Cuervo AM, Czaja MJ (2009) Autophagy regulates lipid metabolism. *Nature* 458:1131–1135.

- Sinha K, Karimi-Abdolrezaee S, Velumian AA, Fehlings MG (2005) Functional Changes in Genetically Dysmyelinated Spinal Cord Axons of Shiverer Mice: Role of Juxtaparanodal Kv1 Family K⁺ Channels. *J Neurophys* 95:1683–1695.
- Small JR, Ghabriel MN, Allt G (1980) The development of Schmidt-Lanterman incisures: an electron microscope study. *Journal of Anatomy* 150:277–286.
- Smart SL, Lopantsev V, Zhang CL, Robbins CA, Wang H, Chiu SY, Schwartzkroin PA, Messing A, Tempel BL (1998) Deletion of the Kv1.1 Potassium Channel Causes Epilepsy in Mice. *Neuron* 20:809–819.
- Sonnino S, Mauri L, Chigorno V, Prinetti A (2006) Gangliosides as components of lipid membrane domains. *Glycobiology* 17:1–13.
- Spiegel I, Peles E (2002) Cellular junctions of myelinated nerves (Review). *Mol Membr Biol* 19:95–101.
- Stanley WA, Filipp FV, Kursula P, Schüller N, Erdmann R, Schliebs W, Sattler M, Wilmanns M (2006) Recognition of a Functional Peroxisome Type 1 Target by the Dynamic Import Receptor Pex5p. *Mol Cell* 24:653–663.
- Steinberg SJ, Dodt G, Raymond GV, Braverman NE, Moser AB, Moser HW (2006) Peroxisome biogenesis disorders. *Biochim Biophys Acta* 1763:1733–1748.
- Susuki K, Rasb MN, Rasband MN, Tohyama K, Koibuchi K, Okamoto S, Funakoshi K, Hirata K, Baba H, Yuki N (2007) Anti-GM1 Antibodies Cause Complement-Mediated Disruption of Sodium Channel Clusters in Peripheral Motor Nerve Fibers. *J Neurosci* 27:3956–3967.
- Swinkels BW, Gould SJ, Bodnar AG, Rachubinski RA, Subramani S (1991) A novel, cleavable peroxisomal targeting signal at the amino-terminus of the rat 3-ketoacyl-coA thiolase. *EMBO J* 10:3255–3262.
- Tatsumi K, Saito M, Lin B, Iwamori M, Ichiseki H, Shimozawa N, Kamoshita S, Igarashi T, Sakakihara Y (2001) Enhanced expression of a-series gangliosides in fibroblasts of patients with peroxisome biogenesis disorders. *Biochim Biophys Acta* 1513:285–293.
- Teigler A, Komljenovic D, Draguhn A, Gorgas K, Just WW (2009) Defects in myelination, paranode organization and Purkinje cell innervation in the ether lipid-deficient mouse cerebellum. *Hum Mol Genet* 18:1897–1908.
- Tessitore A, del P. Martin M, Sano R, Ma Y, Mann L, Ingrassia A, Laywell ED, Steindler DA, Hendershot LM, d'Azzo A (2004) GM1-Ganglioside-Mediated Activation of the Unfolded Protein Response Causes Neuronal Death in a Neurodegenerative Gangliosidosis. *Mol Cell* 15:753–766.
- Tettamanti G, Bonali F, Marchesini S, Zambotti V (1973) A new procedure for the extraction, purification and fractionation of brain gangliosides. *Biochim Biophys Acta* 296:160–170.
- Thai T-P, Rodemer C, Jauch A, Hunziker A, Moser A, Gorgas K, Just WW (2001) Impaired membrane traffic in defective ether lipid biosynthesis. *Hum Mol Genet* 10:127–136.

- Tjelle TE, Brech A, Juvet LK, Griffiths G, Berg T, Wright JE (1996) Isolation and characterization of early endosomes, late endosomes and terminal lysosomes: their role in protein degradation. *J Cell Sci* 109:2905–2914.
- Tokuyasu KT (1973) A technique for ultracryotomy of cell suspensions and tissues. *The Journal of Cell Biology* 57:551–565.
- Traka M, Dupree JL, Popko B, Karagogeos D (2002) The Neuronal Adhesion Protein TAG-1 Is Expressed by Schwann Cells and Oligodendrocytes and Is Localized to the Juxtaparanodal Region of Myelinated Fibers. *J Neurosci* 22:3016–3024.
- Traka M, Goutebroze L, Denisenko N, Bessa M, Nifli A, Havaki S, Iwakura Y, Fukamauchi F, Watanabe K, Soliven B, Girault J-A, Karagogeos D (2003) Association of TAG-1 with Caspr2 is essential for the molecular organization of juxtaparanodal regions of myelinated fibers. *J Cell Biol* 162:1161–1172.
- Trapp BD (1990) Myelin-Associated Glycoprotein Location and Potential Functions. *Ann N Y Acad Sci* 605:29–43.
- Trapp BD, Andrews SB, Wong A, O'Connell M, Griffin JW (1989) Co-localization of the myelin-associated glycoprotein and the microfilament components, F-actin and spectrin, in Schwann cells of myelinated nerve fibres. *J Neurocyt* 18:47–60.
- Uyemura K, Tobar C, Hirano S, Tsukada Y (1972) Comparative studies on the myelin proteins of bovine peripheral nerve and spinal cord. *Acta Neuropathol* 19:2607–2614.
- Vabnick I, Trimmer JS, Schwarz TL, Levinson SR, Risal D, Shrager P (1999) Dynamic Potassium Channel Distributions during Axonal Development Prevent Aberrant Firing Patterns. *J Neurosci* 19:747–758.
- van der Zand A, Braakman I, Tabak HF (2010) Peroxisomal Membrane Proteins Insert into the Endoplasmic Reticulum. *Mol Biol Cell* 21:2057–2065.
- van Doorn PA, Ruts L, Jacobs BC (2008) Clinical features, pathogenesis, and treatment of Guillain-Barré syndrome. *The Lancet Neurology* 7:939–950.
- van Roermund CWT, Visser WF, IJlst L, van Cruchten A, Boek M, Kulik W, Waterham HR, Wanders RJA (2008) The human peroxisomal ABC half transporter ALDP functions as a homodimer and accepts acyl-CoA esters. *FASEB J* 22:4201–4208.
- Vellodi A (2005) Lysosomal storage disorders. *Br J Haematology* 128:413–431.
- Verity C, Winstone AM, Stellitano L, Will R, Nicoll A (2009) The epidemiology of progressive intellectual and neurological deterioration in childhood. *Arch Dis Child* 95:361–364.
- Viader A, Sasaki Y, Kim S, Strickland A, Workman CS, Yang K, Gross RW, Milbrandt J (2013) Aberrant Schwann Cell Lipid Metabolism Linked to Mitochondrial Deficits Leads to Axon Degeneration and Neuropathy. *Neuron* 77:886–898.
- Vitner EB, Platt FM, Futerman AH (2010) Common and uncommon pathogenic cascades in lysosomal storage diseases. *J Biol Chem* 285:20423–20427.
- Walkley SU (2004) Secondary accumulation of gangliosides in lysosomal storage disorders. *Seminars in Cell & Developmental Biology* 15:433–444.

- Wanders RJA (2004a) Metabolic and molecular basis of peroxisomal disorders: A review. *Am J Med Genet* 126A:355–375.
- Wanders RJA (2004b) Peroxisomes, lipid metabolism, and peroxisomal disorders. *Mol Genet Metab* 83:16–27.
- Wanders RJA, Waterham HR (2006a) Peroxisomal disorders: The single peroxisomal enzyme deficiencies. *Biochim Biophys Acta* 1763:1707–1720.
- Wang H, Tempel BL (1993) Heteromultimeric K⁺ channels in terminal and juxtaparanodal regions of neurons. *Nature* 365:75–79.
- Waxman SG (1980) Determinants of conduction velocity in myelinated nerve fibers. *Muscle Nerve* 3:141–150.
- Waxman SG, Ritchie JM (1985) Organization of ion channels in the myelinated nerve fiber. *Science* 228:1502–1507.
- Wiesinger C, Kunze M, Regelsberger G, Forss-Petter S, Berger J (2013) Impaired Very Long-chain Acyl-CoA -Oxidation in Human X-linked Adrenoleukodystrophy Fibroblasts Is a Direct Consequence of ABCD1 Transporter Dysfunction. *J Biol Chem* 288:19269–19279.
- Wiggins RC, Benjamins JA, Morell P (1975) Appearance of myelin proteins in rat sciatic nerve during development. *Brain Res* 89:99–106.
- Wilkins A, Majed H, Layfield R, Compston A, Chandran S (2003) Oligodendrocytes Promote Neuronal Survival and Axonal Length by Distinct Intracellular Mechanisms: A Novel Role for Oligodendrocyte-Derived Glial Cell Line-Derived Neurotrophic Factor. *J Neurosci* 23:4967–4974.
- Wraith JE (2002) Lysosomal disorders. *Semin Neonatol* 7:75–83.
- Xie F, Liang P, Fu H, Zhang J-C, Chen J (2014) Effects of normal aging on myelin sheath ultrastructures in the somatic sensorimotor system of rats. *Mol Med Rep* 10:459–466.
- Yang LJ, Zeller CB, Shaper NL, Kiso M, Hasegawa A, Shapiro RE, Schnaar RL (1996) Gangliosides are neuronal ligands for myelin-associated glycoprotein. *PNAS* 93:814–818.
- Yang Y, Lacas-Gervais S, Morest DK, Solimena M, Rasband MN (2004) IV Spectrins Are Essential for Membrane Stability and the Molecular Organization of Nodes of Ranvier. *J Neurosci* 24:7230–7240.
- Yin X, Crawford TO, Griffin JW, Tu P-H, Li C, Roder J, Trapp BD (1998) Myelin-Associated Glycoprotein is a Myelin Signal that Modulates the Caliber of Myelinated Axons. *J Neurosci* 18:1953–1962.
- Yu RK, Tsai Y-T, Ariga T, Yanagisawa M (2011) Structures, Biosynthesis, and Functions of Gangliosides-an Overview. *J Oleo Sci* 60:537–544.
- Zenker J, Poirot O, de Preux Charles AS, Arnaud E, Medard JJ, Lacroix C, Kuntzer T, Chrast R (2012) Altered Distribution of Juxtaparanodal Kv1.2 Subunits Mediates

Peripheral Nerve Hyperexcitability in Type 2 Diabetes Mellitus. *J Neurosci* 32:7493–7498.

Zhang Y, Bekku Y, Dzhashiashvili Y, Armenti S, Meng X, Sasaki Y, Salzer J, Milbrandt J (2012) Assembly and Maintenance of Nodes of Ranvier Rely on Distinct Sources of Proteins and Targeting Mechanisms. *Neuron* 73:92–107.

Curriculum vitae

Personal details

Surname: Kleinecke
First name: Sandra

Date of birth: 09.02.1988, Blankenburg (Harz)
Nationality: German

Home address: Kasseler Landstraße 87
37081 Göttingen

Work address: MPI of Experimental Medicine
Department of Neurogenetics
Hermann-Rein Str. 3, 37075 Göttingen, Germany
Tel. +49 551 3899-744

E-mail: Kleinecke@em.mpg.de

Education

01/2013 - present Graduate student at the Max Planck Institute of Experimental Medicine, Department of Neurogenetics

Thesis: *“Cellular and subcellular analysis of peripheral neuropathy caused by peroxisomal dysfunction in mice”*
Student of the Molecular Medicine program (University Medical Center, Göttingen)

10/2012 Master of Science (grade: 1.2)

10/2010 - 10/2012 Master student of the “Developmental, Neural and Behavioral Biology” program, Georg-August University, Göttingen

Master thesis: *„Analysis of the peripheral pathology in mouse models of peroxisomal disorders“*, Max Planck Institute of Experimental Medicine, Department of Neurogenetics

09/2010 Bachelor of Science (grade: 1.6)

- 10/2007 - 09/2010 Bachelor student of the Biology program, Georg-August University, Göttingen
- Bachelor thesis: “*Charakterisierung cis-regulatorischer Elemente für funktionelle Motoneuron-Subtypen*“, European Neuroscience Institute
- 2007 Allgemeine Hochschulreife (Abitur), Europagymnasium Richard von Weizsäcker, Thale, Germany (grade: 1.6)

Workshops

- 06/2015 “Academic writing”, University Medical Center, Göttingen
- 06/2012 “Schizophrenia“, Max Planck Institute of Experimental Medicine, Göttingen
- 11/2011 “Multiple Sclerosis“, Max Planck Institute of Experimental Medicine, Göttingen

Meetings and conferences

- 01/2016 Women’s Careers and Networks, Georg-August University, Göttingen
- 12/2014 PerFuMe (Peroxisome Formation, Function, Metabolism), Groningen, The Netherlands

Publications

Richert S, **Kleinecke S**, Günther J, Schaumburg F, Edgar J, Nienhaus GU, Nave KA, Kassmann CM. In vivo labeling of peroxisomes by photoconvertible mEos2 in myelinating glia of mice. *Biochimie*. 2014 Mar; 98:127-34

S. Kleinecke, S. Richert, L. de Hoz, B. Brügger, S. Quintes, J. Blanz, R. McGonigal, K. Naseri, T. Sachsenheimer, C. Lüchtenborg, E. Asadollahi, W. Möbius, H. Willison, M. Baes, K.-A. Nave, and C. M. Kassmann. Peripheral neuropathy caused by impaired peroxisomal-lysosomal lipid metabolism. In preparation